THE CATHOLIC UNIVERSITY OF AMERICA

Strangeness Photoproduction in the $\gamma p \rightarrow K^0\Sigma^+$ Reaction

A DISSERTATION

Submitted to the Faculty of the

Department of Physics

School of Arts and Sciences

Of The Catholic University of America

In Partial Fulfillment of the Requirements

For the Degree

Doctor of Philosophy

by

Bryan Carnahan

Washington, District of Columbia

2003

Strangeness Photoproduction in the $\gamma p \to K^0\Sigma^+$ Reaction

Bryan Carnahan, Ph.D.

Director: Franz Klein, Ph.D.

ABSTRACT

The photoproduction reaction $\gamma p \to K^0\Sigma^+$ was analyzed in the photon energy range from 1.15 to 2.35 GeV. This thesis contains the first high-statistics analysis of K^0 photoproduction. Data were taken in Hall B at Jefferson Lab using tagged photons incident on a liquid hydrogen target, with all outgoing charged particles in the final states $(\pi^+\pi^-)(p\pi^0)$ and $(\pi^+\pi^-)(n\pi^+)$ detected by the CLAS spectrometer. As the reaction $\gamma p \to K^0\Sigma^+$ is a rare process, most of the detected events are due to unwanted background reactions. Careful data fits and cross checks are required to identify the reaction being studied. To determine the acceptance for the desired reaction and the possible contamination by background processes, a detailed Monte Carlo simulation of all of these processes is performed. Data sets at beam energies of 2.445 and 3.115 GeV were studied separately and then averaged into a single data set, with much better statistical precision than previous measurements. Our cross sections are smaller than previous experimental data and theoretical predictions based on those data, especially in the forward angular region, but are similar in shape in the total cross section.

This dissertation by Bryan Carnahan fulfills the dissertation requirement for the doctoral degree in Doctor of Philosophy in Physics approved by Franz Klein, Ph.D., as Director and Hall Crannell, Ph.D., and Daniel Sober, Ph.D., as Readers.

Franz Klein, Ph.D., Director

Hall Crannell, Ph.D., Reader

Daniel Sober, Ph.D., Reader

Acknowledgments

Many thanks to my supervisors at The Catholic University of America, including Drs. Hall Crannell, Daniel Sober, Franz Klein, Konstantin Lukashin, Alberto Longhi, and Scott Matthews. Many people at Jefferson Lab helped me in my analysis, including Will Brooks, Dennis Weygand, Mac Mestayer, Reinhard Schumacher, John McNabb, David Lawrence, and Bernhard Mecking. Thanks also to my parents, William and Taimi Carnahan, and Danielle for all their help. This work was supported by the National Science Foundation, Grant PHY-0098674 and its predecessors.

Contents

List of Figures

List of Tables

Introduction

This thesis presents results of an experiment investigating the reaction $\gamma p \rightarrow \mathrm{K}^0\Sigma^+$ using a tagged photon beam and a large-acceptance detector. The analysis results in values for total and differential cross sections for this reaction.

The first chapter presents the motivation for studying this reaction and describes existing experimental data and theoretical models. The second chapter explains the physical setup of the detector system used to obtain the experimental data. The third chapter describes how the experimental data were processed into a format which was suitable for physics analysis and how photon flux values were obtained. The fourth chapter presents the analysis method for determining the final event sample from the experimental data, studies of acceptance and background processes, and a study of the statistical and systematic uncertainties. The fifth chapter presents the final results for the differential, integrated and total cross sections for this reaction and comparisons to previous experimental data and theoretical models.

Chapter 1

Physics Motivation and Existing Data

1.1 Physics motivation

While the associated production of strange particles has been studied for over four decades, the underlying reaction mechanism is still not well understood. It was discovered in early experiments that whenever the baryons Σ or Λ were produced, a K meson (kaon) also appeared. This led to the idea of a quantum number called strangeness which was later associated with the presence of the *strange* (s) quark. Strangeness production can result in the excitation of hyperon resonances and some nucleon resonances that are not excited in pion production.

1.1.1 Baryon physics

From results of deep inelastic electron scattering experiments, it was confirmed that nucleons are comprised of quarks, which are charged, point-like particles. The quantum numbers of quarks can be used to explain nucleon properties such as charge and isospin. While the magnetic moments seemed initially to be explained by existing quark models, subsequent experiments at CERN [1] and SLAC [2] have shown that gluons have a large contribution. A gluon is an exchange particle which mediates the strong interaction. The proton (p) is made up of two *up* (u) quarks and one *down* (d) valence quark while the neutron (n) is made up of one u-quark and two d-quarks. Baryons are three-quark states with half-integral spin and are thus fermions. The nucleons, p and n, are considered as the ground states of the baryon spectrum. The other class of multiquark states are mesons which have integral spin, and are thus bosons. In the following discussion only u-, d- and s-quarks are considered. The "heavy" quarks c,b and t (charm, bottom, and top), do not play a significant role at the energies of this experiment. While nucleons are comprised of three "valence quarks" (u- and d-quarks) that determine their quantum numbers, there also exist in the nucleon "sea quarks", quark-antiquark pairs which can become separated in interactions of the nucleon with other particles.

Kaons are mesons containing one s-quark or antiquark ($\bar{s}$-quark). These are produced via strong or electromagnetic interactions during which the strangeness is conserved. For example, the sum of strangeness quantum numbers from the number of s-quarks (S = -1) and antistrange ($\bar{s}$) quarks (S =+1) has to be the same in the initial and final state. Strange particles decay via the strong, electromagnetic or weak interaction. In the latter case the strangeness quantum number is not conserved. The strangeness component of the resultant particles comes from a concurrent production of a particle containing an s-quark and one containing an $\bar{s}$-quark.

Examples of baryons comprised of only u- and d-quarks are the nucleons, proton and neutron, and the Δ particles. Hyperons are baryons containing one or more s-quarks and include the Λ, Σ, Ξ, and Ω particles [3].

1.1.1.1 The baryon octet

Consider the baryon ground states with spin and parity $J^p = \frac{1}{2}^+$ (where the quark orbital angular momentum is l =0). Since the three valence quarks in the baryon each have a spin of $\frac{1}{2}$, one of the three quarks must have a spin projection opposite to the other two. This spin state is thus not symmetric or anti-symmetric under a spin exchange, but instead has a mixed symmetry. Wave functions for the proton and neutron are written as permutations involving $|p>=|uud>$ and $|n>=|udd>$. These nucleons form an isospin doublet. Baryons which contain two s-quarks comprise an isospin doublet involving two s-quarks and either a u- or d-quark as $|\Xi^+>=|uss>$ and $|\Xi^->=|dss>$. There also exist baryons with spin and parity $J^p = \frac{1}{2}^+$ and one s-quark which form an isospin triplet, $|\Sigma^+>=|uus>$, $|\Sigma^0>=|uds>$ and $|\Sigma^->=|dds>$, and an isospin singlet state $|\Lambda>=|uds>$.

1.1.2 Photoproduction of K^0

The reaction $\gamma p \rightarrow \mathrm{K}^0\Sigma^+$ can be rewritten by using the valence quarks of each particle: $|\gamma> + |uud> \rightarrow |d\bar{s}> + |uus>$. Strangeness is conserved in this electromagnetic reaction as the proton has a strangeness of zero, the K^0 has a strangeness of +1 due to its $\bar{s}$-quark, and the Σ^+ has a strangeness of -1 due to its s-quark. The production of two strange particles may result from various mechanisms:

- the decoupling of an $s\bar{s}$ pair out of the "sea quarks" of the nucleon
- the dissociation of the photon $|\gamma> \rightarrow |s\bar{s}>$
- a gluon coupling producing an $s\bar{s}$ pair.

Now consider the decays of the reaction products. The K^0 is not an eigenstate but is an equal mixture of two states called K^0_S (S for short, since the particle has a short lifetime) and K^0_L (L for long, as it has a longer lifetime). As the mean track length cτ for the K^0_L is 15.51 m (as opposed to cτ = 0.027 m for the K^0_S), the K^0_L particles will rarely decay within the CLAS detector system. Because of this, only the K^0_S particles are considered in the analysis and the missing K^0_L decay is accounted for as part of the branching ratio in the calculations of cross sections. The decay $K^0_s \rightarrow \pi^+\pi^-$, has its quark content written as $|d\bar{s}> \rightarrow \ |u\bar{d}> \ + \ |d\bar{u}>$. Through a weak interaction the $\bar{s}$ produces a $\bar{d}$ while a $u\bar{u}$ pair from the sea quarks enters the decay products. In this weak decay strangeness is not conserved as the K^0 has a strangeness of +1 and the resultant pions have a strangeness of zero.

The Σ^+ decays 51.6 % of the time into $p\pi^0$ and 48.3 % of the time into $n\pi^+$. The decay of the Σ^+ into a proton and neutral pion ($\Sigma^+ \rightarrow p\pi^0$) can be written as $|uus> \rightarrow |uud> + |d\bar{d}>$. In this decay the *strange* quark decays through a weak interaction into a *down* quark and a $d\bar{d}$ or $u\bar{u}$ pair. Strangeness is not conserved in this weak decay as the Σ^+ has a strangeness of -1 and the decay products have a strangeness of zero. The Σ^+ also decays as $\Sigma^+ \rightarrow n\pi^+$ which can be written as $|uus> \rightarrow |udd> + |u\bar{d}>$. This decay has the same resultant quarks as $\Sigma^+ \rightarrow p\pi^0$ but they are combined as different particles. Table 1.1 [4] shows general properties of the particles K^0_S and Σ^+.

Table 1.1: Properties of K^0_S and Σ^+ [3]

Particle Properties	K^0_S	Σ^+
J^p(I)	$0^-(\frac{1}{2})$	$\frac{1}{2}^+(1)$
mass ($\frac{MeV}{c^2}$)	493.68 ± 0.02	1189.37 ± 0.07
$c\tau$ (cm)	2.676	2.396
major decay modes	$\pi^+\pi^-$ (68.61±0.28)%	$p\pi^0$ (51.57±0.30)%
	$\pi^0\pi^0$ (31.39±0.28)%	$n\pi^+$ (48.31±0.30)%

1.1.3 Kinematics

To learn more about the properties of certain particles and resonances, production experiments can be conducted. In these experiments, a high-energy beam of protons, pions, kaons or photons is incident on a target, and resultant particles from the reactions are detected and analyzed. As many resultant particles (including K_S^0 and Σ^+) are short-lived, experimentalists often have to rely on detecting decay products from the particles. These short-lived particles can have their momentum, direction and mass determined by using information from the decay products. For example, the mass of a short-lived particle can be determined from its decay products by using the method of invariant mass, where for the decay $A \to B + C$, the invariance of the 4-momentum squared is used to obtain the squared invariant mass

$$M_A^2 = (E_B + E_C)^2 - (\vec{p}_B + \vec{p}_C)^2 \ . \tag{1.1}$$

For the decay $K_S^0 \to \pi^+\pi^-$ present in the reaction under consideration, this equation becomes

$$M_{K_S^0}^2 = (E_{\pi^+} + E_{\pi^-})^2 - (\vec{p}_{\pi^+} + \vec{p}_{\pi^-})^2 \ . \tag{1.2}$$

By looking at combinations of invariant masses from decay products, experimentalists can identify and observe the behaviors of resonance particles.

Along with the method of invariant mass, the method of missing mass is often used. Consider for example the reaction $A + B \to C + D + X$ where the momenta of the incoming particles A and B are known and only the outgoing particles C and D are detected. The mass of the undetected particle X is determined by using conservation of energy and momentum and writing

$$M_X^2 = (E_A + E_B - E_C - E_D)^2 - (\vec{p_A} + \vec{p_B} - \vec{p_C} - \vec{p_D})^2 \tag{1.3}$$

where E_i is the energy of a particle and $\vec{p_i}$ is the three-momentum of that particle.

For example, in this analysis one equation used is

$$M_X^2 = (E_\gamma + E_t - E_{\pi^+} - E_{\pi^-})^2 - (\vec{p_\gamma} + \vec{p_t} - \vec{p_{\pi^+}} - \vec{p_{\pi^-}})^2 \tag{1.4}$$

(where t refers to the target proton) which for the reaction $\gamma p \to \mathrm{K}^0\Sigma^+$ should be close to the mass of a Σ^+.

Since the target proton has no initial momentum in the laboratory, $\vec{p_t} = 0$ and $E_t = m_t$.

Both of these methods are used in the analysis of the data. Throughout this document, natural units are used where c=$\hbar$=1.

The kinematics for the reaction under consideration in this thesis, $\gamma p \rightarrow \mathrm{K}^0\Sigma^+$, are sketched in Fig. 1.1. The incident photon carries the momentum $\vec{k}$, whereas the produced meson has momentum $\vec{q}$. The production angle $\theta^{cm}_{K^0_S}$ is defined as the angle between the beam direction (z-axis) and the outgoing K^0_S.

For two-body reactions the kinematics are often specified by the Lorentz-invariant Mandelstam variables, where p_1 and p_2 are the 4-momenta of the incident particles and p_3 and p_4 are the 4-momenta of the outgoing particles:

$$s = (p_1 + p_2)^2 = (p_3 + p_4)^2 \tag{1.5}$$

(the square of the total energy in the center-of-mass system),

$$t = (p_1 - p_3)^2 = (p_2 - p_4)^2 \tag{1.6}$$

(the square of the 4-momentum transfer from particle 1 to particle 3), and

$$u = (p_1 - p_4)^2 = (p_2 - p_3)^2 \tag{1.7}$$

(the 4-momentum transfer squared from particle 1 to particle 4). These variables satisfy the equation

$$s + t + u = m_1^2 + m_2^2 + m_3^2 + m_4^2 \; . \tag{1.8}$$

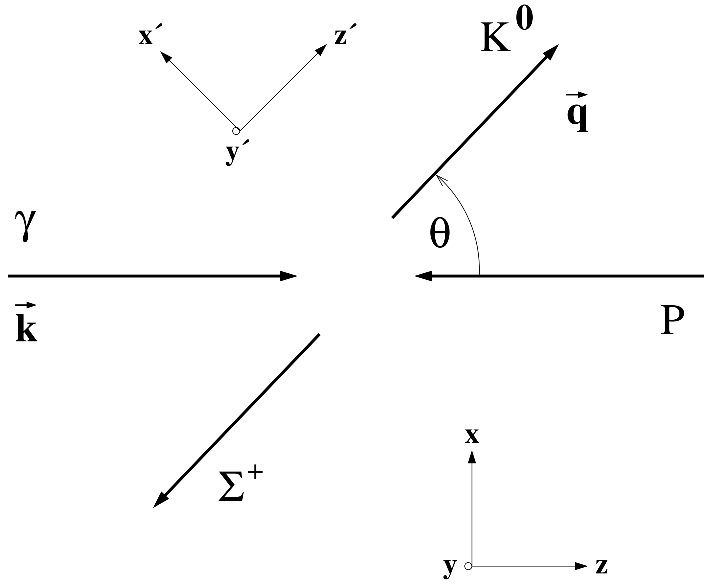

Figure 1.1: Kinematics for the reaction $\gamma p \rightarrow \mathrm{K}^0\Sigma^+$ in the center-of-mass frame. $\vec{k}$ is the momentum of the incoming photon (whose 4-vector is $p_1 = (E_\gamma, \vec{p_\gamma}))$ and $\vec{q}$ is the momentum of the outgoing K_S^0 (whose 4-vector is $p_3 = (E_K, \vec{p_K}))$. The axis on the bottom is for the center of mass frame, and the primed axis is for the center of mass frame of the K_S^0.

1.1.3.1 Cross sections

A cross section represents the probability of interaction per incident particle and per target particle per unit area.

For a reaction of two initial particles with masses m_1 and m_2 and 4-momenta p_1 and p_2 and two resultant particles m_3 and m_4, the differential cross section can be obtained from the transition matrix element M_{fi} by

$$d\sigma = \frac{(2\pi)^4 |M_{fi}|^2}{4\sqrt{(p_1 p_2)^2 - (m_1 m_2)^2}} d\phi_n(s; p_3, p_4) \; . \tag{1.9}$$

The transition matrix element M_{fi} is written as the coherent sum of the complex transition amplitudes T_n as $M_{fi} = T_1 + T_2 + T_3 ....$.

Feynman diagrams describe interactions between particles and can be used to calculate amplitudes for those interactions. Thus the theoretical cross section can be obtained through the coherent sum of various Feynman diagrams that represent the different intermediate states. Figure 1.2 shows tree-level Feynman diagrams for the reaction $\gamma p \rightarrow \mathrm{K}^0\Sigma^+$. In this figure, the Born terms are grouped on the left while the isobar terms are grouped on the right. These diagrams are separated into s-channel, t-channel and u-channel diagrams. Translating the visual diagram into the transition matrix M_{fi}, the vertices are assigned coupling constants based on the particle lines leading into and out of that vertex. The coupling constant $g_{\gamma pp}$ corresponds to the vertex on the first Feynman diagram for s-channel processes connecting the lines for γ and the two protons. Propagation operators are assigned for each intermediate particle in a diagram. These elements which are incorporated in various ways in different theoretical models are used to calculate cross sections for reactions.

Considering the spectrum for the production of hadrons as a function of incident photon energy, there are some strong peaks corresponding to the formation of resonances. For the energy dependence of the cross section for a reaction between two particles A and B near a resonance energy E_0 the Breit-Wigner formula is used 4

$$\sigma_f(E) \;\propto\; \frac{\pi(2J+1)}{|\vec{p}^{CM}|(2s_a+1)(2s_b+1)} \frac{\Gamma_i \Gamma_f}{(E-E_0)^2 + \frac{\Gamma_{tot}^2}{4}} \; , \tag{1.10}$$

where s_a and s_b are the spins of the reacting particles, Γ_i and Γ_f are the partial widths of the resonance in the initial and final decay channels. The lifetime τ is given as $\tau = \frac{1}{\Gamma}$, and Γ_{tot} is the sum of partial widths of all possible decay channels.

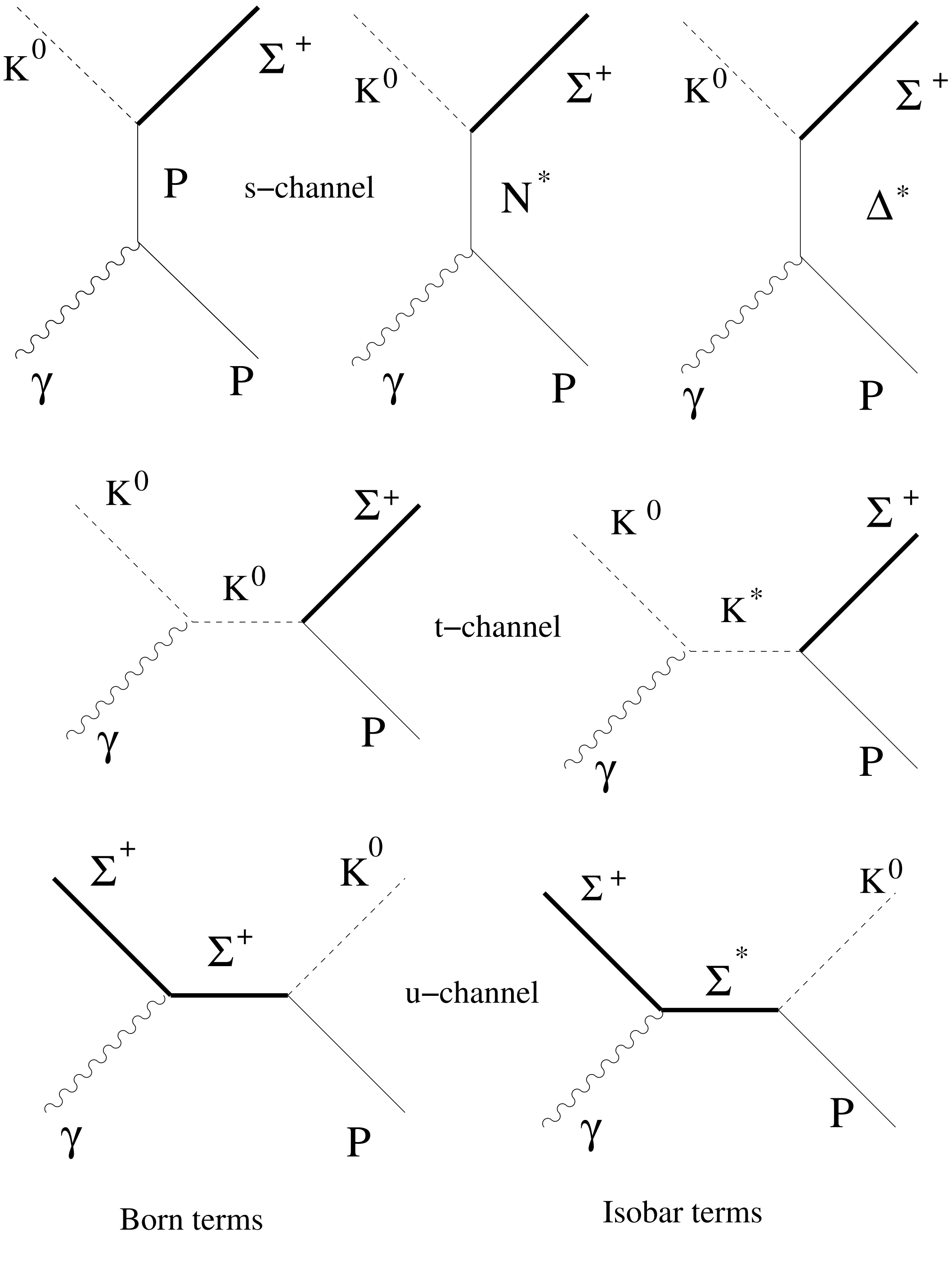

Figure 1.2: Feynman diagrams for the reaction $\gamma p \rightarrow\rightarrow \mathrm{K}^0\Sigma^+$.

1.2 Theoretical models

Theoretical physicists develop models that describe reaction mechanisms and give predictions which can be compared with experimental results. Many experiments have produced data for K^+ photoproduction, but there are only a few data points (with very limited statistics) for K^0 photoproduction.

1.2.1 Isobar models

1.2.1.1 Adelseck-Saghai

Adelseck and Saghai [5] analyzed the reaction $\gamma p \rightarrow K^+\Lambda$ using an isobar model and diagrammatic techniques to construct a Lorentz-invariant operator. Their analysis used lowest-order Feynman diagrams to represent the Born terms and contributions from resonances. They considered effects from all known spin-$\frac{1}{2}$ and spin-$\frac{3}{2}$ nucleon resonances, contributions from all known spin-$\frac{1}{2}$ Λ and Σ resonances, and the lowest kaon resonances. The KYN coupling constants were obtained through a least-squares search of available data. The photoproduction operator was found from selected first-order Feynman diagrams including nucleon, hyperon and kaon exchange terms. They specifically obtained the $g_{K\Lambda N}$ and $g_{K\Sigma N}$ coupling constants from kaon-nucleon scattering data.

1.2.1.2 Williams, Ji and Cotanch

Williams, Ji and Cotanch [6] used a hadron-pole model with coupling parameters constrained through an analysis of Λ, Σ^0 and $\Lambda(1405)$ production. Through a duality correction they represented the effects of higher spin s- and u-channel resonances, the N^*, Δ^* and Y^* states, by low mass t-channel K^* resonances in an attempt to reduce double counting effects. This reduced the number of diagrams required for their phenomenology and allowed one pole in the t-channel to represent the average of a set of higher spin resonances. In their model they included electromagnetic form factors extracted from existing experimental data.

1.2.1.3 Mart and Bennhold

Mart and Bennhold [7] compared existing data for the reactions $\gamma p \rightarrow \mathrm{K}^0\Sigma^+$ and $\gamma n \rightarrow \mathrm{K}^+\Sigma^-$ to models created for the reactions $\gamma p \rightarrow \mathrm{K}^+\Sigma^0$ and $\gamma p \rightarrow \mathrm{K}^+\Lambda$. They showed that the coupling constants for different processes can be related. This constricted the theoretical models since a given model could be tested against experimental data for more than one reaction. Notably they obtained the relations

$$g_z = g_{K^+\Sigma^0 P} = -g_{K^0\Sigma^0 N} = \frac{1}{\sqrt{2}} g_{K^0\Sigma^+ P} = \frac{1}{\sqrt{2}} g_{K^+\Sigma^- N} \; . \tag{1.11}$$

They also obtained relations among coupling constants of various Δ resonance contributions:

$$G_\Delta = G_{K^+\Sigma^0\Delta^0} = -\sqrt{2} G_{K^0\Sigma^+\Delta^+} = G_{K^0\Sigma^0\Delta^0} = \sqrt{2} G_{K^0\Sigma^-\Delta^0} \; . \tag{1.12}$$

The model of Mart and Bennhold combines data for the photoproduction and electroproduction of $\mathrm{K}^+\Sigma^0$, $\mathrm{K}^+\Sigma^-$ and $\mathrm{K}^0\Sigma^+$. This leads to very strong constraints on leading coupling constants. They believe that this was the first model to make use of data from charged Σ reactions. This model contains the standard Born terms, intermediate Λ- and K^*-exchange, the N^* resonances $S_{11}(1900)$ and $P_{11}(1710)$, and for Σ photoproduction only the Δ resonances $S_{31}(1900)$ and $P_{31}(1910)$. They only included the $K_1(1270)$ t-channel resonance in $\mathrm{K}\Lambda$ production as they found no sensitivity to this in $\mathrm{K}\Sigma$ production. This model was fit to all four reactions $\gamma p \to \mathrm{K}^0\Sigma^+$, $\gamma n \to \mathrm{K}^+\Sigma^-$, $\gamma p \to \mathrm{K}^+\Sigma^0$ and $\gamma p \to \mathrm{K}^+\Lambda$.

Figure 1.3 shows three different models fit to the experimental data for these reactions. The first model represents an older model from Bennhold [8] using Born terms and a Δ^* resonance at 1700 MeV, and was fit to $\mathrm{K}^+\Sigma^0$ photoproduction data. It is clear from the figure that this model greatly overpredicts the charged Σ photoproduction cross sections. This could be attributed to the Born coupling constants which are much larger in this model than in the others. The second model from Williams, Ji and Cotanch [6] includes several low lying s-, u- and t-channel resonances. This model was fit to photoproduction and electroproduction data for $\mathrm{K}^+\Lambda$, $\mathrm{K}^+\Sigma^0$, and $K^+\Lambda^*(1405)$, but was not fit to charged Σ data. This model agrees with the charged Σ data better than the first model, but it has a very poor fit to the $\mathrm{K}^+\Sigma^0$ data above the photon energy 1.5 GeV. The third model shown is from Mart and Bennhold with a fit to all available $K^+\Sigma^0$ data before 1995. The figure shows this model also has a very poor fit to the charged Σ data. Mart and Bennhold showed in this paper that including the $\gamma p \to \mathrm{K}^+\Sigma^0$ and $\gamma p \to \mathrm{K}^0\Sigma^+$ photoproduction data reduces the Born coupling constants $g_{\Sigma KN}$ and $g_{\Lambda KN}$ by an order of magnitude, so the description of the processes becomes much more resonance dominated. This illustrates the importance of $\gamma p \to \mathrm{K}^0\Sigma^+$ experimental data in refining theoretical models. Newer investigations of Λ photoproduction [9] show that a previously unknown resonance $D_{13}(1895)$ must be included to fit the experimental data. Mart and Bennhold's predictions have been utilized in a program called KAON-MAID [10]. This program can be run for different reactions with various resonances present or absent.

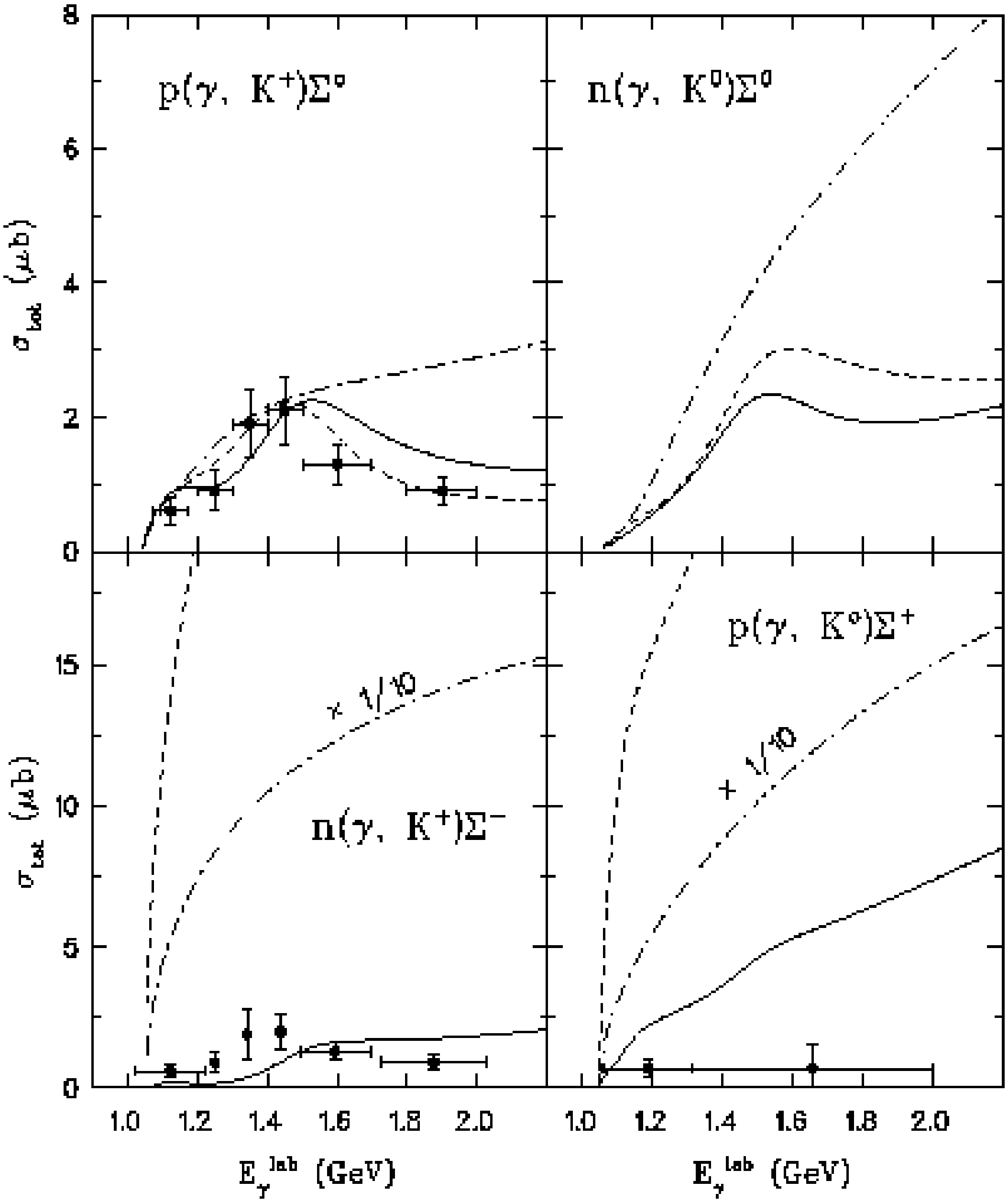

Figure 1.3: Total cross section for four isospin channels in $K\Sigma$ photoproduction in comparison with three model predictions. The dash-dotted line is from a model by Williams, Ji and Cotanch [6]. The dashed curve represents an older model from Mart and Bennhold [8] using Born terms and fit to $K^+\Sigma^0$ photoproduction data. The solid curve is a more recent model from Mart and Bennhold [7] fit to all previous experimental data except charged Σ data. The experimental data points are from [11]

1.2.2 The coupled channel analysis of Feuster, Penner and Mosel

The theoretical approach taken by Penner and Mosel (based on earlier work collaborating with Feuster) [12] is to analyze all available experimental data on photon- and pion-induced reactions on the nucleon to develop a unitary coupled-channel effective Lagrangian model. They believe that a single-channel analysis can not adequately take into account background contributions and rescattering effects. In their model, they use the same Lagrangians for pion- and photon-induced reactions, so different reactions can be analyzed consistently with similar aspects of the model. The background is generated dynamically from u- and t-channel contributions without new parameters. Other models, called T-matrix models [13, 14, 15] are based on single-channel effective Lagrangian calculations and ignore rescattering effects. Their model includes nucleon Born contributions for ω production, which causes it to overestimate the data above 1.7 GeV. To better approximate experimental data Penner and Mosel believe that one has to either ignore these contributions or use very soft form factors.

Penner and Mosel compare all channels simultaneously to experimental data. The sets of experimental data include $\gamma N \rightarrow \pi$ N, $\gamma N \rightarrow \pi\pi$ N (these data are included in rescattering effects but are not directly compared to the model), $\gamma N \rightarrow \omega$N for which ABBHHM [16] and SAPHIR [18] data are included,$\gamma N \rightarrow \gamma$ N, $\gamma N \rightarrow \eta$N, $\gamma N \rightarrow$KΛ for which SAPHIR cross section and Λ polarization data are included [18], and $\gamma N \rightarrow$K Σ for which experimental data for $\gamma p \rightarrow K^+\Sigma^0$ and $\gamma p \rightarrow K^0\Sigma^+$ from ABBHHM and SAPHIR are included [16, 18, 19]. In total they used 4400 photo-induced and 2400 pion-induced data points in their fits. In their first attempts at including photoproduction data [20, 21], they kept hadronic parameters fixed to their values from the fits using pion-induced reactions, but these parameters were found to not reproduce the photoproduction data. Their new expanded model and data set now constrains the production mechanisms more strongly, especially above 1.7 GeV where photoproduction data for all reactions have become available. Since there are no good data at energies above 1.7 GeV for pion-induced ηN and ωN production, these production mechanisms have not been properly decomposed in purely hadronic calculations, which leads to contradictions in the photoproduction reactions when the hadronic parameters were kept fixed. For associated strangeness production, the Born terms play a minor role in the pion-induced reactions, but due to the gauging procedure, their effects are enhanced in photoproduction. This leads to a more reliable determination of the corresponding couplings. When their hadronic parameters are kept fixed, the experimental KΛ and KΣ photoproduction data do not fit the model. Only when the hadronic parameters are allowed to vary a simultaneous fit to all pion- and photon-induced reactions is possible. This means that the experimental data for all these reactions are compatible with each other as far as partial wave decomposition and unitary effects.

Penner and Mosel develop theoretical predictions for the $\gamma p \rightarrow K^0\Sigma^+$ photoproduction reaction, as shown in Fig. 1.4. They take the four best hadronic fits with parameters based on existing data. These fits are labeled $C - p\gamma\pm$ and $C - t\gamma\pm$ where C indicates they are using spin-$\frac{3}{2}$ couplings with spin-$\frac{1}{2}$ off-shell contributions and the p or t indicates which of two form factors(F_p or F_t) is used in the t-channel diagrams.

The equations for these form factors are:

$$F_p(q^2, m^2) = \frac{\Lambda^4}{\Lambda^4 + (q^2 - m^2)^2} \,, \tag{1.13}$$

$$F_t(q^2, m^2) = \frac{\Lambda^4 + \frac{1}{4}(q_t^2 - m^2)^2}{\Lambda^4 + (q^2 - \frac{1}{2}(q_t^2 + m^2))^2} \,. \tag{1.14}$$

The γ indicates a photoproduction reaction (similar hadronic fits exist for pion produced data) and the sign corresponds to the unknown sign of the coupling constant $g_{\omega\rho\pi}$. Penner and Mosel were not able to obtain a good global fit using the form factor F_t for the t-channel exchange diagrams so they chose instead to use the form factor F_p for all vertices and for t-channel meson exchange. The form factor F_p was found to apply well to a much larger kinematic range at higher energies than F_t. Thus they decided to utilize photoproduction results of the global calculation $C - p\gamma\pm$ rather than $C - t\gamma\pm$.

The authors attempt to simultaneously describe both measured charged Σ photo-induced reactions while still agreeing with all three charged pion-induced channels. They found that KΣ was sensitive to scattering effects via ωN. The ωN channel feeds the $IJ^p = \frac{1}{2}\frac{1}{2}^-$ KΣ wave which leads to a sudden increase in both the $K^0\Sigma^+$ and $K^+\Sigma^0$ total cross sections as a function of energy. They noted that the finite width (8 MeV) of the ω meson smears out this threshold effect, but this aspect is not included in this model.

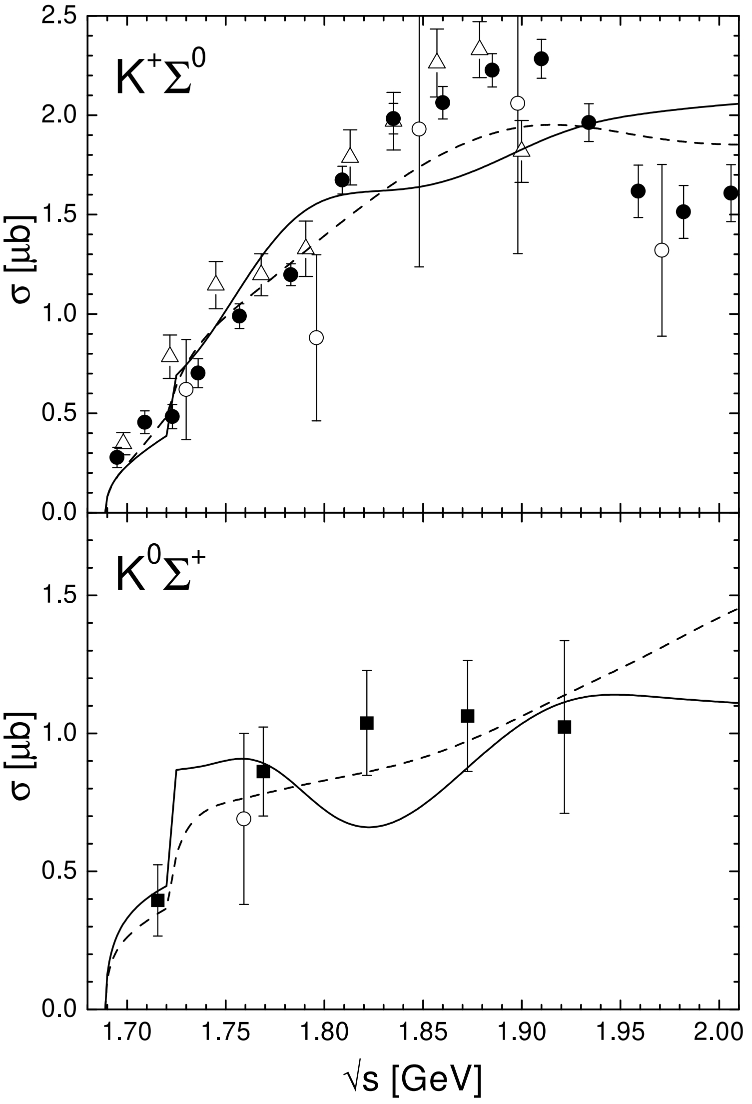

Figure 1.4: Penner and Mosel's theoretical predictions for total cross section in comparison with previous experimental data. The lower plot shows SAPHIR data [17] (solid squares) and ABBHHM data [16] (open circles) for the reaction $\gamma p \rightarrow \mathrm{K}^0\Sigma^+$ plotted with two hadronic fits from Penner and Mosel: the solid line for $C - p\gamma+$ and the dotted line for $C - p\gamma-$.

Penner and Mosel compared their model to one by Janssen *et al.* [22] in which a tree level isobar model is used and the D_{13} wave is excluded. Using that model Janssen identified important contributions from $P_{11}(1710)$ and $S_{11}(1650)$ which are also contained in the Penner and Mosel model. But where Janssen identifies contributions from $P_{13}(1720)$, $S_{31}(1900)$ and $P_{31}(1910)$, Penner and Mosel's model instead identifies contributions from the resonances $P_{13}(1900)$, $S_{31}(1620)$ and $P_{31}(1750)$. Penner and Mosel do not find significant contributions from $S_{31}(1900)$ or $P_{31}(1910)$ in their model. Clearly much better data are needed to accurately determine the contributions from the different resonances. SAPHIR data, as shown in Fig. 1.4 and 1.5, are not accurate enough to distinguish between these calculations.

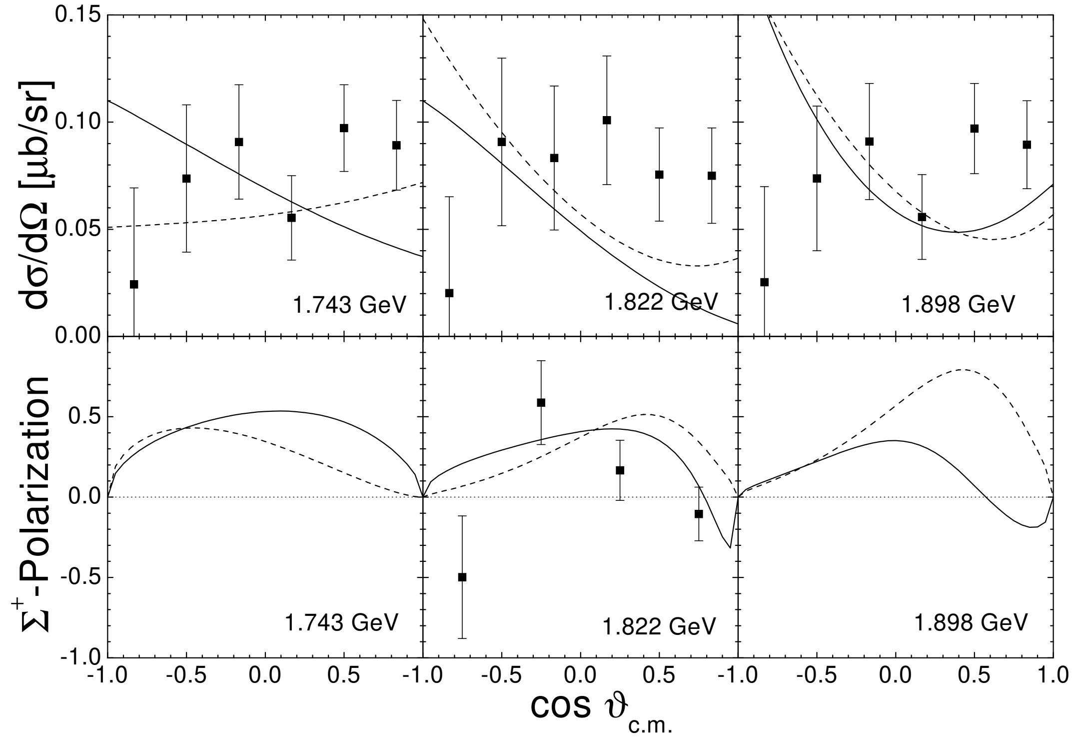

Figure 1.5: Penner and Mosel's theoretical predictions for differential cross sections in comparison with previous experimental data. Differential cross sections and Σ^+ polarization from SAPHIR data [17] and ABBHHM data [16] for the reaction $\gamma p \to K^0\Sigma^+$ are plotted with two hadronic fits from Penner and Mosel: the solid line for $C - p\gamma+$ and the dotted line for $C - p\gamma-$. These plots are for W values of 1.743, 1.822 and 1.898 GeV as indicated on the figures.

Figure 1.6 shows the partial wave decomposition of C-pγ+ for the total cross section. In these calculations for $K^0\Sigma^+$, there is a noticable contribution from the $P_{11}(1710)$ as seen in the $J^P = \frac{1}{2}^+$ contribution and from the $J^P = \frac{3}{2}^+$ contributions due to the $P_{33}(1920)$ and $P_{13}(1900)$. The $J^P = \frac{3}{2}^-$ and contributions from higher partial wave analysis do not significantly contribute to the total result as shown by the figure. The authors believe that the angular structure of cross sections for $K^0\Sigma^+$ is well described by their model. They ascribe the decrease in cross section at forward angles for higher energies to the K^* exchange. It is clear that better $K^0\Sigma^+$ data would improve the judgement of the quality of their fit. In Section 5.4.1 our experimental results are compared with their theoretical predictions.

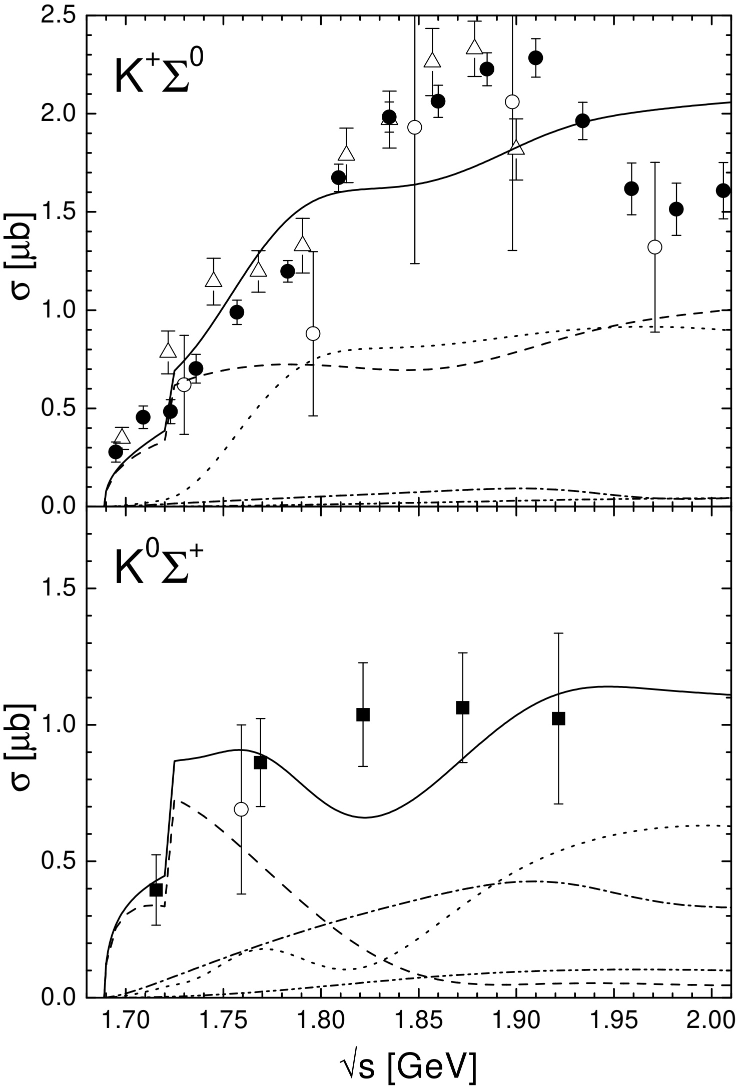

Figure 1.6: Penner and Mosel's partial wave decomposition of $C - p\gamma +$ for the total cross section plotted with previous experimental data. The dashed line is for resonances with $J^P = \frac{1}{2}^-$, the dotted line for $J^P = \frac{1}{2}^+$ (including the $P_{11}(1710)$), the dash-dotted line for $J^P = \frac{3}{2}^+$ (including the $P_{33}(1920)$ and $P_{13}(1900)$) and the dash-double-dotted line for $J^P = \frac{3}{2}^-$. The solid line is the sum.

1.3 Existing experimental data

1.3.1 ABBHHM

The Aachen-Berlin-Bonn-Hamburg-Heidelberg-Muenchen Collaboration (ABBHHM) used the hydrogen bubble chamber at DESY to study photoproduction on protons in the photon energy range 0.3 to 5.8 GeV [16]. Results were published in 1969 based on 31,000 analyzed events where three or more outgoing charged particles were detected. Their analysis involved a kinematic fit, which does not allow for analyzing reactions with more than one neutral particle. When analyzing reactions with only one neutral particle such as $\gamma p \rightarrow n\pi^+\pi^+\pi^-$ and $\gamma p \rightarrow p\pi^+\pi^-\pi^0$, the kinematics were uniquely determined and the calculated photon energy (determined from a photon tagging system) was correct within the measurement errors. This experiment analyzed various reactions simultaneously. The number of events found and corrected for scanning losses for the reaction $\gamma p \rightarrow n\pi^+\pi^+\pi^-$ was 6800 and for the reaction $\gamma p \rightarrow p\pi^+\pi^-\pi^0$ was 3050. For the reaction $\gamma p \rightarrow \mathrm{K}^0\Sigma^+$ only 6 unique events were identified, which was increased to 18 events after their apportionment of ambiguous events. These events were determined using a three constraint fit and by observing the compatibility of the observed bubble density with the calculated density. For the reaction $\gamma p \rightarrow \mathrm{K}^0\Sigma^+$, this experiment resulted in two points for the total cross section as a function of photon energy. A measurement of the differential cross section for this reaction was not attempted due to the small number of events.

1.3.2 SAPHIR

More recently, data from the reaction $\gamma p \rightarrow \mathrm{K}^0\Sigma^+$ up to 1.55 GeV in photon energy were obtained using the SAPHIR detector at the electron stretcher ring ELSA in Bonn, Germany [17]. The data analysis was based on events where three charged particles had been detected. The decay channels $\Sigma^+ \rightarrow p\pi^0$, $\Sigma^+ \rightarrow n\pi^+$, and $K^0 \rightarrow \pi^+\pi^-$ were analyzed. The selection of events required that the invariant mass and missing mass of combinations of detected particles match the decaying final state particles(K^0_S, Σ^+). Their analysis procedure included four steps to identify an event. Their first step was to reconstruct the K^0_S and its decay vertex, performed through a kinematic fit with the negatively charged track and the most appropriate of the positively charged tracks. The invariant mass of these tracks had to be consistent with the K^0_S mass, and any mass predictions from their time-of-flight measurements of these particles had to be consistent with the mass of a pion. After the complete event selection was performed, they were certain that the proper combination of π^+ and π^- particles was chosen to reconstruct the K_S^0. The Σ^+ was identified through missing mass techniques, as the K_S^0 was already identified and the incoming photon energy was measured by a tagging system. When the missing mass $MM(\gamma p \to K_S^0 X)$ was consistent with that of a Σ^+, a kinematic fit was performed to obtain the kinematics of the primary reaction and the 3-momentum of the Σ^+ at the primary vertex. After this step, the primary vertex and the decay of the Σ^+ were reconstructed. The primary vertex was determined to be on the track of the reconstructed K_S^0, inside the target. If the K_S^0 decayed within the target, the intersection of the K_S^0 track with the boundary of the target was taken to be the point of decay. The Σ^+ decay vertex was sought by testing potential primary decay vertices inside the target along the K_S^0 track. The best primary vertex and Σ^+ decay vertex were chosen by considering points along this line and their consistency with the track of the third detected, charged particle which decays from the Σ^+ (either a p or π^+). After these vertices were chosen, kinematic fits were performed to both decay channels, $\Sigma^+ \to p\pi^0$ and $\Sigma^+ \to n\pi^+$. The better fit of those two was chosen, also considering the proper relation between the decay channel and the mass of the charged particle detected from the Σ^+ decay. Finally, an overall kinematic fit was performed to the reaction $\gamma p \to \mathrm{K}^0\Sigma^+$ and either $\Sigma^+ \to p\pi^0$ or $\Sigma^+ \to n\pi^+$. If the probability of the fit was good and greater than that of background reactions, the event was accepted. Experimental results from SAPHIR are presented along with our experimental data in Section 5.3. Monte-Carlo simulations were performed for the SAPHIR experiment to estimate the contributions from background processes, with the conclusion being that the largest background contribution comes from the reaction $\gamma p \to p\pi^+\pi^-\pi^0$. The SAPHIR experiment resulted in identifying 405 unique events. They were not able to identify any structure in the differential cross section of $\gamma p \to \mathrm{K}^0\Sigma^+$ due to large statistical uncertainties.

Our analysis has similarities to that of the SAPHIR experiment, including identifying the K_S^0 and Σ^+ by invariant-mass and missing-mass techniques. A similar type of distance cut for this analysis was considered (as described in section 4.2.4), but not used because of the poor resolution for determining the location of the vertex due to the large size of the CEBAF photon beam and the comparatively large distance to the inner tracking chamber.

Table 1.2: Comparing data for $\gamma p \to \mathrm{K}^0\Sigma^+$ for the ABBHHM, SAPHIR and CLAS experiments.

	ABBHHM	SAPHIR	CLAS
Identified events	18	405	17500
Maximum photon energy	2.0 GeV	1.55 GeV	2.35 GeV

Chapter 2

Experimental setup

2.1 Jefferson Lab

This experiment was conducted at the Thomas Jefferson National Accelerator Facility (JLAB) in Newport News, Virginia. This facility contains an electron accelerator (CEBAF) which operates with superconducting RF cavities to drive the electrons to high energies. A refrigeration plant creates temperatures around 1.8° K for superconducting operation. Figure 2.1 shows the two parallel linacs which are used to boost the beam energy during up to five loops around the track to a maximum of 6.0 GeV before beam delivery to the end stations. The electron beam is split into three separate beams and transported to three end stations, called "halls", for simultaneous data taking on different experiments. The "continuous" electron beam (actually only macroscopically continuous) has a 1.499 GHZ RF microstructure. A pulse in sync with the RF structure (hereafter referred to as "RF signal") provides an accurate timing signal that allows multiparticle coincidences to be measured at high rates.

2.2 CLAS

This experiment took place in Hall B using a tagged bremsstrahlung photon beam. Figure 2.2 shows the CEBAF Large Acceptance Spectrometer (CLAS) which is a large acceptance detector (approximately 70 % of 4π steradians) located in Hall B of Jefferson Lab [23]. Six iron-free superconducting coils centered on the beam line create a toroidal magnetic field which can be adjusted up to 2 tesla, with a maximum field integral of 2.5 tesla·meter in the forward direction. These six coils divide CLAS into six azimuthal

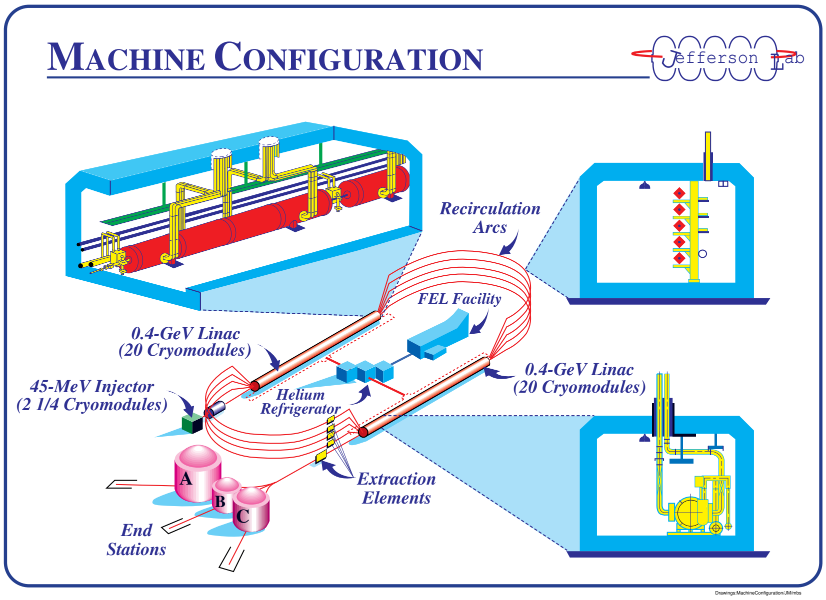

Figure 2.1: (CEBAF) at the Thomas Jefferson National Accelerator Facility (JLAB)

sectors each containing three multilayer drift chambers (DC) [24] which are used to determine the trajectories and momenta of charged particles produced from a fixed target on the toroidal axis. Region 1 of the drift chambers is closest to target and beam line and operates in a region with almost no magnetic field. This region is used to determine the initial trajectory of charged particles. Region 2 is located inside the strong magnetic field between the torus coils and is used to obtain a measurement of the particle track at a point of maximum curvature. Region 3 rests outside the torus coils in a low magnetic field area and is used to further determine the trajectory of charged particles before they hit other detectors including the time-of-flight(TOF) counters, the forward electromagnetic calorimeter(EC) and large angle calorimeter(LC). These calorimeters consist of alternating layers of lead and scintillator strips attached to photomultiplier tubes. The forward calorimeter, covers lab angles from 8° to 45° in all six sectors and the LC covers 45° to 70° in two sectors [25].

2.2.1 Target

A liquid hydrogen target was used for this experiment, with the target cell walls made of kapton. The length of the target was determined to be 178.5 ± 0.5 mm. The temperatures and pressures associated with the target were measured at the start of each run, which remained mostly constant over the period of running. For the 2.445 GeV beam energy running period, the average density of the target was found to be 0.0711 g/cm^3 [28]. The target is surrounded by a set of scintillation counters which – in coincidence with the time-of-flight counters – allow for determining the flight time of charged particles.

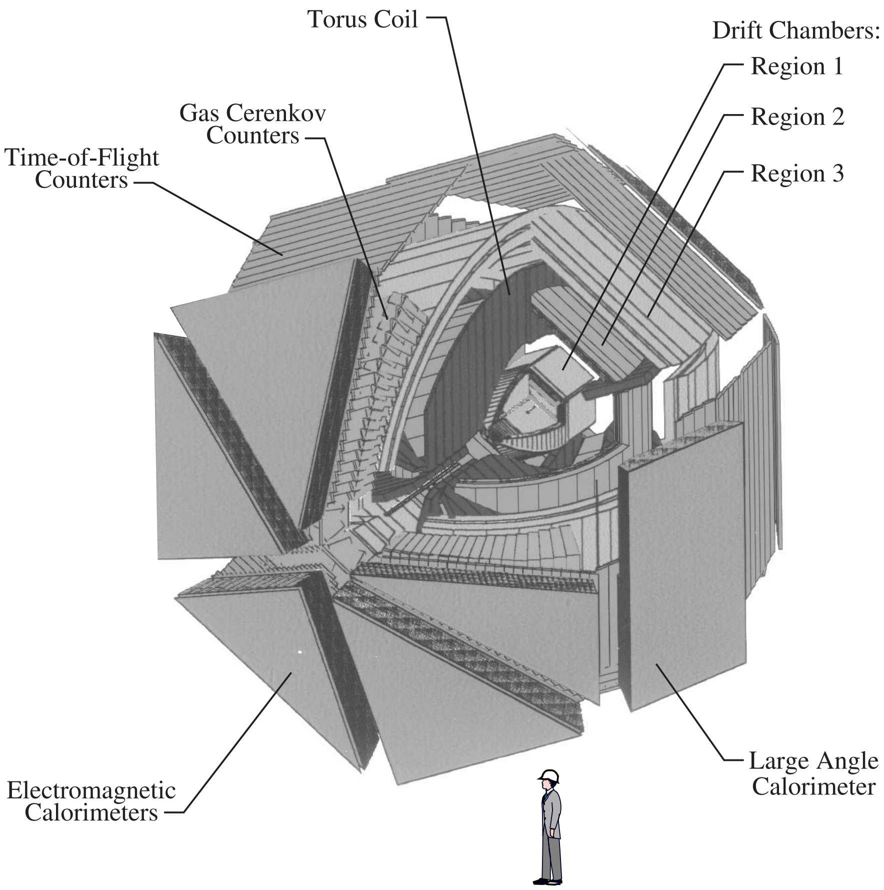

Figure 2.2: The CEBAF Large Acceptance Spectrometer (CLAS). The Gas Cerenkov Counters and the Calorimeters were not used in this experiment.

2.3 Data acquisition

2.3.1 Event trigger

The recording of an interaction (called an "event") is initiated by the CLAS event trigger, called the "level 1" trigger. This requires a coincidence between hits in the tagger, start counter, and time-of-flight paddles. Thus, even a single charged particle exiting the target and striking a TOF counter, in coincidence with a tagged photon, will initiate data recording for the event. Signals from all 61 T-counters are "OR"ed together to produce what is called a "master-OR".

2.3.2 Photon energy and time

2.3.2.1 The Hall B tagging system

For photoproduction experiments in Hall B, the CEBAF electron beam is used to produce tagged photons, whose energy is determined by the Hall B tagging system [29]. The photon tagger can detect photon energies in a range from 20% to 95% of the incident electron energy, and operate with electron beam energies up to 6.1 GeV. The electron beam hits a thin bremsstrahlung radiator, typically a gold foil with a thickness of 10^{-4} r.l. The electrons are then bent downwards by a dipole magnet while the photons pass through a hole in the magnet yoke and strike the target. Electrons which produce a photon are degraded in energy, bent through a larger angle by the tagger magnet.

2.3.2.2 The hodoscope

The scattered electrons are measured by a hodoscope which contains two arrays of plastic scintillators. The photon energy is determined by an array of 384 partially overlapping small (0.4 cm thick) scintillators called "E-counters" while the timing resolution used to form a coincidence with the corresponding nuclear reaction triggered by the tagged photon is determined by an array of 61 thicker (2 cm) scintillators, called "T-counters". The E-counters overlap by about $\frac{1}{3}$ of a scintillator width to create 767 E-channels of nearly equal energy with a width of $\approx$0.001 E_0. The E-channels are numbered in order of decreasing photon energy, with E_1 corresponding to $E_\gamma \approx$0.95 E_0 and E_{767} corresponding to $E_\gamma \approx$0.20 E_0. To minimize false signals from backscattered particles the E-counters were arranged perpendicular to the path of electrons passing

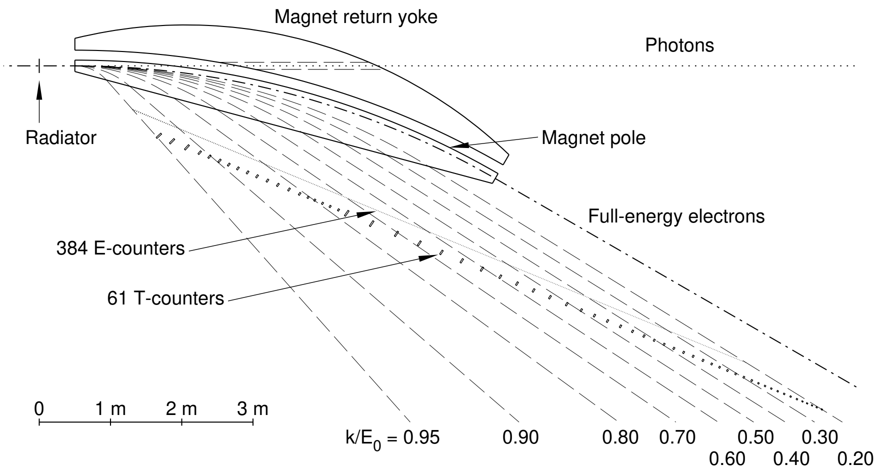

Figure 2.3: Layout of Photon Tagging System

through the focal plane. To minimize energy loss and scattering of electrons, the electrons travel within a vacuum chamber that extends almost to the E-counter plane. A thin vacuum window, composed of a layer of mylar supported by a mesh of kevlar, separates the vacuum chamber from the E- and T-counters [30]. The T-counters are also arranged perpendicular to the path of electrons passing through the focal plane. The T-counters overlap by about 10% of their width to eliminate potential gaps between T-counters. Because the outgoing bremsstrahlung electrons leave the radiator at very small angles, the electron trajectory is essentially dependent only on the ratio $\frac{E_\gamma}{E_0}$, so the coincidence pattern of hits in the E- and T-counters can be predicted. The comparisons between coincidences observed while taking experimental data and predicted from using the dipole field map are found to be in good agreement. The photon energy, E_γ, is determined by the equation $E_\gamma = E_0 - E'$ where E_0 is the incident electron energy and E' is the energy of the scattered electron detected in the tagging hodoscope. The photon flux actually striking the target was determined by comparing the rate in the tagger with that of a high efficiency total absorption counter (TAC) photon monitor. The photon rate was monitored during data taking by lower efficiency photon beam monitors.

2.3.2.3 Photon beam monitoring

The TAC is comprised of four lead-glass blocks attached to four photo-multipliers and is located downstream ($\approx$ 22 m) of the target. The TAC is almost 100% efficient in detecting photons but can be used only with low intensity beams, the total photon flux being no more than about 50 kHz. The TAC is used at this photon flux during special normalization runs. Two other downstream devices which incorporate scintillators are the pair spectrometer and pair counter [29]. These devices were used in early photon running in order to determine the photon flux. During the g1c run period, during which the present data were taken, these devices were only used for consistency checks.

2.3.3 Start counter

The start counter (SC) [27] is a set of six scintillators surrounding the target region in a distance of 10.2 cm from the target center. In conjunction with the time-of-flight counters, the start counters indicate an event coming from the target and define the velocity of the particle. Signals from phototubes in the start counter are summed and passed through a discriminator before being sent to determine an AND relation with the master-OR from the tagger's T-counters.

2.3.4 Particle trajectory via drift chamber

The drift chambers [24] measure the position of a track by detecting a signal produced when a charged particle passes through the gas within the chamber. As the charged particles pass through the chamber, they ionize the gas, an argon-CO_2 mixture. The "sense" wires are kept at a positive high voltage while the "field" wires, which are used to shape the electric field, are kept at a negative high voltage. Particles passing through the drift chamber ionize the gas and create electrons along the particle's path. These electrons move toward the sense wires due to the electric field, and are said to "drift" toward the sense wires, as collisions with molecules in the gas result in the electron moving at a comparatively low, almost constant velocity. As the electron is accelerated near the sense wire, it ionizes additional gas molecules, resulting in an increased number of electrons, hence creating a larger signal. The time when the electrons reach the sense wire is recorded and used to calculate the distance-of-closest-approach of the track to the sense wire. This distance is then used to fit to a trajectory of the track through the detectors.

2.3.5 Time-of-flight

The time-of-flight (TOF) system [26] is made up of scintillation counters of varying lengths so as to span the area between the coils. They cover an angular range measured from the initial beam direction from 8° to 150° in the laboratory. There are 57 counters per sector, with the backward counters combined to yield 48 "paddles". Signals from phototubes on each end of the time-of-flight paddles were summed, discriminated and then sent to the level-1 trigger logic. These signals are also used to obtain a position corrected time with a resolution of about 190 ps.

Chapter 3

Data Processing

The experimental and simulated data used in this analysis are processed before being analyzed. Figure 3.1 shows the steps taken to process the data before the analysis of physics events begins. Simulated events for the reaction sought, $\gamma p \rightarrow \mathrm{K}^0\Sigma^+$, as well as background reactions with the same final state particles are processed through *GSIM*, which is a GEANT [34] based Monte Carlo program which simulates the CLAS detector system. The program *GPP*, *GSIM* post-processing, removes dead drift chamber wires and time-of-flight counters, and smears the reconstructed position in the drift chambers to better approximate experimental data. The code *A1C* is then used to process the data into a form more useful for physics analysis. Experimental data first go through a calibration process which takes into account instabilities in the beam and detectors, then is processed through *A1C* as are the simulated data. Both simulated and experimental data are then filtered to separate the $\Sigma^+ \rightarrow p\pi^0$ and $\Sigma^+ \rightarrow n\pi^+$ decay channels, and to ensure (using broad mass cuts) that only the given four final decay particles are in the data set. These data are then ready for data analysis.

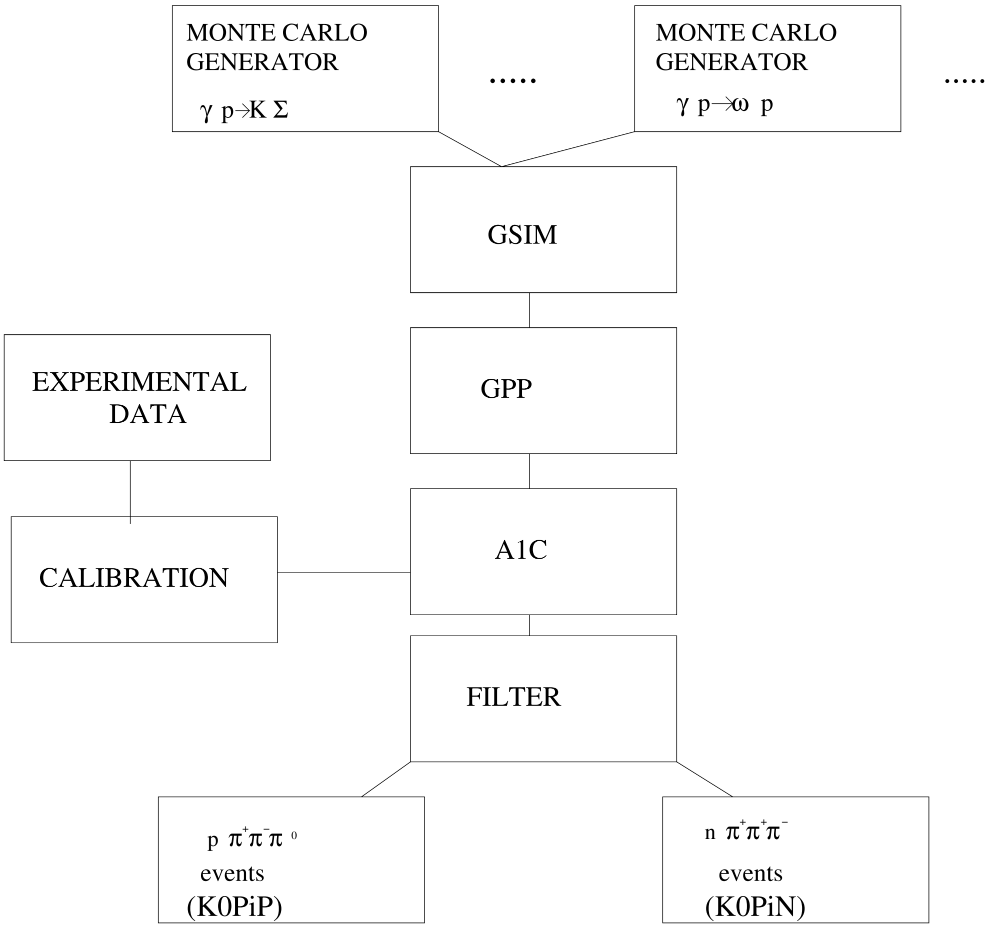

Figure 3.1: Flowchart for the processing of data. Starting from the top, simulated data are produced using a Monte Carlo generator for various reactions. The data are then processed through *GSIM* and *GPP*. They are then processed through the *A1C* reconstruction code. Experimental data, on the left, undergoes a calibration, and is then processed through the same *A1C* reconstruction code. After *A1C*, these events are filtered for either the final state particles p piz $\pi^+\pi^-$ (corresponding to $\gamma p \rightarrow \mathrm{K}^0\Sigma^+ \rightarrow p\pi^+\pi^-\pi^0$) or for the final state particles $n\pi^+\pi^+\pi^-$ (corresponding to $\gamma p \rightarrow \mathrm{K}^0\Sigma^+ \rightarrow n\pi^+\pi^+\pi^-$). All data, experimental and simulated, are processed in this manner before being analyzed by the analysis code.

3.1 Data set

The data analyzed in this experiment were taken during a running period at Jefferson Lab during October and November, 1999. This run period is referred to as g1c. The first data set was obtained with an electron beam energy of 3.115 GeV, the second set with an electron beam energy of 2.445 GeV. The 3.115 GeV data set had 10^9 triggers while the 2.445 GeV data set had 2.6x10^9 triggers. These electron beam energies correspond to photon beam energy ranges of 0.623 to 2.96 GeV for the first set and 0.489 to 2.32 GeV for the second set. Only events produced at photon energies between 1.15 and 2.35 GeV were considered in this analysis (the threshold energy for $\gamma p \rightarrow \mathrm{K}^0\Sigma^+$ is 1.048 GeV). The data were divided into segments called runs which were further divided into 2-gigabyte data files where each run had approximately 10 files. The data set includes about 120 runs for the 2.445 GeV data and about 150 runs for the 3.115 GeV data. The 3.115 GeV data set was in part taken with the full tagger range active and in part where only the upper portion (higher photon energy) of the tagger range ($\approx$ 0.5 to 0.95 of E_0) was active. Another data set at a beam energy of 2.8 GeV was investigated but discarded due to problems with the photon flux and low statistics. These two data sets were analyzed separately and the final cross section results were combined by weighted averages.

3.2 Data reconstruction

The raw data from each component of the CLAS detector consists of digitized information from time-to-digital converters(TDC), analog-to-digital converters(ADC), and scalers. They must be converted into data that can be used for physics analysis. In the analysis procedure used by the CLAS collaboration, both the raw data and the processed data are stored in a format called BOS banks. BOS [31] is a Fortran-77 based dynamic memory management system where a “bank” is a subset of data relating to a certain aspect of the data. The reconstruction program, *A1C*, calls several modules which convert data fromt all the detector components into quantities that are used to identify the particles and topologies. This analysis code uses reconstructed BOS banks. The tagger analysis reconstructs the time that the photon hits the center of the target and gives the energy of the photon. In order for an event to be accepted by the tagger software, there must be a coincidence between the T-counter and one of the appropriate E-counters. The track reconstruction uses the time information of hits in the drift chambers to fit the track parameters of charged particles traversing the chambers. Time-of-flight scintillator hits allow a determination of the given particle’s speed from the time and distance between the start counter and TOF scintillator planes. This trajectory then is projected backwards to a common vertex of the particles belonging to a single event, so a more accurate vertex time can be determined. This vertex time is then compared to various hits in the tagger bank. The hit in the tagger bank which is consistent with a photon hitting the target closest in time to the determined vertex time, within a timing resolution window, is recorded as the best tagger hit. This hit is used to determine the photon energy.

3.3 Data calibration

To reconstuct physics events from raw data, a data calibration [32] has to be performed in order to determine intrinsic parameters of the various CLAS detector components and to align their relative timings. This calibration has to take into account changes in beam energy and instabilities in the detector performance that are indicated in the monitoring. All high resolution timing information is recorded by TDCs operating in a common start mode, so the event trigger starts the recording time in various counters until a hit is detected and the elapsed time recorded. All time offsets in these various propagation times have to be taken into account for the proper reconstruction of data. The drift chamber TDCs are operated in common stop mode, thus a hit in the drift cell starts the recording time which is stopped by the delayed event trigger signal. While the pattern recognition using just the wires recording a signal (called "hit-based" tracking) can be used to reconstruct a rough particle trajectory in the drift chambers, a more accurate tracking using the drift time-to-distance relation (called "time-based" tracking) inside the drift cells requires timing alignment of the drift chambers. Time-of-flight measurements are based on information from the TOF scintillator, but a second time measurement is required to determine the speed of a particle detected in the CLAS detector. For photon running, this is obtained from the start counter in conjunction with the beam RF signal.

The calibration process determines and correlates sets of constants for each detector system which are stored in files called "maps". During reconstruction of the data, a list of dead channels is compiled which is then used to "knock out" these dead channels in Monte Carlo simulations and in the processing of experimental data. The tagger system is calibrated by aligning the E- and T-counter timings with the RF signal. The TOF scintillators were calibrated by optimizing the time and hit position reconstruction and by aligning the timing of the 288 paddles with each other and within the CLAS detection timing scheme. The start counter is calibrated by aligning the time information of the start counter paddles with respect to the tagger T-counters.

3.4 Particle identification

Particles are identified by calculating the mass from the time-of-flight and momentum. The mass is determined from the equations $E = \gamma mc^2$ and $\beta = \frac{pc}{E}$ which leads to $m = \frac{pc}{\gamma\beta} = pc\sqrt{\beta^{-2} - 1}$, where $\gamma = (1 - \beta^2)^{-\frac{1}{2}}$ and $\beta = \frac{L}{c\Delta t}$, and where Δt is the time-of-flight and L is the particle's path from the target to the given scintillator. The mass calculation depends thus on the quality of the reconstructed momentum, path length and time-of-flight. Particles with higher momentum are more energetic and bend less under the magnetic field, thus having a less precise resolution. The mass peaks for high momentum particles are therefore expected to be broader. This is evident in the mass peaks for detected pions for 2.445 GeV data shown in Fig. 3.2. A particle selection on the mass distribution is used to identify charged particles during processing and filtering of raw data. A more refined charged particle identification is used in the final analysis as presented in Section 4.2.1.

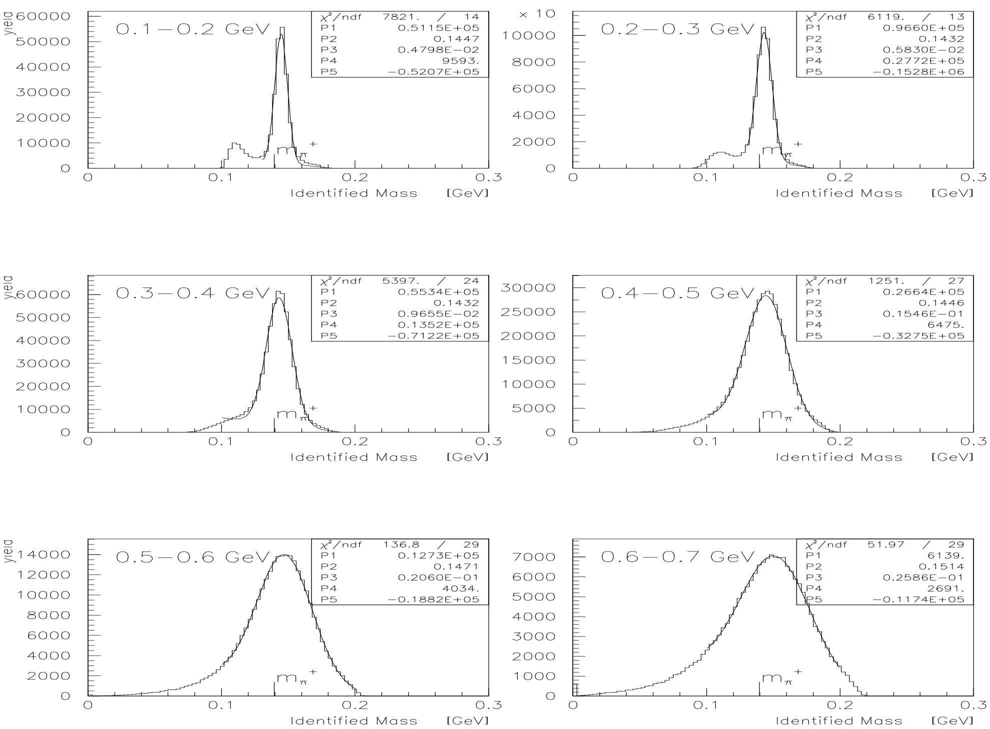

Figure 3.2: Mass distributions of identified pions for different particle momenta. Note the widening of the peak as the momentum increases. The distributions are fitted to a Gaussian $(P1 - P3)$ plus a linear function $(P4, P5)$.

3.5 Data filtering

As the reaction $\gamma p \to$K$^0\Sigma^+$ only comprises a small fraction of the total data set, a more manageable data set was created by filtering the g1c data. For the $\Sigma^+ \to p\pi^0$ decay channel the filtered set contains events which have three detected charged particles: a proton, π^+ and π^-. These particles were identified by their charge and reconstructed mass: for protons having a mass between 0.7 and 1.2 GeV (the mass of a proton being 0.938 GeV) and for pions having a mass between 0.0 and 0.4 GeV (the mass of a charged pion being 0.140 GeV). If the missing mass from these detected particles, MM($p\pi^+\pi^-X$), is between 0.02 and 0.3 GeV, thus within the range of the π^0 mass (0.135 GeV), then the events are written into the filtered file. For the $\Sigma^+ \to n\pi^+$ decay channel the filtered set contains events which have two detected π^+s and one detected π^- and a missing mass from these detected particles, MM($\pi^+\pi^+\pi^-X$), between 0.75 GeV and 1.15 GeV, thus in the range of the neutron mass (0.940 GeV). The shorthand for these events is $\Sigma^+ \to p\pi^0$ for the $\gamma p \to$K$^0\Sigma^+\to p\pi^+\pi^-\pi^0$ decay channel and $\Sigma^+ \to n\pi^+$ for the $\gamma p \to$K$^0\Sigma^+\to n\pi^+\pi^+\pi^-$ decay channel. This analysis is based on the data contained in these filtered files.

3.6 Vertex reconstruction and energy loss

Two procedures for vertex reconstruction are used in CLAS: VERT which reconstructs the vertex of any combination of two detected particles, and MVRT which determines a common vertex for all charged particles. The components of the reconstructed primary vertex from the MVRT bank are presented in Fig. 3.3. For this analysis the VERT package is used to reconstruct the kaon vertex from the detected π^+ and π^- resulting from the kaon decay. This information was used in studying the feasibility of employing an event selection based on the distance between the primary interaction point and the K^0_S decay vertex, discussed further in Section 4.2.4.

This analysis contains an energy loss correction for each detected particle by calculating the energy lost during the passage through the target and start counter, as the track reconstruction does not include these effects in calculating a particle's momentum. Figure 3.4 shows the relative difference between the particle's momentum after and before the energy correction, divided by the pre-energy loss momentum, which can be written as $\frac{p_{before}-p_{after}}{p_{before}}$. The two vertical bands correspond to the relative energy loss of protons and pions, respectively, as determined by this code based on Bethe-Bloch's formula.

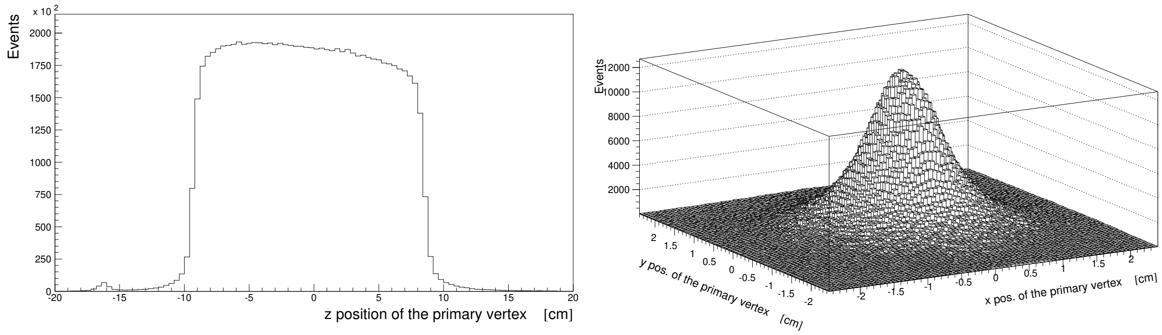

Figure 3.3: The z position and x versus y positions of the primary vertex reconstructed using MVRT

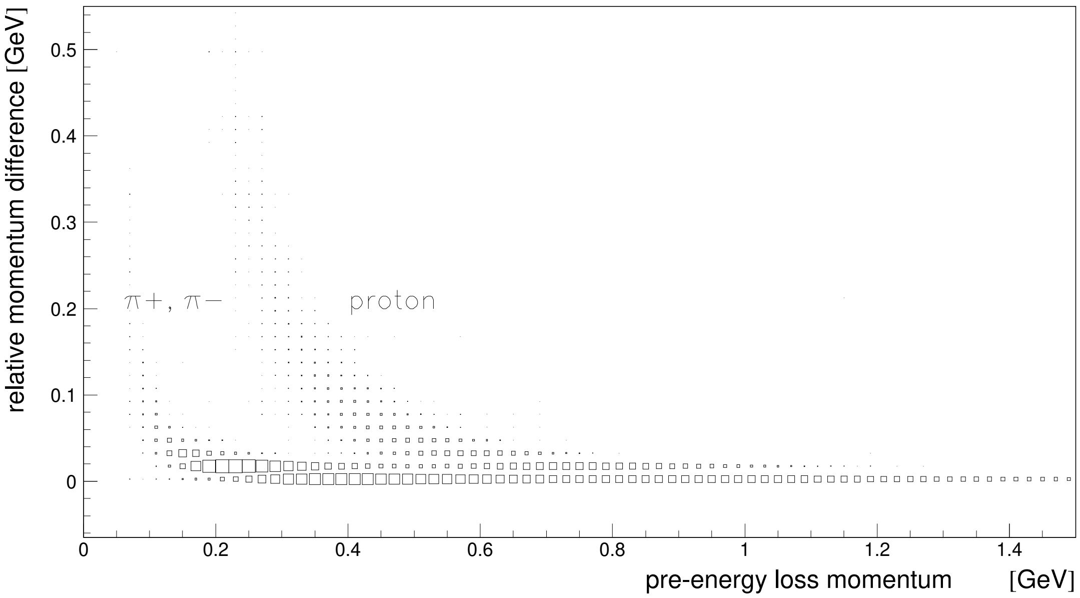

Figure 3.4: The fractional change in particle momentum due to energy loss. The band on the left is from charged pions, while the band on the right is from protons.

3.7 Photon flux

To determine the cross section, the incident flux of photons on the target must be known. The analysis of tagger counter hits gives the number of electrons incident on the tagger focal plane. To know the photon flux the "transmission efficiency" of bremsstrahlung photons through the collimator and onto the target must be known. Special normalization runs are taken at low intensity, with the total absorption counter (TAC) placed in the photon beam downstream of the target. For each of the 767 E-channels, the number of electrons is recorded, making sure that each of the corresponding photons satisfies the coincidence between hits in the focal plane of the tagger and the TAC.

3.7.1 Normalization procedure - gflux

The procedure used to determine the number of photons incident on the target is called gflux. This procedure first determines the number of photons per T-counter incident on the target, based on accidental hits in that T-counter. These results are then translated into the number of photons incident on the target corresponding to a given E-counter, using a conversion for the correspondence of T-counters to E-counters. This calculation is performed for every time interval between scaler events. Scaler events are special events containing scaler information of various detector components accumulated within 10-second time intervals. The photon flux on the target corresponding to a given T-counter (TC),$N_{\gamma TC}$, as determined by the gflux procedure is given by:

$$N_{\gamma TC} = R_{TC} \Delta T_{run} \epsilon_{TC} (1 + \nu) \ , \tag{3.1}$$

where R_{TC} is the rate in a given T-counter and ΔT_{run} is the rungated time for the considered interval between scaler events, corrected for livetime.

The parameter ν accounts for the photon loss due to absorption in material between the target and TAC; ν is determined to be 0.039 ± 0.002 [33].

The beam line efficiency, ϵ_{TC}, is determined by taking low intensity normalization runs with the TAC set up downstream to determine the number of tagged photons which reach the target. The number of triggers where the master-OR and TAC are in coincidence is compared with the number of triggers in the master-OR to give

$\epsilon_{TC} = (\frac{MOR*TAC}{MOR})_{TC}$.

The signals from each T-counter are inputted to a TDC. The start for the TDC is provided by a CLAS trigger; the stop by an electron striking the T-counter. The TDC is active for approximately 200 ns. Photons associated with the actual trigger provide a stop that occurs within the first 30 ns of the TDC window. Because of the relatively high counting rate, there is a reasonable chance that a TDC not stopped by the true event causing the trigger will be stopped after the first 30 ns by a photon not associated with the trigger. The rate of these out-of-time, or random, events is called R_{TC}. This quantity is used in Eq. 3.1 to determine the photon flux on the target corresponding to a given T-counter.

3.7.2 Gflux photon flux values for subsets of g1c data

The gflux procedure was used to obtain the photon flux in 50 MeV bins of photon energy. Figure 3.5 shows the photon energy spectra obtained for the different data sets. The 3.115 GeV running period had a number of runs in which the lower part of the photon energy range was not in use, as shown in the lower plot. Due to the erratic photon flux of the 3.115 GeV data set for lower photon energies and subsequent problems in the analysis, it was decided not to include data from this data set below 1.55 GeV photon energy in our analysis. In Fig. 3.5 there is a noticable drop in photon flux in the range 1.85 to 1.9 GeV for the 2.445 GeV data set. This drop in photon flux was identified as being due to a malfunctioning T-counter (T-counter 20), as discussed further in Section 4.1.2.

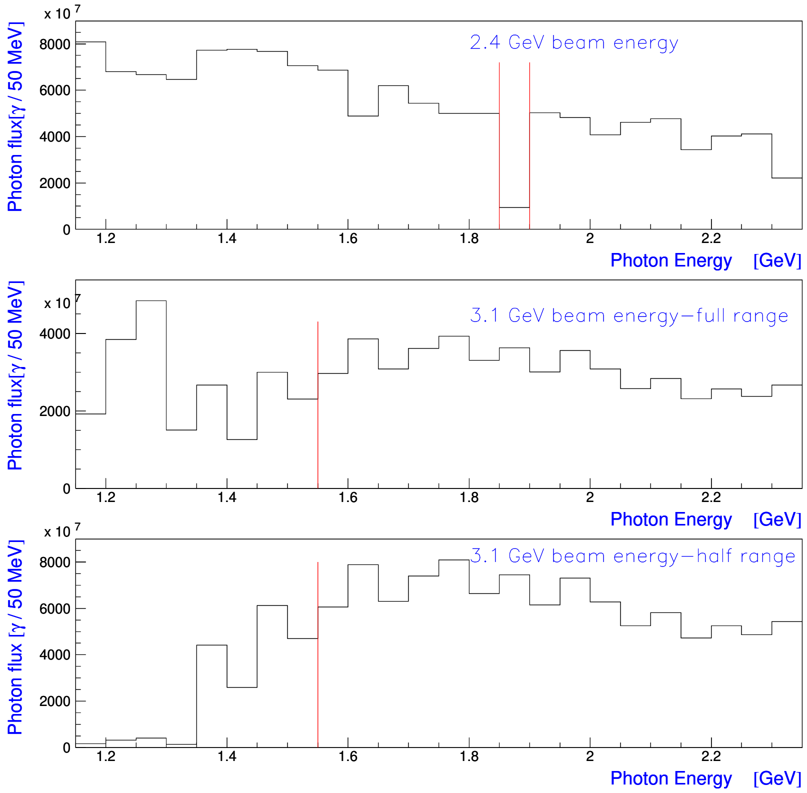

Figure 3.5: Photon flux values for different beam energies, for data from the $\Sigma^+ \to p\pi^0$ decay channel. The top plot shows results from 2.445 GeV data, the middle plot shows results from 3.115 GeV data with the entire tagger energy range in use, and the bottom plot shows results from 3.115 GeV data with the lower part of the tagger energy range not in use. Only the photon energy range used in the analysis is presented here. The vertical lines on the 2.445 GeV data set plot represent an area with low photon flux due to a malfunctioning T-counter. The vertical lines on the 3.115 GeV data sets separate the data used, above 1.55 GeV, from the rejected data below 1.55 GeV in photon energy.

Chapter 4

Data Analysis

The results from this analysis are presented as cross sections. Differential cross sections are determined for a given region in angle and energy by the equation

$$\frac{d\sigma}{d\Omega} = \frac{N}{(\Phi T \epsilon \Omega B)} \, , \tag{4.1}$$

where N is the number of detected events, Φ is the number of projectiles hitting the target (here the photon flux), T is the number of target protons per unit area, Ω is the solid angle under consideration, B is the product of branching ratios to the detected final-state particles and ϵ is the efficiency to detect events for this reaction. The procedures to determine the number of detected events, the photon flux, and the efficiency are presented in detail, followed by a discussion of cross section results and comparisons with previous experimental data and theoretical models.

In analyzing the reaction $\gamma p \rightarrow$K$^0\Sigma^+$ only cases where the kaon decays into a π^+ and π^- were considered. The kaon's decay into two π^0s would be very hard to reconstruct, since two γ s for each resultant π^0 would need to be detected and reconstructed correctly. Since the cross section is not forward peaked (as is presented later in the analysis), there is a low probability for four π^0 gamma rays to be detected in the forward EC. The absence of the $K^0_S \rightarrow \pi^0\pi^0$ channel in this analysis is taken into account in the calculations for the cross sections[1]. As mentioned earlier, only the decays of K^0_S particles are analyzed as the K^0_L particles are rarely detected within the system. This is also taken into account in calculations of cross sections. For the decay of the Σ^+, both decay channels, $\Sigma^+ \rightarrow p\pi^0$ and $\Sigma^+ \rightarrow n\pi^+$, were analyzed. This analysis is thus broken up into two decay channels. For each of these channels the detection of

[1]This decay channel requires the identification of three neutral particles: π^0 and π^0 from the K^0_S decay and either n or π^0 from the Σ^+ decay.

all three charged particles was required, while the neutral particle was reconstructed using missing mass. As mentioned earlier, data were filtered into a separate set for each decay. A diagram of the reactions considered is presented in Fig. 4.1.

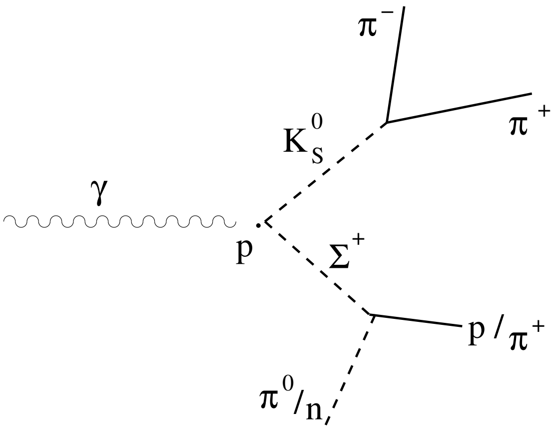

Figure 4.1: The reaction $\gamma p \to K^0\Sigma^+$ the solid lines show detected particles while dashed lines show particles that are not detected.

4.1 Removing irregular data

Through an initial analysis of the data to identify known quantities, information coming from data runs or detector elements that demonstrate erratic or unexplained behavior can be eliminated.

4.1.1 Identifying malfunctioning time-of-flight counters

Before the data were processed the timing of the time-of-flight scintillators was calibrated. Counters which were malfunctioning or had difficulties with the calibration were identified and removed from both the simulated and experimental data to improve the correlation between simulated results and the data sets. Figure 4.2 shows hits in time-of-flight paddles, by sector for the 2.445 GeV beam energy data set. For some malfunctioning paddles hits are not present or the efficiency is considerably smaller than for neighboring paddles. The 3.115 GeV beam energy data set has similar results, with some of the same malfunctioning paddles as in the 2.445 GeV set showing many fewer hits.

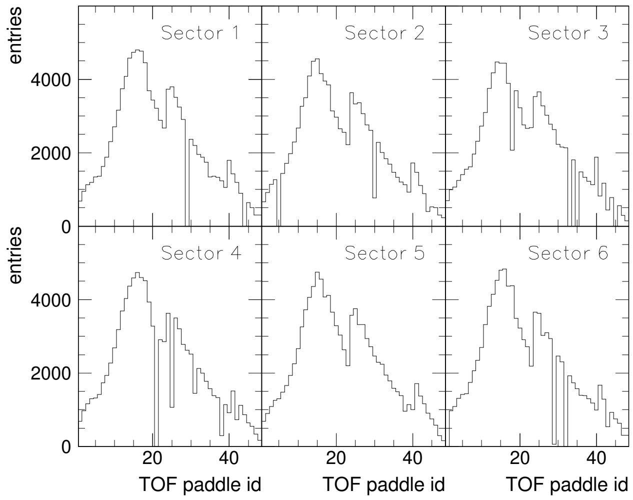

Figure 4.2: Hits in time-of-flight paddles, by sector for the 2.445 GeV beam energy data set, showing dips due to malfunctioning paddles.

4.1.2 Exclusion of runs and E-counters based on normalized particle yield information

To analyze the quality of the photon flux obtained by the gflux procedure, a normalized particle yield for each run was obtained, using proton yields for the $\Sigma^+ \rightarrow p\pi^0$ decay channel and π^+ yields for the $\Sigma^+ \rightarrow n\pi^+$ decay channel. The run numbers are consecutive from the beginning of data taking with CLAS, so the run numbers for these data sets increase in value with time. The normalized proton or π^+ yield is calculated for a given run and range of E-channels by dividing the number of protons or π^+s detected in that region by the photon flux that was obtained from gflux. For stable running periods, both the photon flux and normalized proton/π^+ yield should be constant. If there is a large particle yield but a comparatively low photon flux, then a problem occured in the photon flux calculation for that run or E-channel region. If both the particle yield and photon flux are very low in a given region, then that could indicate other problems with the equipment. By analyzing this information, various runs and E-channels were identified which were unreliable. A total of eight of these runs from the 2.445 GeV beam energy data set, but no runs from the 3.115 GeV data set, were removed. One set of E-channels that was removed based on this procedure was numbers

185-200 (which correspond to T-counter number 20) where there were unusually low particle yields and photon flux values. Removing these E-channels from the 2.445 GeV data set leaves a gap in the photon energy range covered by this analysis from 1.864 to 1.902 GeV. As the correspondence of E-channels and photon energy changes with beam energy, for the 3.115 GeV data set these counters are out of the photon energy range in which data are analyzed. Instabilities were also found in E-channels 510-520, corresponding to photon energies of 1.408 to 1.442 GeV for the 3.115 GeV beam energy data set. This energy range was already removed from the analysis due to the fluctuating photon flux in that area. For the 2.445 beam energy data set, the energy range corresponding to these E-channels is not within the range of photon energies of this analysis, thus does not affect the data.

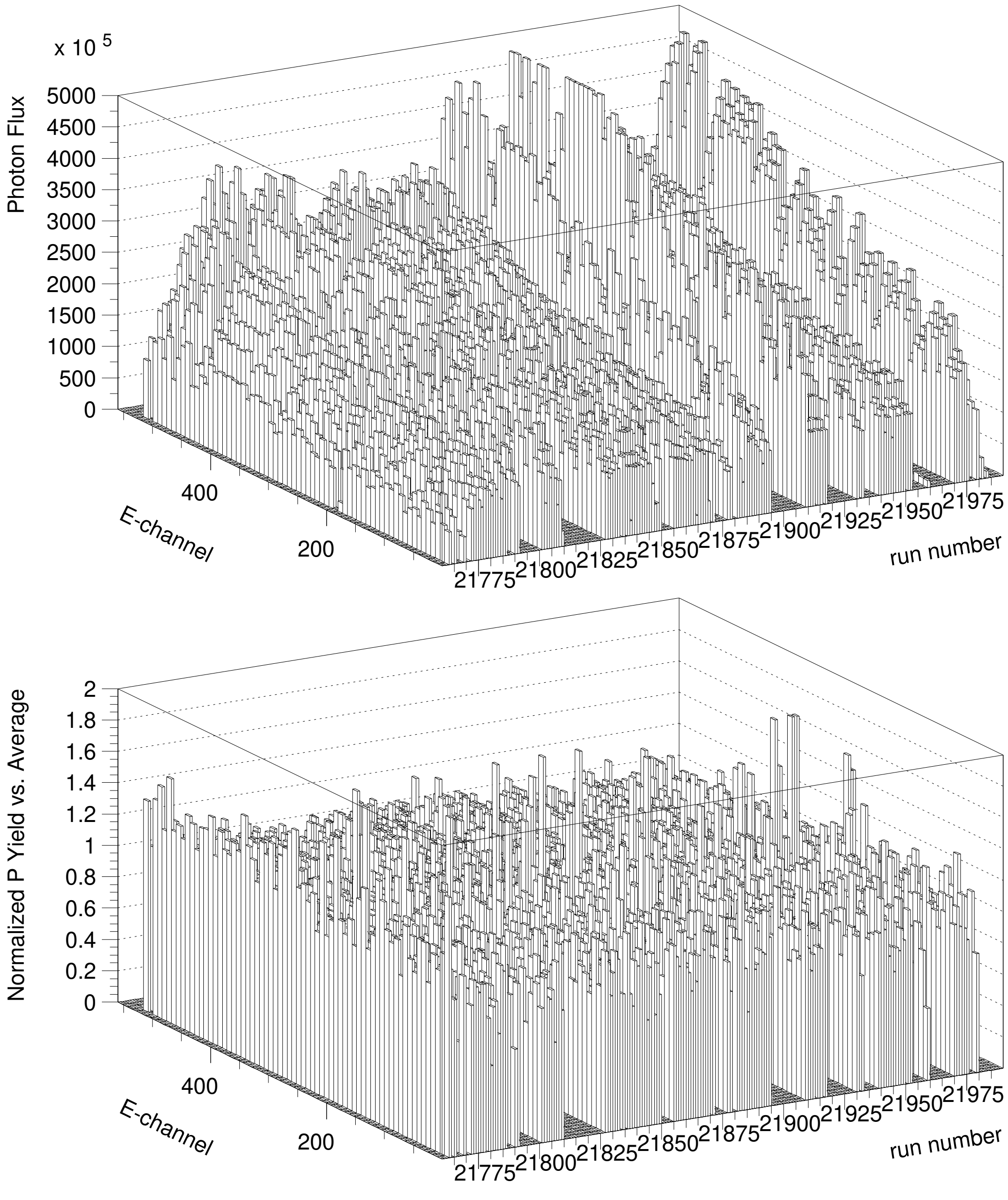

Figure 4.3: Photon flux and normalized proton yield divided by averaged normalized proton yield for 2.445 GeV data. The top plot shows the photon flux by run number and groups of 8 E-channels. The bottom plot shows the corresponding normalized proton yield (the number of protons divided by the photon flux) divided by the average normalized proton yield.

4.2 Selection of events

To obtain the final event sample, the identified events containing three charged particles must be processed through an event selection as described in Chapter 3. As these particles were initially identified with broad cuts on the mass, a more accurate identification is performed through a beta-momentum event selection. Events satisfying the reaction studied, $\gamma p \rightarrow K^0\Sigma^+$, only account for a small fraction of these three-charged-particle events due to higher production rates of other reactions with the same final state particles in the data sample. To create a final event sample with events only from $\gamma p \rightarrow K^0\Sigma^+$, event selections are made which satisfy unique relations between momenta and energies defined for the decay particles from this reaction. These event selections depend upon missing mass and invariant mass techniques involving the three detected particles. As these relations can also be accidentally satisfied by other reactions, a sideband background subtraction is performed to eliminate background events which would otherwise be included in the final event sample. Figure 4.4 shows the steps taken in event selection to obtain the final event sample, which are described in the following sections.

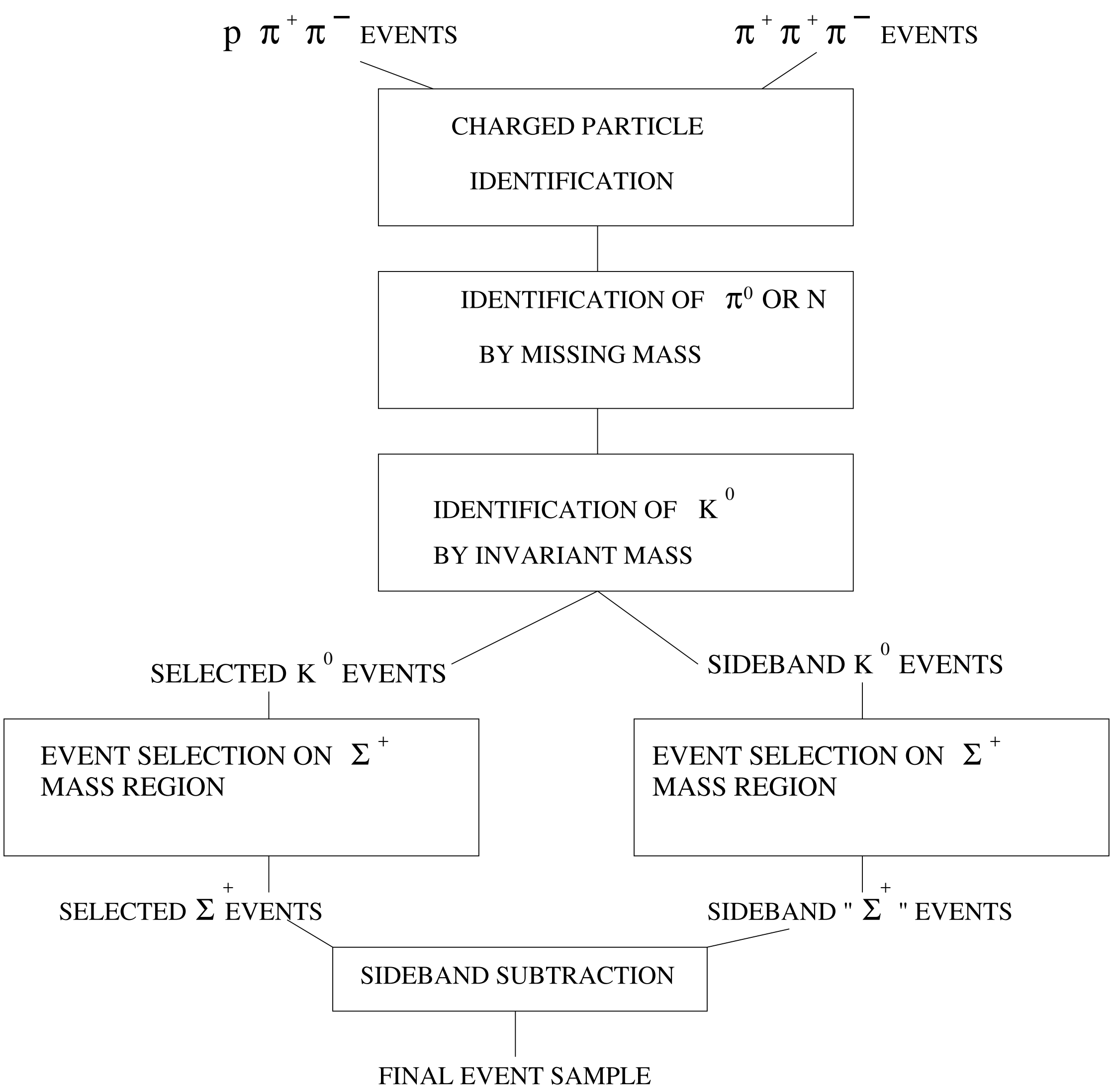

Figure 4.4: Steps in event selection to obtain the final event sample as described in Section 4.2.

4.2.1 Charged particle identification

For the analysis of both decay channels, $\gamma p \to \mathrm{K}^0\Sigma^+ \to (\pi^+\pi^-)(\mathrm{p}\,\pi^0)$ and $\gamma p \to K^0\Sigma^+ \to (\pi^+\pi^-)(\mathrm{n}\ \pi^0)$, the particles p, π^+, and π^- are identified using broad mass cuts. As described in Section 3.4, the mass resolution for a detected particle depends on the quality of its reconstructed momentum and velocity. The mass peaks for high velocity particles are therefore expected to be broader. Instead of selecting a particle based on its mass peak, a two-dimensional histogram of the velocity β of the particle versus its momentum (p) was considered. Figure 4.5 shows a plot of β vs. p for charged particles, with lines drawn to show the regions of selected events. Using the relation $\beta = \frac{p}{E} = \frac{p}{\sqrt{m^2+p^2}}$ and substituting in the mass ranges 0.11 to 0.16 GeV for pions (where the mass of a π^+ is 0.140 GeV) and 0.91 to 1.05 GeV for protons (where the mass of a proton is 0.938 GeV), and adding or subtracting a shift, upper and lower bounds on an acceptable β for the detected particle can be set as:

$$\frac{p}{\sqrt{0.16^2+p^2}} - 0.2 < \beta < \frac{p}{\sqrt{0.11^2+p^2}} + 0.2$$

for pions and

$$\frac{p}{\sqrt{1.05^2+p^2}} - 0.0 < \beta < \frac{p}{\sqrt{0.91^2+p^2}} + 0.2$$

for protons, where p is measured in units of GeV. Figure 4.5 shows that most of the events fall within these limits, represented by curves on the plot.

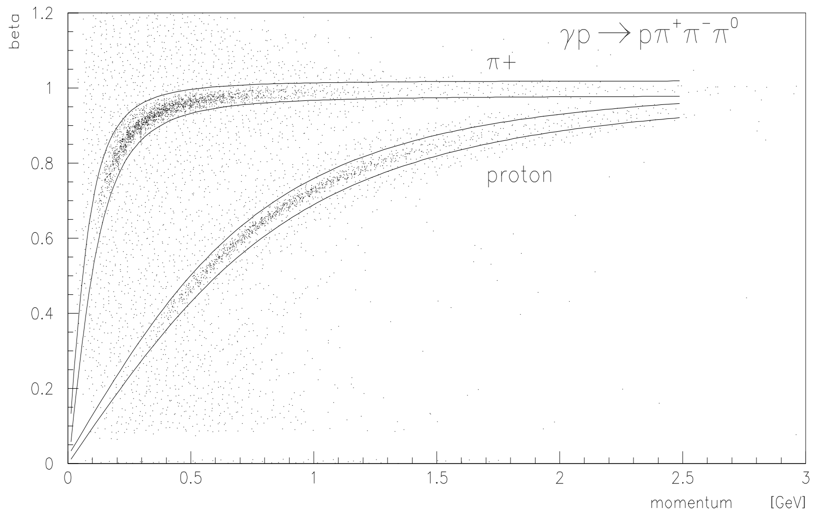

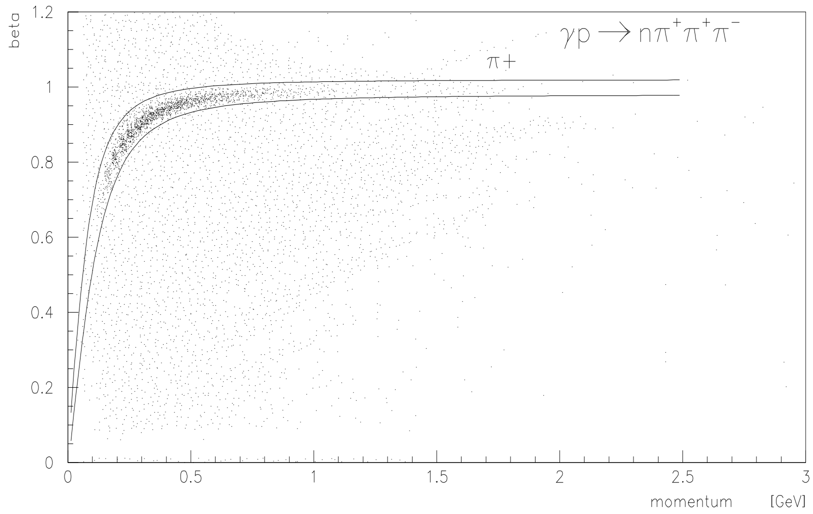

Figure 4.5: β versus momentum for identified, positively charged particles. Events from the $\Sigma^+ \to p\pi^0$ decay channel are on top and from the $\Sigma^+ \to n\pi^+$ decay channel are on the bottom, along with curves representing the event selection for the proton and charged pions. The π^- distribution (not plotted here) looks similar to that of the π^+.

4.2.2 The $\gamma p \to K^0\Sigma^+ \to p\pi^+\pi^-\pi^0$ decay channel

4.2.2.1 Identification of π^0 by missing mass

For the reaction $\gamma p \to K^0\Sigma^+ \to (\pi^+\pi^-)(p\pi^0)$ the following detected particles are required: one proton, one π^+ and one π^-. The undetected π^0 is then reconstructed using missing mass.

Since energy and momentum of the incoming photon(γ), the target proton(t) and the three detected particles(p, π^+ and π^-) are known, the mass of the undetected particle X can be determined using conservation of energy and momentum by writing

$$M_X^2 = (E_\gamma + E_t - E_p - E_{\pi^+} - E_{\pi^-})^2 - (\vec{p_\gamma} + \vec{p_t} - \vec{p_p} - \vec{p_{\pi^+}} - \vec{p_{\pi^-}})^2 \, , \tag{4.2}$$

where E_i is the energy of a particle and $\vec{p_i}$ is the three-momentum of that particle. The shorthand for this missing mass from a detected p, π^+ and π^- is $\mathrm{MM}(p\pi^+\pi^-X)$.

In the laboratory frame where $\vec{p_t} = 0$, this becomes (where t refers to the target proton)

$$M_X^2 = (E_\gamma + m_t - E_p - E_{\pi^+} - E_{\pi^-})^2 - (\vec{p_\gamma} - \vec{p_t} - \vec{p_{\pi^+}} - \vec{p_{\pi^-}})^2 \, . \tag{4.3}$$

Figure 4.6 shows the experimental data for $\mathrm{MM}(p\pi^+\pi^-X)$ for six photon energy bins. A distinct peak at the mass of the π^0 (0.135 GeV) is present in each spectrum. Only those events where this missing mass is determined to be between 0.07 and 0.20 GeV are used in the subsequent analysis. This has the advantage of eliminating events which have a detected p, π^+ and π^- but no π^0, such as those that come from the prominent reaction $\gamma p \to \rho^0 p \to \pi^+\pi^- p$ or $\gamma p \to \Delta^{++}\,\pi^- \to p\,\pi^+\pi^-$.

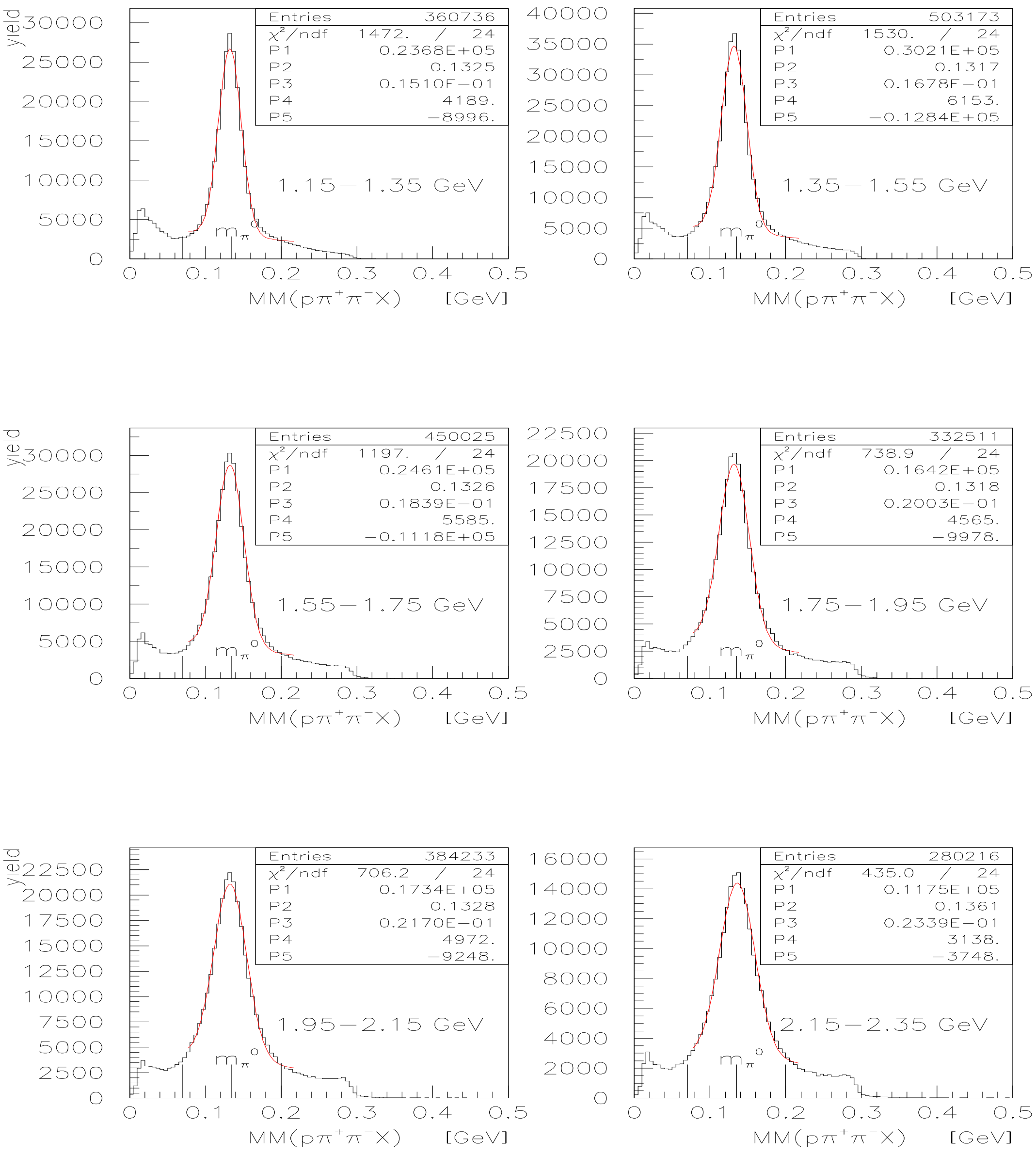

Figure 4.6: MM($p\pi^+\pi^-X$) for six photon energy bins. The plots are obtained from the filtered data set. Therefore the significant larger peak at MM($p\pi^+\pi^-X$)= 0 and the distribution above 0.3 GeV is suppressed. The vertical lines at MM($p\pi^+\pi^-X$) = 0.07 and 0.20 GeV represent the data selection limits used in the analysis. This peak is fit to a Gaussian ($P1 - P3$) and a linear function ($P4, P5$) with the fit results displayed on the plot. The poor value of χ^2/ndf shows that a Gaussian is a poor approximation to the data, but only the location of the selection limits effects subsequent analysis.

4.2.2.2 Identification of K_S^0 and Σ^+

The next step in event selection is to examine a plot of the invariant mass squared, $M^2(\pi^+\pi^-)$, versus the missing mass squared, $MM^2(\pi^+\pi^-X)$, for the detected π^+ and π^- as shown in Fig. 4.7.

The notation M($\pi^+\pi^-$) refers to the invariant mass of the detected π^+ and π^-. If these particles decayed from a K_S^0, their combined system will have the momentum and energy of the K_S^0, corrected for the mass difference of K_S^0 and two pions. The invariant mass squared of these particles is given by the equation: $M^2(\pi^+\pi^-) = (E_{\pi^+} + E_{\pi^-})^2 - (\vec{p_{\pi^+}} + \vec{p_{\pi^-}})^2$, where E_i is the energy of a particle and $\vec{p_i}$ is the three-momentum of that particle. The invariant mass of the detected π^+ and π^- for particles decaying from a K_S^0 should be centered around the mass of the K_S^0: 0.498 GeV.

MM($\pi^+\pi^-X$) refers to the missing mass with respect to the known incoming particles and detected final state particles π^+ and π^-. This can be written as:

$$MM^2(\pi^+\pi^-X) = (E_\gamma + E_t - E_{\pi^+} - E_{\pi^-})^2 - (\vec{p_\gamma} + \vec{p_t} - \vec{p_{\pi^+}} - \vec{p_{\pi^-}})^2 \ . \tag{4.4}$$

As the reaction being considered is $\gamma p \rightarrow K^0\Sigma^+$ the missing mass from the detected π^+ and π^- which came from the decay of the K_S^0 should be centered around the mass of the Σ^+ (1.189 GeV).

There is a distinct peak in Fig. 4.7 on the $MM^2(\pi^+\pi^-X)$ axis for the Σ^+ mass squared (1.414 GeV^2), and on the $M^2(\pi^+\pi^-)$ axis for the K_S^0 mass squared (0.248 GeV^2). It is clear that the events being sought are in this peak, along with unwanted background events. Before making any further event selections, a broad cut on $MM^2(\pi^+\pi^-X)$ is placed in the range of 1.38 GeV^2 to 1.44 GeV^2, to select only these events in the region of interest.

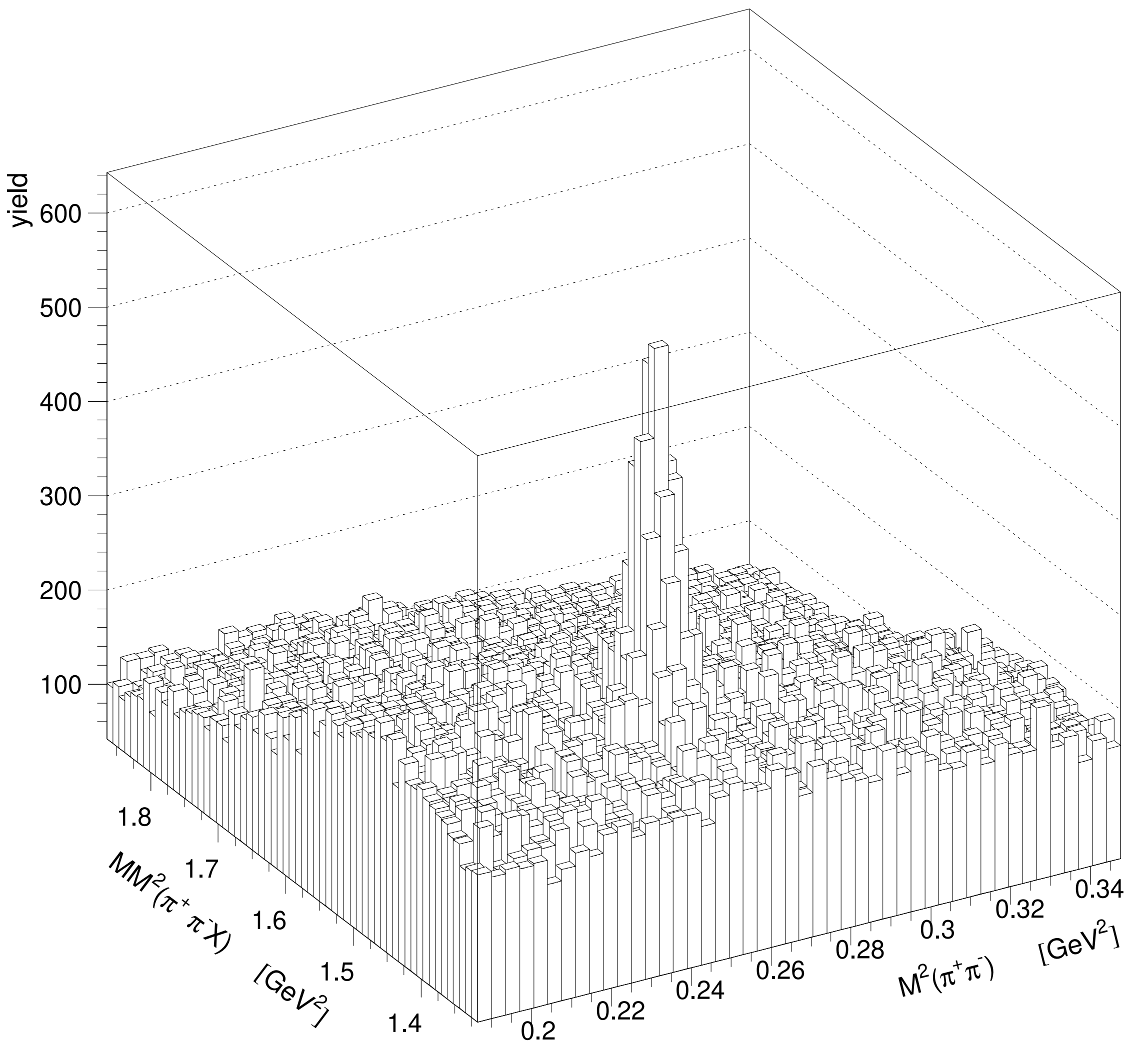

Figure 4.7: $M^2(\pi^+\pi^-)$ versus $MM^2(\pi^+\pi^-X)$ for the $\Sigma^+ \to p\pi^0$ decay channel. The distinct peak is located at the intersection of the mass squared of the K_S^0 (0.248 GeV^2) on the $M^2(\pi^+\pi^-)$ axis and the mass squared of the Σ^+ (1.414 GeV^2) on the $MM^2(\pi^+\pi^-X)$ axis. This peak contains the physics events sought.

Next events are selected based on the invariant mass of the detected π^+ and π^-. The mass of the events being sought will peak around the mass of the K^0_S (0.498 GeV). Figure 4.8 shows, for each of six photon energy bins, a peak at the mass of the K^0_S above a relatively flat background. This background must ultimately be subtracted from the events in the peak. To determine the properties of the K^0_S peak, the peak is fit to a Gaussian and the background is fit to a third order polynomial, as shown in this figure. Table 4.1 lists the means and standard deviations (σ) for each photon energy bin from the Gaussian fits to M($\pi^+\pi^-$).

Table 4.1: Results of Gaussian and third order polynomial fit to M($\pi^+\pi^-$)

E_γ (GeV)	mean of Gaussian	σ of Gaussian
$\Sigma^+ \to p\pi^0$	(GeV)	(GeV)
1.15-1.35	0.4935 ± 0.0005	0.0048 ± 0.0005
1.35-1.55	0.4948 ± 0.0002	0.0041 ± 0.0002
1.55-1.75	0.4954 ± 0.0003	0.0043 ± 0.0003
1.75-1.95	0.4951 ± 0.0003	0.0028 ± 0.0003
1.95-2.15	0.4961 ± 0.0004	0.0042 ± 0.0004
2.15-2.35	0.4970 ± 0.0005	0.0042 ± 0.0007
$\Sigma^+ \to n\pi^+$		
1.15-1.35	0.4941 ± 0.0004	0.0046 ± 0.0004
1.35-1.55	0.4950 ± 0.0002	0.0044 ± 0.0003
1.55-1.75	0.4953 ± 0.0003	0.0042 ± 0.0003
1.75-1.95	0.4961 ± 0.0004	0.0044 ± 0.0004
1.95-2.15	0.4959 ± 0.0005	0.0044 ± 0.0006
2.15-2.35	0.4963 ± 0.0008	0.0059 ± 0.0008

Based on the results for the mean (0.49545 GeV) and 1 σ width for the standard deviation (0.0135 GeV) for the Gaussian fit, the peak region is defined to include the mean $\pm$ 3σ, 0.49545 $\pm$ 0.0135 GeV. The events within this range are referred to as "selected" events.

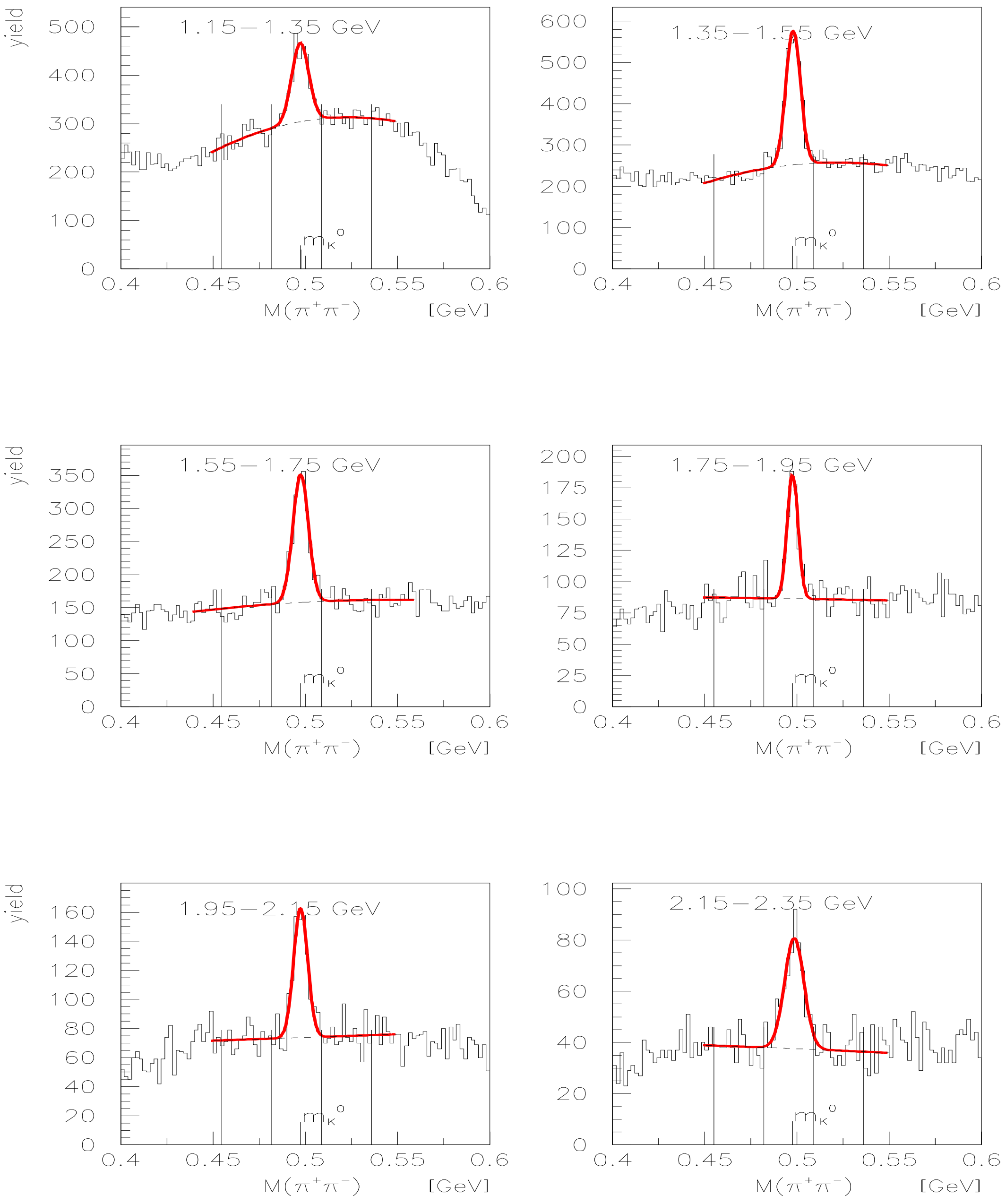

Figure 4.8: M($\pi^+\pi^-$) for six photon energy bins for the $\Sigma^+ \to p\pi^0$ decay channel showing a peak at $m_{K_S^0}$ over a flat background (except for 1.15-1.35 GeV, where the phase space for $\pi^+\pi^-$ in $p\pi^+\pi^-\pi^0$ is limited to about 0.6 - 0.65 GeV). The bold lines show a fit to a Gaussian and a third order polynomial to the background. The vertical lines represent the limits on the event selection, in the center region, and sideband subtraction, in the outer two regions.

4.2.2.3 Final event selection by sideband subtraction

In the plot of M($\pi^+\pi^-$) in Fig. 4.8, there are background events located under the peak of selected events. These background events in the selected event range must be subtracted from those selected events to give the total number of events in the final event sample, which then are used to calculate cross sections. Since these background events are smoothly distributed over a large mass range, a technique called "sideband background subtraction" can be performed. Mass ranges, called "sidebands", to the right and left of the selected event range are determined. Figure 4.8 presents the regions used for selected events and for sidebands. As the selected events range is 0.49545 ± 0.0135 GeV, a sideband event range is chosen to be regions that are 0.027 GeV wide on both sides of the selected event range. These sideband events are processed through the next analysis step along with the selected events, and a subtraction is performed afterwards. Since the two sidebands together cover twice the mass range of the peak region, the sideband events are divided by two before subtracting them. As these sideband events will have similar kinematics as the background events under the K_S^0 peak, subtracting them from the selected events will result in approximately the correct number of events used to calculate cross sections.

In this analysis step, the missing mass of the detected π^+ and π^-, MM($\pi^+\pi^-X$), is calculated for both sets of events, selected and sideband. For the decay channel $\gamma p \rightarrow \mathrm{K}^0\Sigma^+ \rightarrow p\pi^+\pi^-\pi^0$, many of the selected events should be located in a peak centered around the mass of the Σ^+. It is expected that the sideband events will approximate the background to this peak. No other reaction channel has a resonant state in M($\pi^+\pi^-$) around 0.498 GeV, the mass of the K_S^0, and a resonant state in MM($\pi^+\pi^-X$) around 1.189 GeV, the mass of the Σ^+. In the plots shown in Fig. 4.9, the total number of selected events per bin is represented by a solid histogram while the sideband events are represented by data points with error bars. Clearly, the sideband events do not peak at the Σ^+ mass. When they are subtracted from the selected events, there will remain a distinct peak centered around the mass of the Σ^+. The shape of the sideband agrees with what is found in simulated data, as is discussed in Section 4.3.2.5. The final event sample for each energy and angular bin is determined by subtracting the number of sideband events from the number of selected events and then summing the center seven bins on this plot, in the mass range from 1.170 to 1.205 GeV. This result is used to calculate cross sections. The analysis sums events over seven bins centered around the mass of the Σ^+, since the Σ^+ events appear to fall mostly within this range. Analyses conducted with other selection criteria are discussed in section 4.4.2.

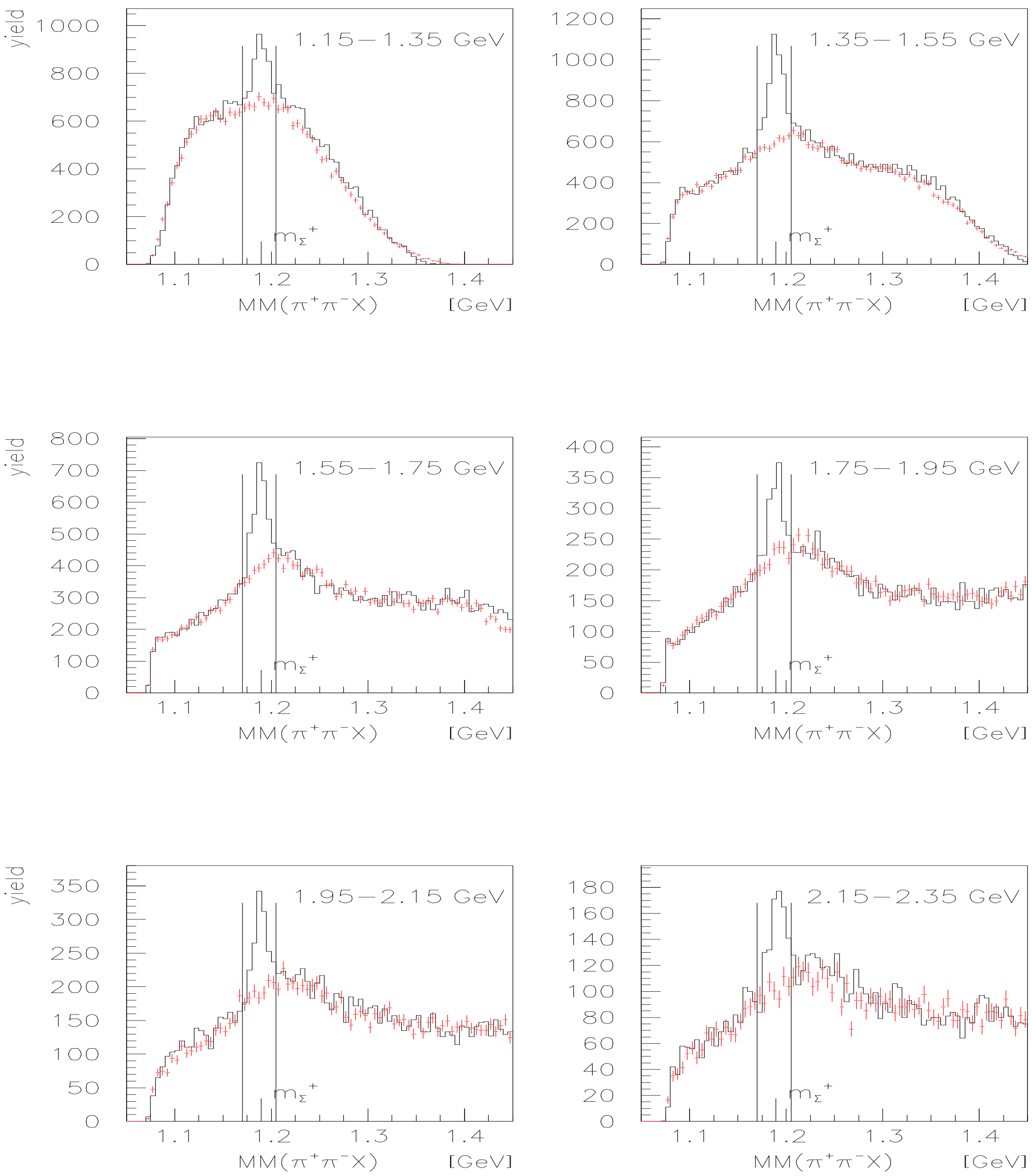

Figure 4.9: MM($\pi^+\pi^- X$) for the $\Sigma^+ \to p\pi^0$ decay channel showing selected events and sideband events. The solid line shows the total of selected events, while data points with error bars show the sideband events. The vertical lines define the region of the event selection from 1.170 to 1.205 GeV, centered around the mass of the Σ^+. The final event sample is determined by subtracting the sideband events from the selected events and summing the results in this region.

4.2.3 The $\gamma p \rightarrow$K$^0\Sigma^+\rightarrow n\pi^+\pi^+\pi^-$ decay channel

4.2.3.1 Identification of a neutron by missing mass

For the reaction $\gamma p \rightarrow$K$^0\Sigma^+\rightarrow (\pi^+\pi^-)(n\pi^+)$, two π^+s and one π^- are required . The undetected n is then reconstructed using missing mass techniques. This missing mass is found from the equation

$$M_X^2 = (E_\gamma + E_t - E_{\pi^+} - E_{\pi^+} - E_{\pi^-})^2 - (\vec{p_\gamma} + \vec{p_t} - \vec{p_\pi^+} - \vec{p_{\pi^+}} - \vec{p_{\pi^-}})^2 \ . \qquad (4.5)$$

(where t refers to the target proton) which is similar to equation 4.2.

Figure 4.10 shows the experimental data for MM($\pi^+\pi^+\pi^- X$) for six photon energy bins. A distinct peak at the mass of the neutron (0.938 GeV) is present in each spectrum. Only events where this missing mass is between 0.85 and 1.05 GeV are used in the subsequent analysis.

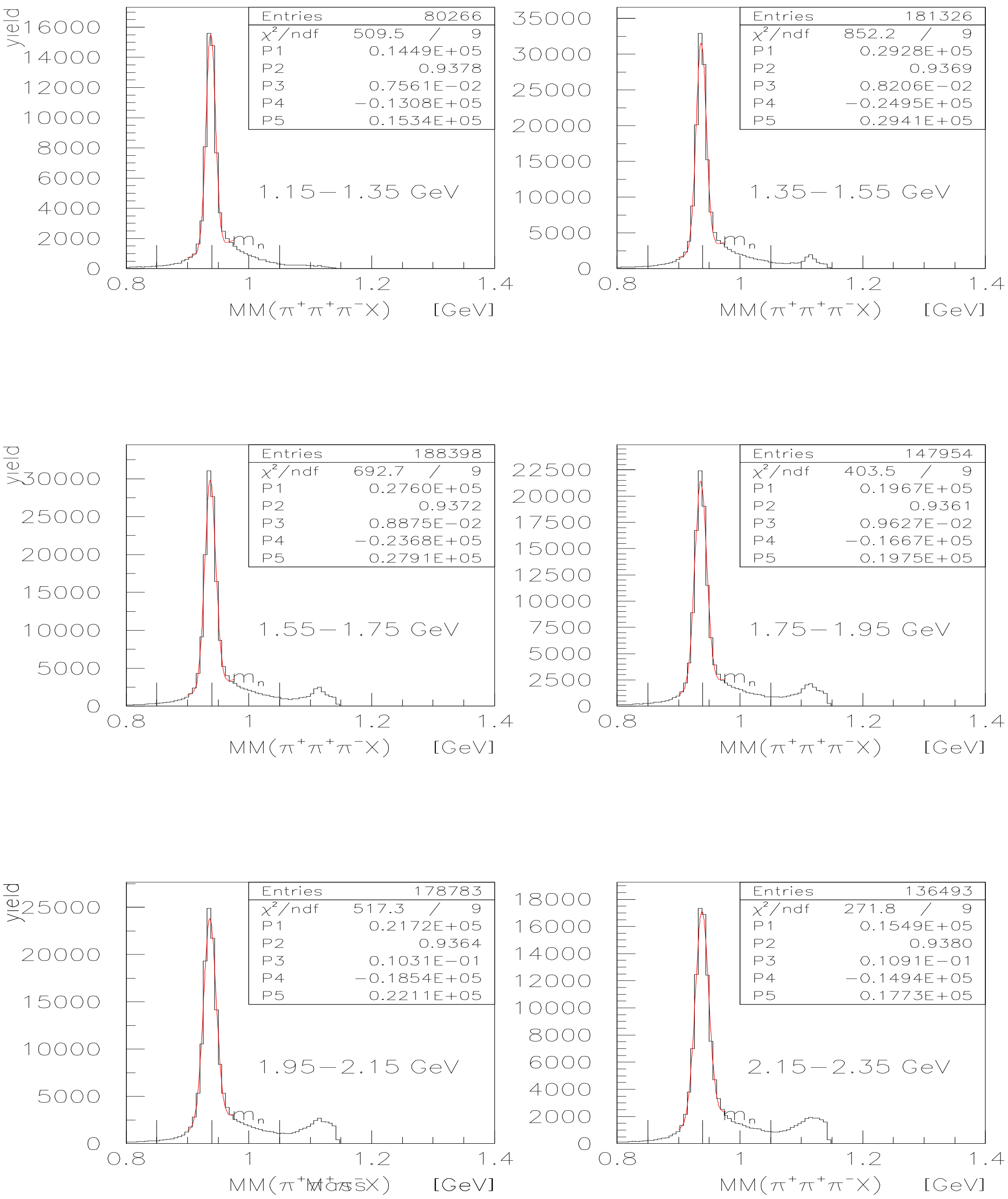

Figure 4.10: $\mathrm{MM}(\pi^+\pi^+\pi^-X)$ for the $\Sigma^+ \to n\pi^+$ decay channel. The vertical lines at $\mathrm{MM}(\pi^+\pi^+\pi^-X) = 0.85$ and 1.05 GeV represent the data selection limits used in the analysis. This peak is fit to a Gaussian ($P1 - P3$) and a linear function ($P4, P5$) with the fit results displayed on the plot.

4.2.3.2 Identification of K_S^0 and Σ^+

Since there are two detected π^+ particles detected, it must be determined which π^+ came from the decay of the $K_S^0 \to \pi^+\pi^-$ and which came from the decay of the $\Sigma^+ \to n$ π^+. The invariant masses of each π^+ combined with the π^- are compared, and the π^+ present in the combination with an invariant mass closest to that of a K_S^0, is assigned as coming from the K_S^0 decay.

The next step in event selection is to examine a plot of the invariant mass squared, $M^2(\pi^+\pi^-)$ versus the missing mass squared, $MM^2(\pi^+\pi^-X)$ of the detected π^+ and π^- as shown in Fig. 4.11. The missing mass squared from the detected π^+ and π^- which came from the decay of the K_S^0 should be centered around the mass squared of the Σ^+ (1.414 GeV^2).

There is a distinct peak in Fig. 4.11 on the $MM^2(\pi^+\pi^-X)$ axis at the Σ^+ mass squared (1.414 GeV^2), and on the $M^2(\pi^+\pi^-)$ axis at the K_S^0 mass squared (0.248 GeV^2). Before making any further event selections, a broad cut is placed on the $MM^2(\pi^+\pi^-X)$ in the range of 1.175 GeV to 1.20 GeV, to select only these events in the region of interest.

The analysis now selects events based on the invariant mass of the detected π^+ and π^-. The events being sought should be peaked around the mass of the K_S^0 (0.498 GeV). Figure 4.12 shows for each of six photon energy bins a peak at the mass of the K_S^0 over a relatively flat background. Based on the results of a Gaussian fit to these peaks (as presented in Table 4.1), the peak region is defined to include the mean $\pm$ 3σ, 0.49545 $\pm$ 0.0135 GeV. These are the selected events used in the sideband subtraction.

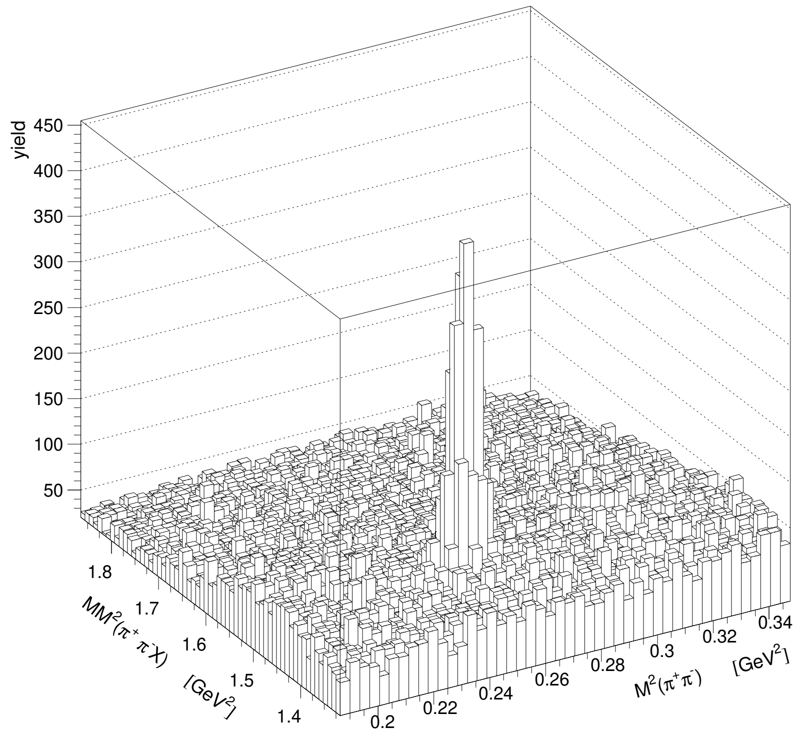

Figure 4.11: $M^2(\pi^+\pi^-)$ versus $MM^2(\pi^+\pi^-X)$ for the $\Sigma^+ \to n\pi^+$ decay channel. A distinct peak is located at the intersection of the mass squared of the K^0_S (0.248 GeV^2) on the $M^2(\pi^+\pi^-)$ axis and the mass squared of the Σ^+ (1.414 GeV^2) on the $MM^2(\pi^+\pi^-X)$ axis. This peak contains the physics events sought.

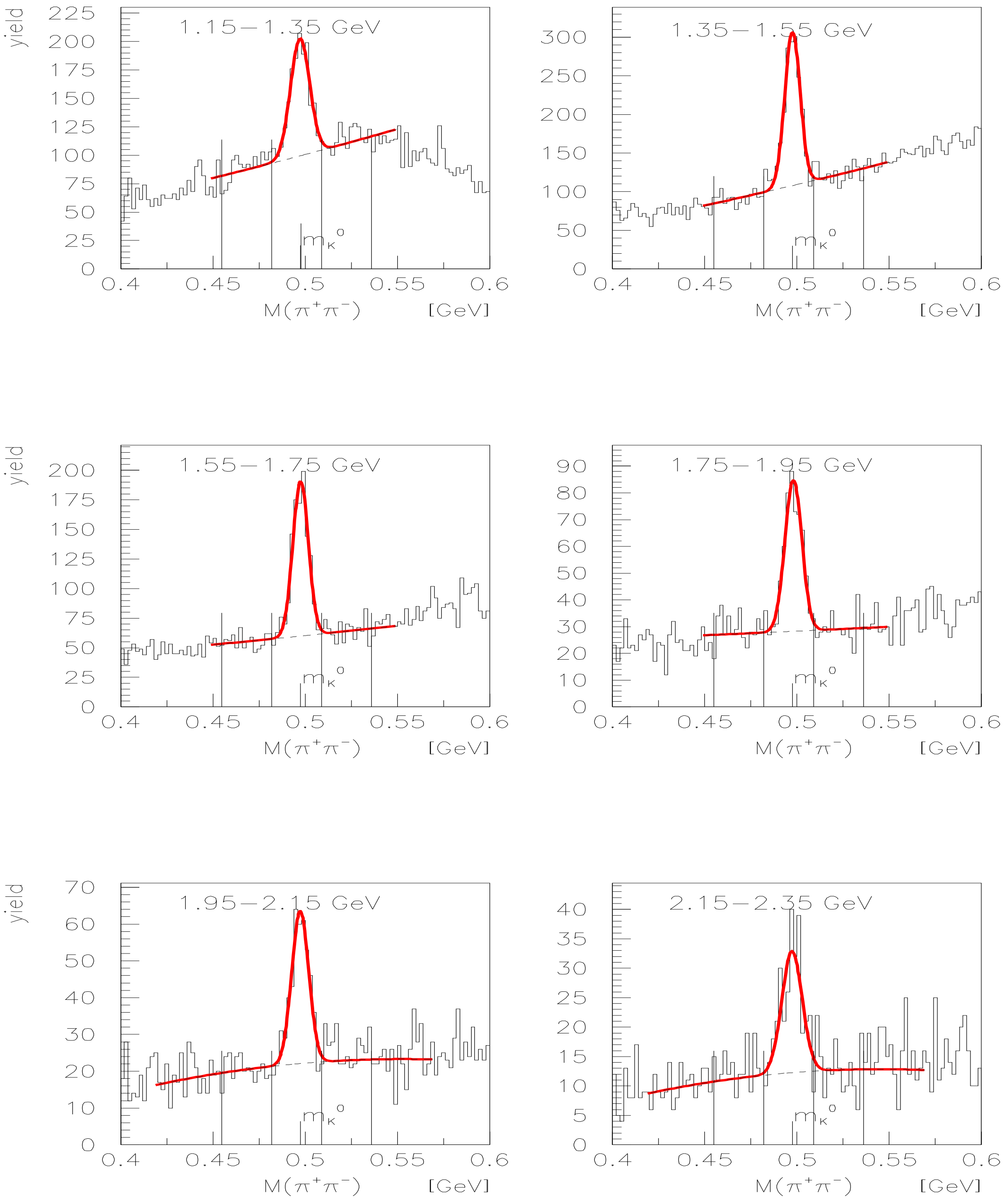

Figure 4.12: M($\pi^+\pi^-$) for the $\Sigma^+ \to n\pi^+$ decay channel. The bold line shows a fit to a Gaussian and a third order polynomial fit to the background. The vertical lines represent the limits on the event selection, in the center region, and sideband subtraction, in the outer two regions.

4.2.3.3 Final event selection by sideband subtraction

As described in Section 4.2.2.3, a sideband subtraction is performed on these events.

Figure 4.12 presents the regions used for selected events and for sidebands. As the range for selected events is 0.49545 $\pm$ 0.0135 GeV, sideband event regions are chosen to be 0.027 GeV wide on both sides of the selected event range. These sideband events are processed through the next analysis step along with the selected events, and a subtraction is performed afterwards. Since the two sidebands together cover twice the mass range of the peak region, the sideband events are divided by two before subtracting them. As these sideband events will have similar kinematics as the background events under the K^0_S peak, subtracting them from the selected events will result in approximately the correct number of events which can be used to calculate cross sections.

In this analysis step, the missing mass of the detected π^+ and π^-, MM($\pi^+\pi^-X$), is calculated for both sets of events, selected and sideband. For the decay channel $\gamma p \rightarrow \mathrm{K}^0\Sigma^+ \rightarrow n\pi^+\pi^+\pi^-$, the selected events should be located in a peak centered around the mass of the Σ^+. It is expected that the sideband events will approximate a background to this peak. No other reaction channel has a resonant state in M($\pi^+\pi^-$) around 0.498 GeV, the mass of the K^0_S, and a resonant state in MM($\pi^+\pi^-X$) around 1.189 GeV, the mass of the Σ^+. In the plots shown in Fig. 4.13, the total number of selected events per bin is represented by a solid histogram while the sideband events are represented by data points with error bars. Clearly, the sideband events do not peak at the Σ^+ mass. When they are subtracted from the selected events, a distinct peak remains centered around the mass of the Σ^+. The shape of the sideband agrees with what is found in simulated data, as will be discussed in Section 4.3.2.5. The final event sample for each energy and angular bin is determined by subtracting the number of sideband events from the number of selected events and then summing the center seven bins on this plot in the mass range from 1.170 to 1.205 GeV. This result is used to calculate cross sections for a given energy and angle. The analysis only sums events over seven bins centered around the mass of the Σ^+, as the background-subtracted peaks appear to fall mostly within this range.

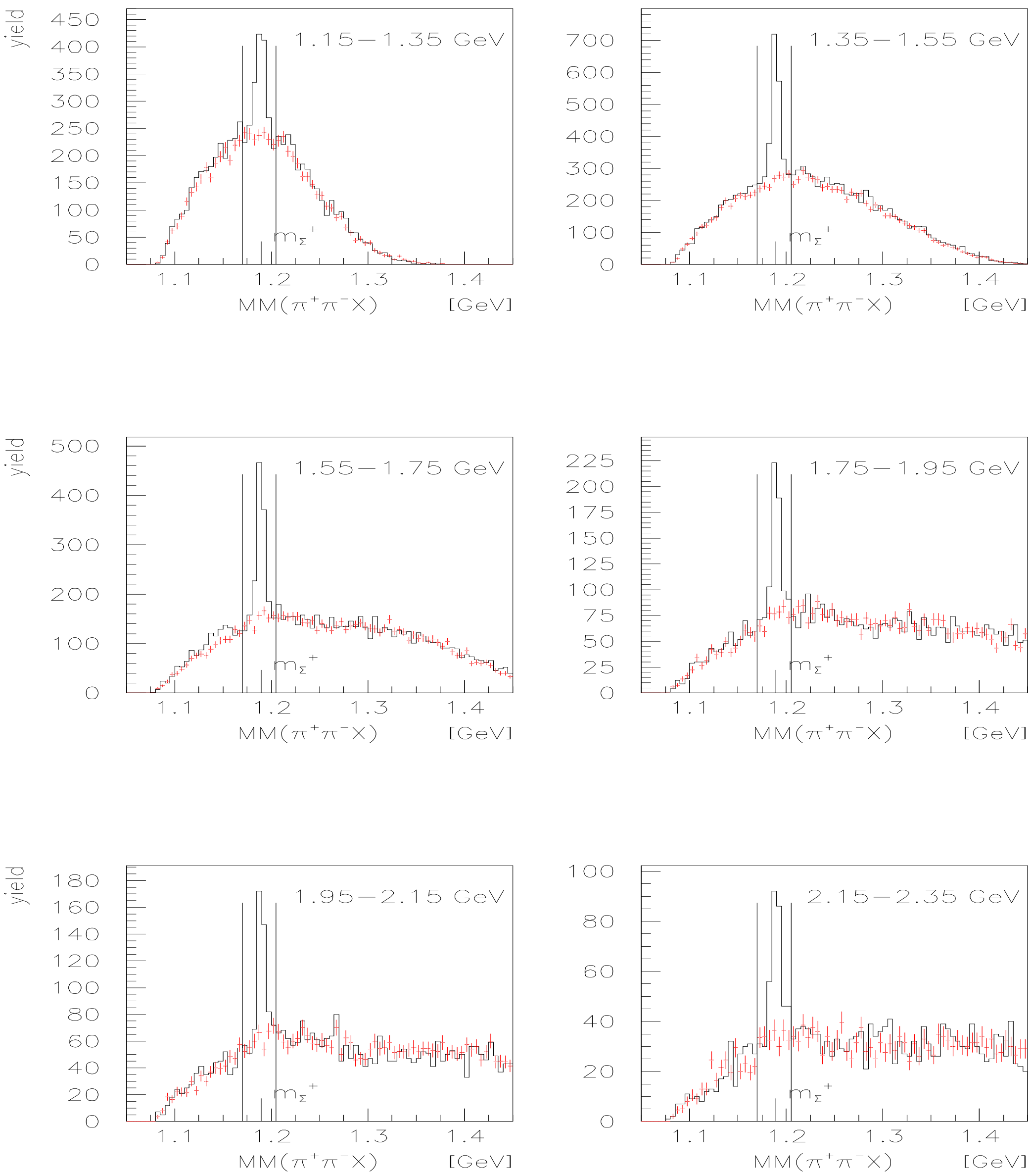

Figure 4.13: MM($\pi^+\pi^- X$) for the $\Sigma^+ \to n\pi^+$ decay channel showing selected events and sideband events. The solid line shows the total of selected events, while data points with error bars show the sideband events. The vertical lines define the region of the event selection from 1.170 to 1.205 GeV, centered around the mass of the Σ^+. The final event sample is determined by subtracting the sideband events from the selected events and summing the results in this region.

4.2.4 Feasibility of a distance cut

All background producing reactions create charged particles which either decay immediately or have a sufficient lifetime to be detected. They appear to come from a single primary vertex. Both the K_S^0 and the Σ^+, however, have a sufficient lifetime that they travel on average about one or two centimeters before decaying. By selecting only those events where the K_S^0 and Σ^+ come from separate displaced vertices, called a distance cut, the background could be greatly reduced while reducing the number of $K_S^0\Sigma^+$ production events marginally. The detected π^+ and π^- particles were used to reconstruct the vertex of the K_S^0. The detected proton was used to create a proton track which was extended back from the region of detection of the proton. In the decay channel $\Sigma^+ \to p\pi^0$ the proton will carry most of the momentum of the Σ^+, so the Σ^+ track can in effect be approximated with that of the proton. The distance between this proton track and the reconstructed K_S^0 vertex was determined by calculating the distance of closest approach as described in Appendix B.

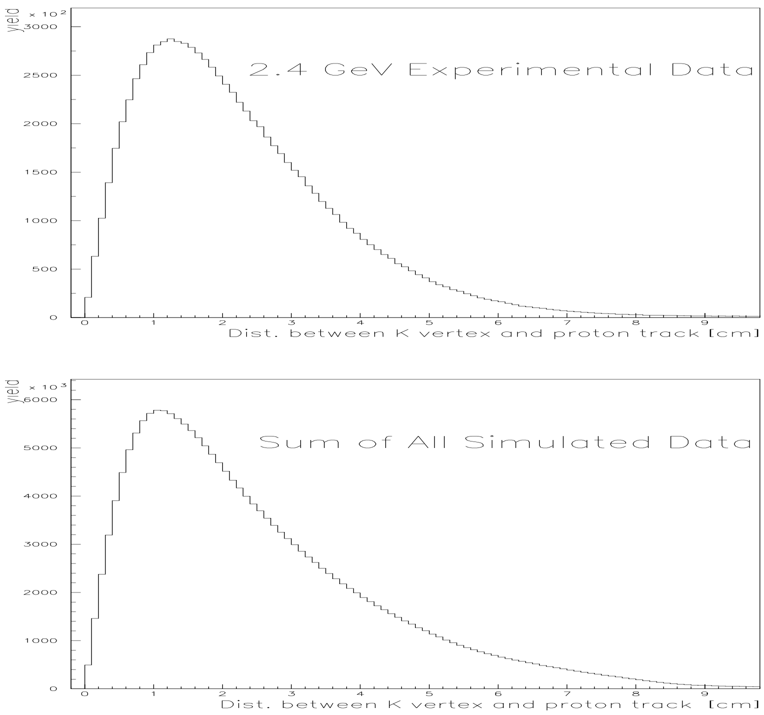

Figure 4.14: The distance betwen the reconstructed K_S^0 vertex and the reconstructed proton track for 2.445 GeV beam energy experimental data on the top plot, and for all simulated processes for $\gamma p \to p\pi^+\pi^-\pi^0$ on the bottom plot.

Figure 4.14 shows the number of detected events as a function of the vertex separation for 2.445 GeV data on the top plot, and all simulated data on the lower plot. These plots show that the vertex resolution is too poor, approximately the size of the K_S^0 and Σ^+ decay paths, for this technique to be useful. Part of the explanation of the poor vertex resolution is that the photon beam has a finite size on the target (approximately 4mm RMS at 2.4 GeV, with tails collimated to 3 cm at the target), so the beam axis is not well determined. Figure 4.15 shows the number of events at this distance for 4 separate simulated decay channels, in the photon energy bin 1.55-1.95 GeV. These figures show how similar the spread of the events are. The data were analyzed using distance cuts ranging from 0.0 to 2.5 cm. Except at the highest energy, this distance cut failed to improve the ratio of signal to background sufficiently to overcome the loss in statistical accuracy due to the decrease in the number of events selected. Based on these results, it was concluded that the vertex resolution is not good enough to use the distance of the vertices to discriminate between $K^0\Sigma^+$ and background events in this experiment.

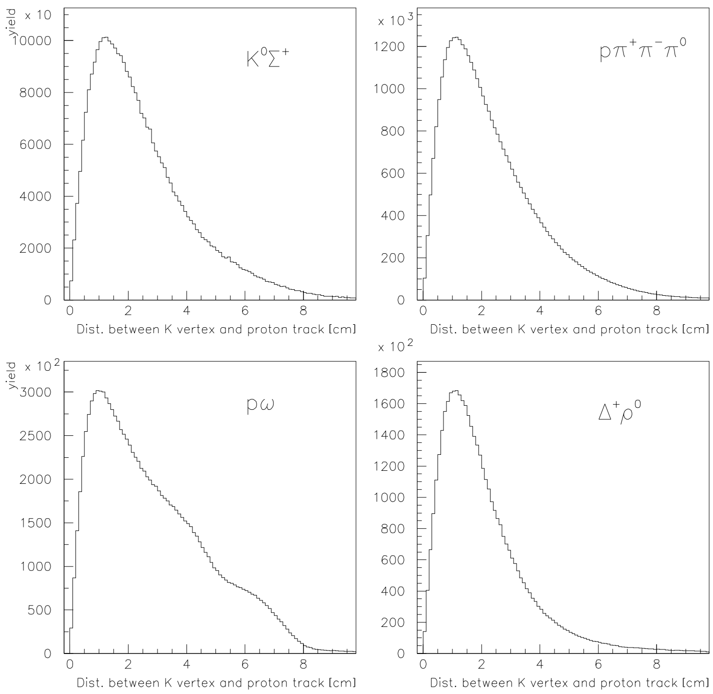

Figure 4.15: Distance between reconstructed K_S^0 vertex and proton track for four simulated *GSIM* processes for the $\Sigma^+ \rightarrow p\pi^0$ decay channel. In order shown are simulated $\gamma p \rightarrow K^0\Sigma^+$, $p\pi^+\pi^-\pi^0$, $p\omega$ and $\Delta^+ \rho^0$.

4.3 Acceptance studies

Not every particle created in the target is detected. The particle may strike one of the Toroid magnet coils or pass through one of the forward or backward uninstrumented regions. The particle may have insufficient energy to pass through all the detectors, or in the case of pions, may decay before reaching the time-of-flight paddles. If any one of the three charged particles in the reactions being studied in this analysis is lost, the event cannot be reconstructed. The purely geometrical acceptance for a single particle in CLAS is about 0.6. Thus the probability of detecting three uncorrelated particles is at best 20%, and other effects will lower this number.

4.3.1 Acceptance calculation for $\gamma p \to \mathbf{K}^0\Sigma^+ \to p\pi^+\pi^-\pi^0$

To calculate the acceptance, $\gamma p \to \mathrm{K}^0\Sigma^+$ events are simulated using a code for CLAS called *GSIM*. *GSIM* is based on a standard Monte Carlo code developed at CERN called GEANT [34]. The *GSIM* program contains a realistic detailed description of the CLAS detector, including all detector elements. Particle energies and angles, decays, and interactions are generated with Monte Carlo techniques. The progress of each generated particle is followed through the detector, and an output which simulates the response of each detector element is generated. These events are further processed through a program called *GPP* (*GSIM* post processing) which removes dead drift chamber wires and time-of-flight (TOF) counters and smears the reconstructed positions in the drift chambers and time information in the TOF counters to better approximate experimental data. The simulated events are then processed through the same version of the reconstruction program as the experimental data as described in Section 3.2. The results of this reconstruction are analyzed using the same procedures as used with the experimental data as described in Section 4. Events for the reaction $\gamma p \to \mathrm{K}^0\Sigma^+$are generated uniformly in 2-body phase space using a program called *psg* (phase space generator). The K_S^0 and Σ^+ decay distributions are generated by the GEANT code.

The simulated data are analyzed to obtain the background-subtracted results of the missing mass from the detected π^+ and π^-. The acceptance in a given energy and angle bin is determined by taking the number of events obtained from this analysis, and dividing by the number of simulated events that were generated in that same energy and angle bin for the given decay channel, $\Sigma^+ \to p\pi^0$ or $\Sigma^+ \to n\pi^+$. Figure 4.16 and Table 4.2 present results for the acceptances as a function of photon energy vs. $\cos(\theta^{cm}_{K_S^0})$. Bin migration, where events generated in a given bin in angle and/or energy are reconstructed as coming from a neighboring bin, is negligible for this analysis due to the large size of the angular and energy bins.

Table 4.2: Acceptance for $\gamma p \to K^0\Sigma^+ \to p\pi^+\pi^-\pi^0$ (in %).

$\cos(\theta^{cm}_{K^0_S})$	E_γ (GeV)					
	1.15-1.25	1.25-1.35	1.35-1.45	1.45-1.55	1.55-1.65	1.65-1.75
0.8 to 0.6	6.09 ±0.13	6.43 ±0.13	6.32 ±0.13	6.45 ±0.13	6.46 ±0.13	6.32 ±0.13
0.6 to 0.4	7.54 ±0.14	8.42 ±0.15	8.39 ±0.15	9.48 ±0.16	9.77 ±0.16	10.37 ±0.16
0.4 to 0.2	8.40 ±0.15	9.20 ±0.16	10.24 ±0.16	11.34 ±0.17	12.49 ±0.18	13.38 ±0.18
0.2 to 0.0	8.77 ±0.15	9.90 ±0.16	11.34 ±0.17	12.85 ±0.18	13.90 ±0.19	14.81 ±0.19
0.0 to -0.2	8.96 ±0.16	9.77 ±0.16	11.22 ±0.17	12.93 ±0.18	14.46 ±0.19	15.62 ±0.20
-0.2 to -0.4	9.07 ±0.16	9.71 ±0.16	10.99 ±0.17	12.78 ±0.18	13.91 ±0.19	14.54 ±0.19
-0.4 to -0.6	8.29 ±0.15	8.93 ±0.15	9.54 ±0.16	11.30 ±0.17	12.18 ±0.18	12.96 ±0.18
-0.6 to -0.8	7.47 ±0.14	7.52 ±0.14	7.77 ±0.14	8.17 ±0.17	8.97 ±0.16	9.34 ±0.16
	1.75-1.85	1.85-1.95	1.95-2.05	2.05-2.15	2.15-2.25	2.25-2.35
0.8 to 0.6	5.89 ±0.13	5.71 ±0.12	5.49 ±0.12	5.56 ±0.12	5.62 ±0.12	5.72 ±0.14
0.6 to 0.4	10.54 ±0.17	10.98 ±0.17	11.11 ±0.17	11.54 ±0.17	11.89 ±0.17	11.97 ±0.20
0.4 to 0.2	13.76 ±0.19	14.33 ±0.19	14.61 ±0.19	15.09 ±0.19	14.94 ±0.19	15.49 ±0.22
0.2 to 0.0	15.59 ±0.20	16.74 ±0.20	17.33 ±0.20	17.47 ±0.20	17.67 ±0.20	17.43 ±0.24
0.0 to -0.2	16.22 ±0.20	16.96 ±0.20	18.15 ±0.21	18.98 ±0.21	19.15 ±0.21	18.91 ±0.24
-0.2 to -0.4	15.43 ±0.20	16.24 ±0.20	16.56 ±0.20	17.63 ±0.21	18.85 ±0.21	19.09 ±0.24
-0.4 to -0.6	13.58 ±0.19	14.00 ±0.19	14.49 ±0.19	15.04 ±0.19	16.08 ±0.20	16.00 ±0.23
-0.6 to -0.8	9.31 ±0.16	9.84 ±0.16	10.09 ±0.16	11.01 ±0.17	11.13 ±0.17	11.41 ±0.20

Processing the simulated $\gamma p \to K^0\Sigma^+$ data through the analysis code gives the values for the missing and invariant masses close to the expected masses of the particles. The top row of Fig. 4.17 shows for three photon energy bins, 1.15-1.55, 1.55-1.95 and 1.95-2.35 GeV, and for $0.0 < \cos(\theta^{cm}_{K^0_S}) < 0.2$, the calculated missing mass from the detected π^+, $\pi^-$and proton. There is a peak at the π^0 mass as expected. As with the experimental data, an event selection is made in the analysis code to exclude data outside of the mass region from 0.07 to 0.20 GeV. The middle row of Fig. 4.17 shows the invariant mass of the detected π^+ and π^- for simulated $K^0\Sigma^+$ data, where the expected peak is at the mass of the K^0_S for the same energy and angular bins. As the $M(\pi^+\pi^-)$ is centered around 0.4975 GeV, this value is used as the center of the region of selected events. Events are selected in a range of 0.4975 ± 0.0135 GeV, and then sidebands events are selected in a range of 0.027 GeV to the left and right of the selected events. The bottom row of Fig. 4.17 shows results for $MM(\pi^+\pi^-X)$, with a distinct peak at the mass of the Σ^+. The dotted curve under the main curve contains the sideband events to be subtracted. Here, as expected, there are very few sideband events in the $\gamma p \to K^0\Sigma^+$ reaction, indicating that we are not losing many good events by making this subtraction. The loss of $\gamma p \to K^0\Sigma^+$ events due to sideband subtraction for the $\Sigma^+ \to p\pi^0$ decay channel is about 2.5% at higher photon energies and goes down to about 1.5% at higher photon energies.

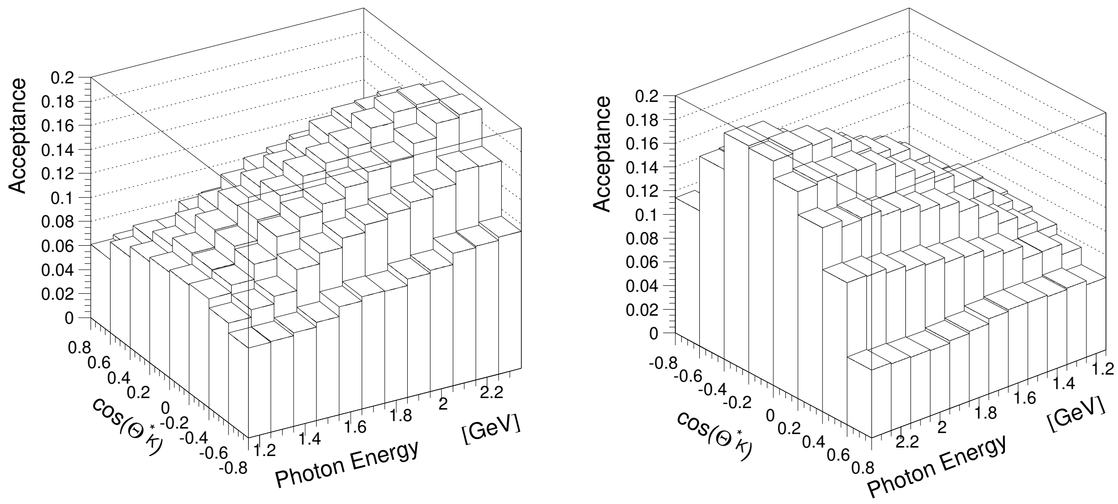

Figure 4.16: Acceptance values for indicated bins in energy and $\cos(\theta^{cm}_{K^0_S})$ for the $\Sigma^+ \rightarrow p\pi^0$ decay channel. Shown are two views of the same data, the second figure rotated by 180° about the vertical axis so that bins hidden in one view are visible in the other.

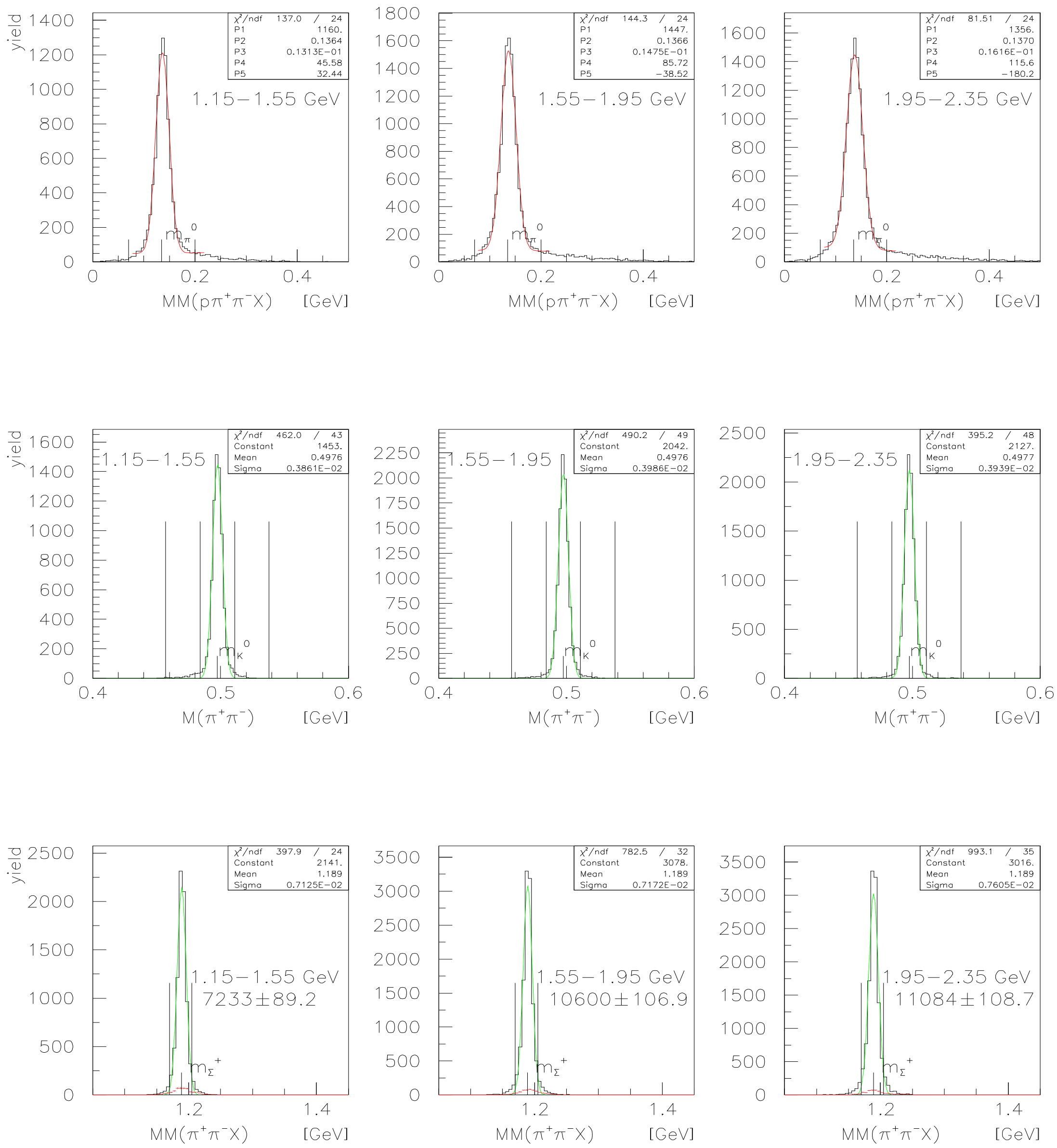

Figure 4.17: The top plots show $\mathrm{MM}(p\pi^+\pi^-X)$ for three photon energy bins for $0.0 < \cos(\theta^{cm}_{K^0_S}) < 0.2$ for simulated $\gamma p \to \mathrm{K}^0\Sigma^+ \to p\pi^+\pi^-\pi^0$ events, analyzed for the $\Sigma^+ \to p\pi^0$ channel. The middle and bottom plots show $\mathrm{M}(\pi^+\pi^-)$ and $\mathrm{MM}(\pi^+\pi^-X)$ using the same photon energy and angle bins. Gaussian fits are made to the top and middle rows, with the fit parameters displayed. The vertical lines shown are from the event selection criteria. The results of the sideband subtraction along with the associated statistical uncertainty are shown in the figures in the bottom row.

4.3.2 Simulated background processes for the decay channel $\gamma p \to \mathbf{K}^0\Sigma^+ \to p\pi^+\pi^-\pi^0$

To better understand the structure of the background in the experimental data, various background reactions are simulated and analyzed using the same reconstruction and analysis code as with experimental data. By observing the shapes and relative magnitudes of these background reactions we gain further confidence in the extraction of good events from experimental data. All of these simulated processes are chosen to satisfy the requirement in the code of one and only one detected proton, π^+ and π^-.

4.3.2.1 $\gamma p \to p\pi^+\pi^-\pi^0$ phase space distribution

$\gamma p \to p\pi^+\pi^-\pi^0$ events are generated with a flat distribution in four-particle phase space. The threshold for this reaction is 0.506 GeV. Since the threshold for $\gamma p \to \mathrm{K}^0\Sigma^+$ is 1.0475 GeV, background from this reaction is expected throughout the data set. The top plots in Fig. 4.18 show $\mathrm{MM}(p\pi^+\pi^-X)$ for this simulated data set, and also show that this background peaks around the mass of the π^0, so almost all of these events will pass the first cut on $\mathrm{MM}(p\pi^+\pi^-X)$. These distributions are wider than those for the $\mathrm{K}^0\Sigma^+$ simulation as expected, since a phase space distribution will include larger variations in momenta than simulated $\mathrm{K}^0\Sigma^+$ data. The middle plots in Fig. 4.18 show that results from $\mathrm{M}(\pi^+\pi^-)$ analysis yields give a mostly flat distribution. This is encouraging as the procedure for background subtraction assumes either a flat or constant sloped approximation for the background processes. The bottom plots in Fig. 4.18 show $\mathrm{MM}(\pi^+\pi^-X)$ results for these simulated data, the data points with error bars being the sideband events. Since the sideband events overlap well with the selected events, this reaction will have a low percentage of events contaminating the final event sample after the sideband subtraction. The number of events remaining after sideband subtraction and the associated statistical uncertainty are shown in each plot in the bottom row. These data show that the background events are removed by this procedure.

4.3.2.2 $\gamma p \to p\omega \to p\pi^+\pi^-\pi^0$

Photoproduced ω mesons are simulated with ω decaying into $\pi^+\pi^-\pi^0$ with a branching ratio of 89%. The threshold for this reaction is 1.105 GeV, so background from this reaction is expected throughout the data set. The top plots in Fig. 4.19 show $\mathrm{MM}(p\pi^+\pi^-X)$ for these events. As with the $p\pi^+\pi^-\pi^0$ events these are distinct peaks around the π^0 mass that are wider than those for the simulated $\mathrm{K}^0\Sigma^+$ events. The middle plots in Fig. 4.19 show the M($\pi^+\pi^-$) plot for these events. These plots are not as flat as they were for the $p\pi^+\pi^-\pi^0$, but in the region around the K_S^0 mass they appear to be flat enough for the sideband subtraction. The bottom plots in Figure 4.19 show that the background subtraction technique works well for this background as well.

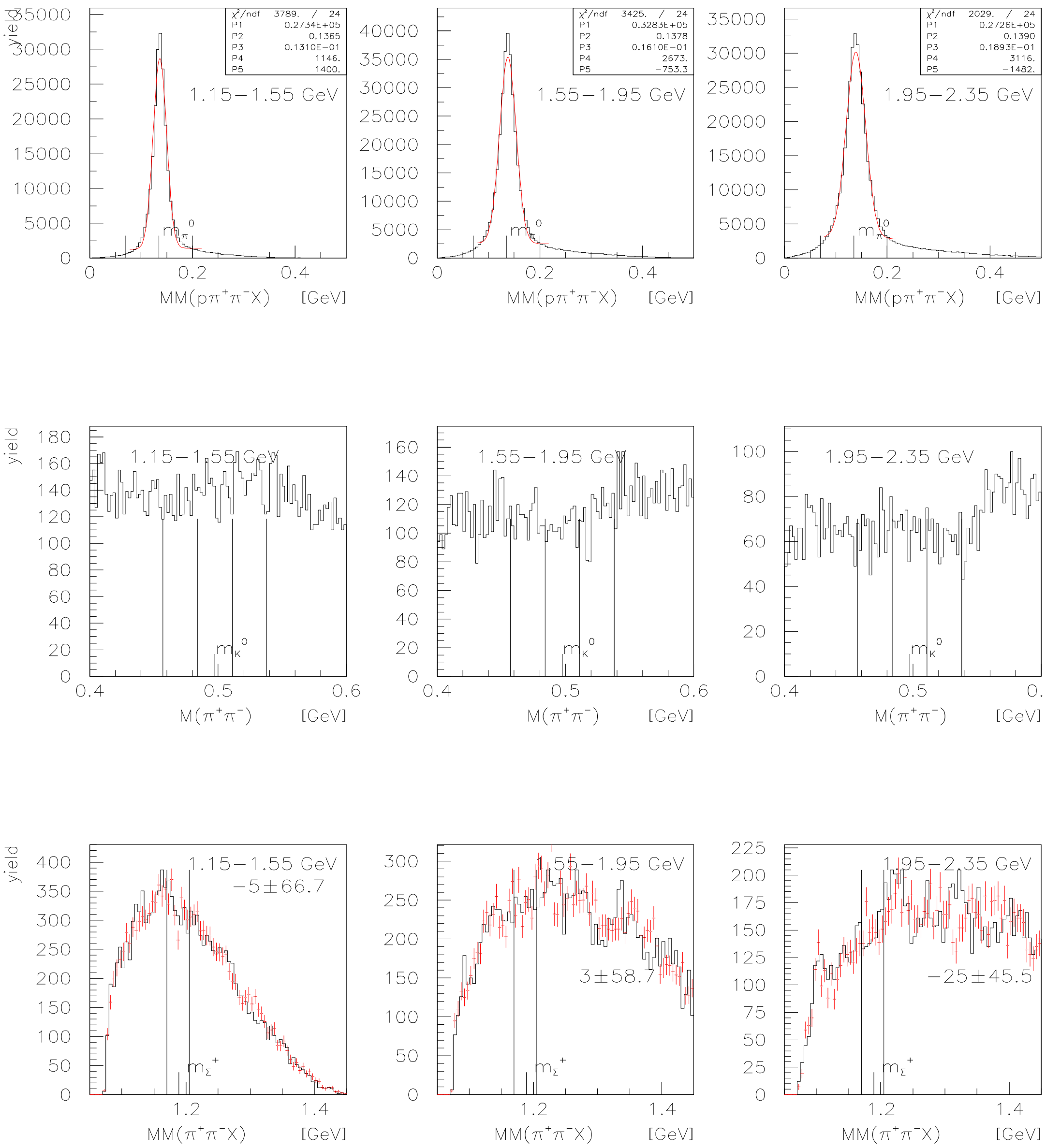

Figure 4.18: The top plots show MM($p\pi^+\pi^-X$) for three photon energy bins for $0.0 < \cos(\theta^{cm}_{(\pi^+\pi^-)}) < 0.2$ for simulated $\gamma p \rightarrow p\pi^+\pi^-\pi^0$ phase space distribution events. The middle and bottom plots show M($\pi^+\pi^-$) and MM($\pi^+\pi^-X$) using the same photon energy and angle bins. Gaussian fits are made in the top row, with the fit parameters displayed. The vertical lines shown are from the event selection criteria. The results of the sideband subtraction along with the associated statistical uncertainty are shown in the figures in the bottom row.

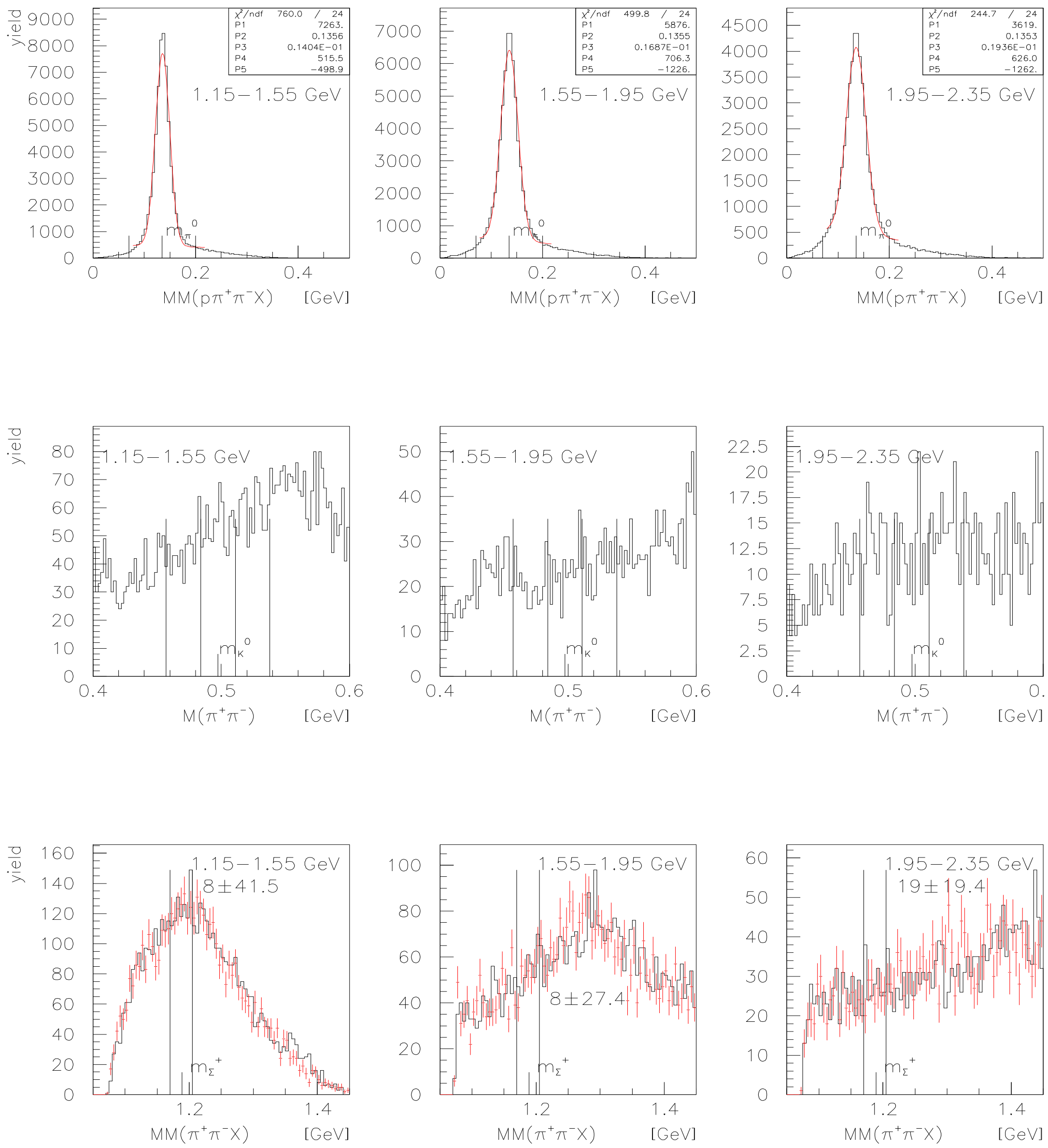

Figure 4.19: The top plots show MM($p\pi^+\pi^-X$) for three photon energy bins for $0.0 < \cos(\theta^{cm}_{(\pi^+\pi^-)}) < 0.2$ for simulated $\gamma p \rightarrow p\omega \rightarrow p\pi^+\pi^-\pi^0$ events. The middle and bottom plots show M($\pi^+\pi^-$) and MM($\pi^+\pi^-X$) using the same photon energy and angle bins. Gaussian fits are made in the top row, with the fit parameters displayed. The vertical lines shown are from the event selection criteria. The results of the sideband subtraction along with the associated statistical uncertainty are shown in the figures in the bottom row.

4.3.2.3 $\gamma p \rightarrow \Delta^+ \rho^0$

Events for the reaction $\gamma p \rightarrow \Delta^+ \rho^0 \rightarrow$ (p π^0) ($\pi^+\pi^-$) were also simulated. The threshold for this reaction is 1.703 GeV, so background from this reaction is expected in the higher photon energy ranges in the data set. However, since the Δ and ρ are very broad, events from this process can occur in all photon energy bins of interest here. The top plots in Fig. 4.20 show MM($p\pi^+\pi^- X$)and how these events show a peak at the mass of the π^0. The middle plots in Fig. 4.20 show an upward sloping background for M($\pi^+\pi^-$). In the third row, this background process produces a false peak close to the Σ^+ mass, but this peak is removed by the sideband subtraction.

The background simulated distributions agree well with the experimental background obtained for MM($\pi^+\pi^- X$). Since the sideband events are subtracted from the selected events, we can be confident that for each of the investigated background processes an appropriate quantity of background events is being correctly subtracted in the analysis of experimental data.

4.3.2.4 Other background reactions

As a further check on the reconstruction process, additional processes were simulated which do not produce a $p\pi^+\pi^-\pi^0$ final state, to confirm that they would be rejected by the event selection. The first such reaction simulated was $\gamma p \rightarrow p\ \pi^+\pi^-$ phase space distribution. As the code only accepts data with a missing mass around the mass of the π^0 resulting from MM($p\pi^+\pi^- X$), events from a $\gamma p \rightarrow p\ \pi^+\pi^-$ should not pass this cut. However, due to the missing mass resolution and large cross section for $\gamma p \rightarrow p\ \pi^+\pi^-$, a study of this reaction is important. Figure 4.21 shows that only a negligible fraction of the events satisfy the selection criteria of 0.07 to 0.20 GeV on MM($p\pi^+\pi^- X$), and that only an insignificant number of events pass our event selection criteria. The decay channel $\gamma p \rightarrow p\rho \rightarrow p\ \pi^+\pi^-$ was also simulated . Few of these events should survive the π^0 mass cut, and this analysis showed a similar lack of events as shown in Fig. 4.21. Another simulated channel, $\gamma p \rightarrow p\ \pi^+\pi^-\pi^+\pi^-$, was also rejected by this analysis.

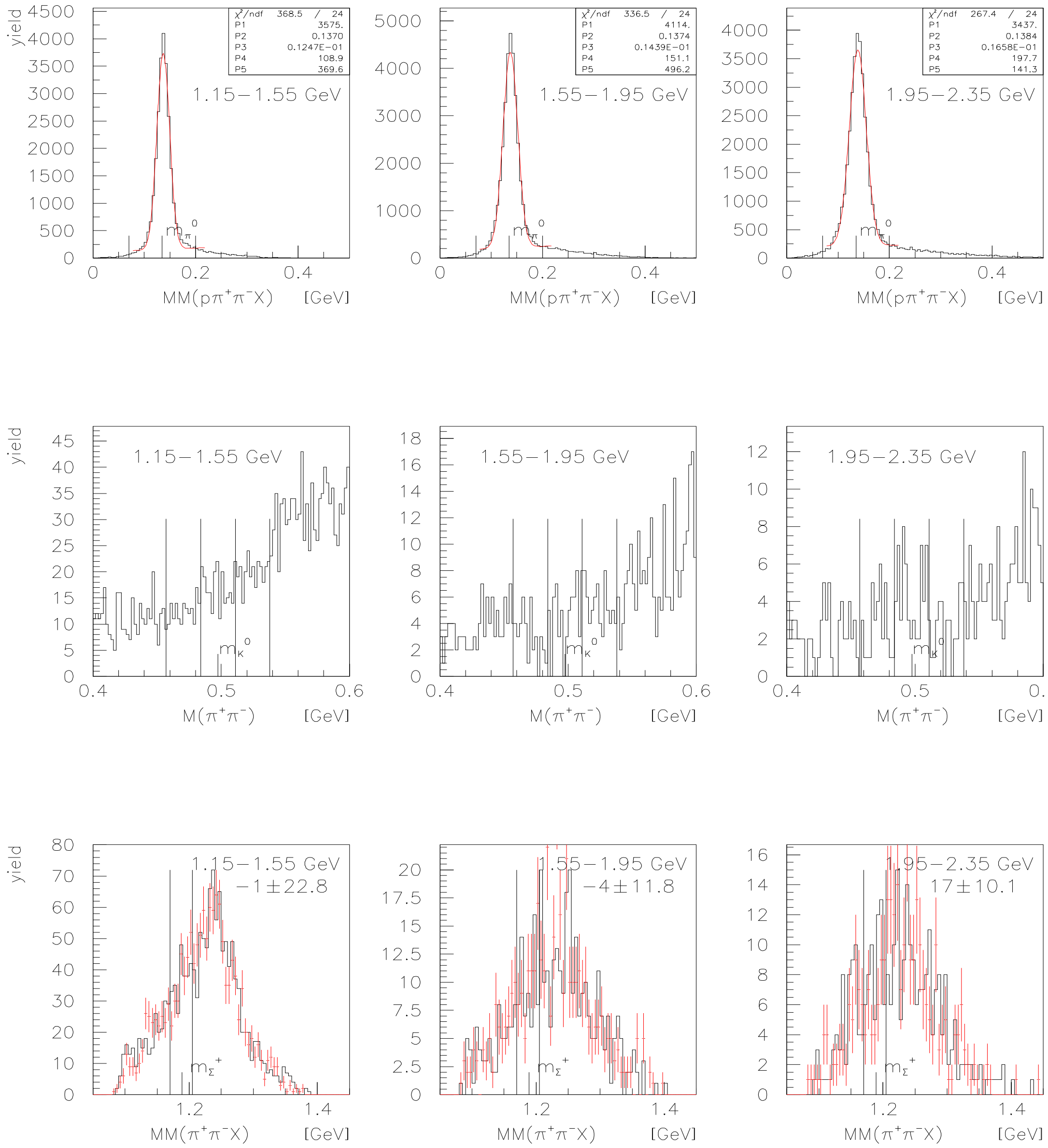

Figure 4.20: The top plots show MM($p\pi^+\pi^-X$) for three photon energy bins for $0.0 < \cos(\theta^{cm}_{(\pi^+\pi^-)}) < 0.2$ for simulated $\gamma p \rightarrow \Delta^+\rho^0 \rightarrow p\pi^+\pi^-\pi^0$ events. The middle and bottom plots show M($\pi^+\pi^-$) and MM($\pi^+\pi^-X$) using the same photon energy and angle bins. Gaussian fits are made in the top row, with the fit parameters displayed. The vertical lines shown are from the event selection criteria. The results of the sideband subtraction along with the associated statistical uncertainty are shown in the figures in the bottom row.

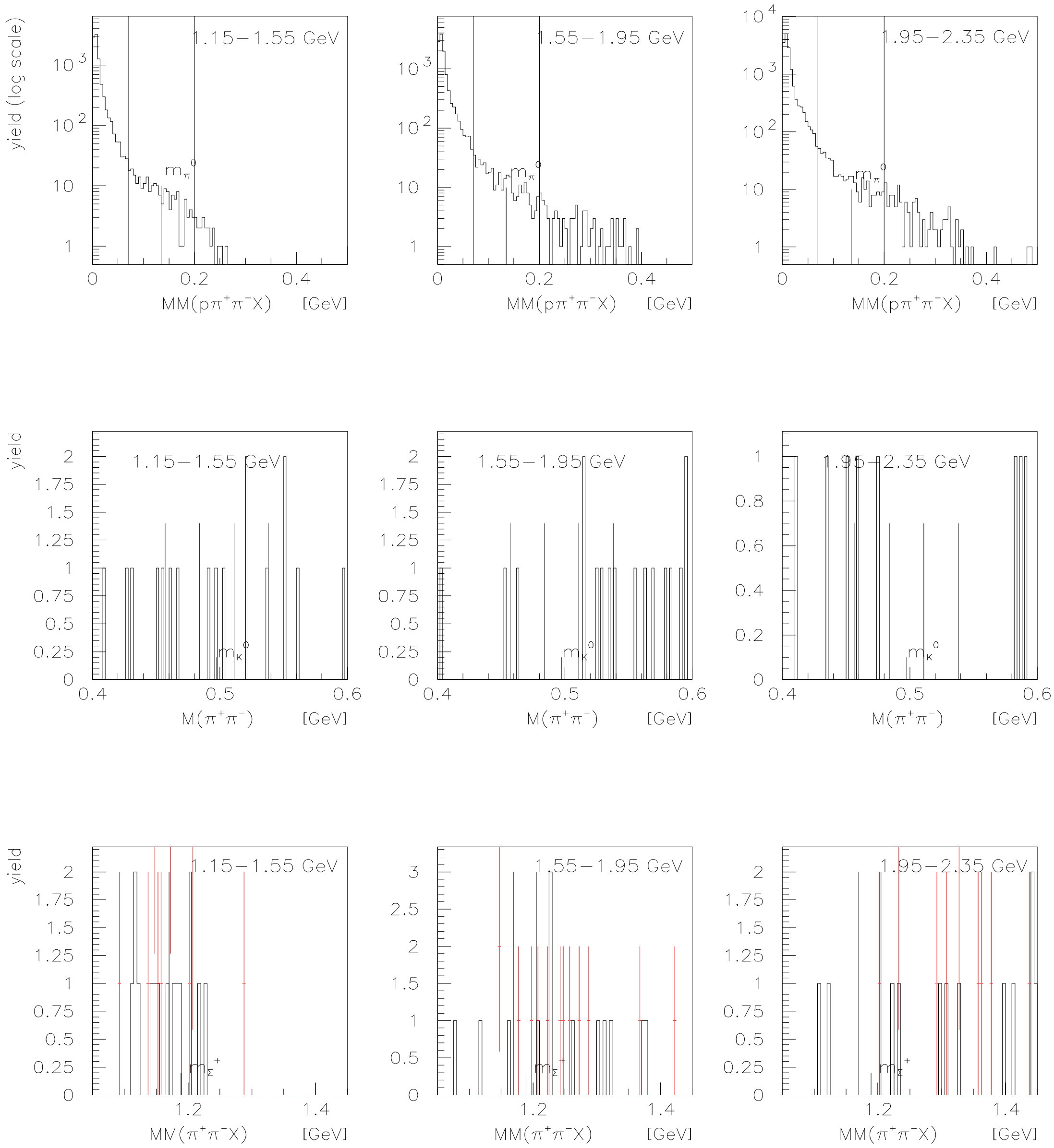

Figure 4.21: The top plots show MM($p\pi^+\pi^-X$) for three photon energy bins for $0.0 < \cos(\theta^{cm}_{(\pi^+\pi^-)}) < 0.2$ for simulated $\gamma p \to p\ \pi^+\pi^-$ events. The middle and bottom plots show M($\pi^+\pi^-$) and MM($\pi^+\pi^-X$) using the same photon energy and angle bins. These plots show that events from this process will not pass our event selection criteria.

4.3.2.5 Comparison of simulated processes with experimental data

To compare these results with experimental data, first a comparison between experimental results and results for each simulated process can be made.

In order to test the yield extraction technique, results from the simulated processes presented in this section, $\gamma p \rightarrow \mathrm{K}^0\Sigma^+$, $p\omega \rightarrow p\pi^+\pi^-\pi^0$, $p\pi^+\pi^-\pi^0$ and $\Delta^+\rho^0$ were combined and analyzed. Figure 4.22 shows results for $\mathrm{MM}(\pi^+\pi^- X)$ from the combination of these reactions in the indicated bins. Data were combined based on the measured cross section of $\gamma p \rightarrow p\omega$ and the measured cross section for $\gamma p \rightarrow p\pi^+\pi^-\pi^0$. Since the cross section for $\gamma p \rightarrow \Delta^+\rho^0$ is not well known, this cross section was adjusted to fit the distribution of experimental data. The simulated data for $p\omega$ and $p\pi^+\pi^-\pi^0$ have similar shapes in this photon energy range with the larger contribution from $p\omega$. The contribution from the $\Delta^+\rho^0$ is estimated to be very small in the first few photon energy bins, but is estimated to have a greater contribution at higher photon energies, with a maximum around 1.225 GeV in $\mathrm{MM}(\pi^+\pi^- X)$.

This figure can be directly compared with Fig. 4.9 which contains the same plots for experimental data. The combination of the backgrounds appears similar to the experimental data. In both simulated and experimental data there is a high background in the photon energy bin 1.15-1.35 GeV which decreases to zero at about 1.35 GeV in $\mathrm{MM}(\pi^+\pi^- X)$. This is mainly due to the $\gamma p \rightarrow p\omega \rightarrow p\pi^+\pi^-\pi^0$ contribution but is also from the $\gamma p \rightarrow \Delta^+\rho^0 \rightarrow p\pi^+\pi^-\pi^0$ contribution as is shown in the first plot in Fig. 4.22. The background in the simulated and experimental data appear to exhibit similar properties in $\mathrm{MM}(\pi^+\pi^- X)$ in these photon energy bins. From this it is concluded that the simulated background processes explain well the properties of the background in experimental data.

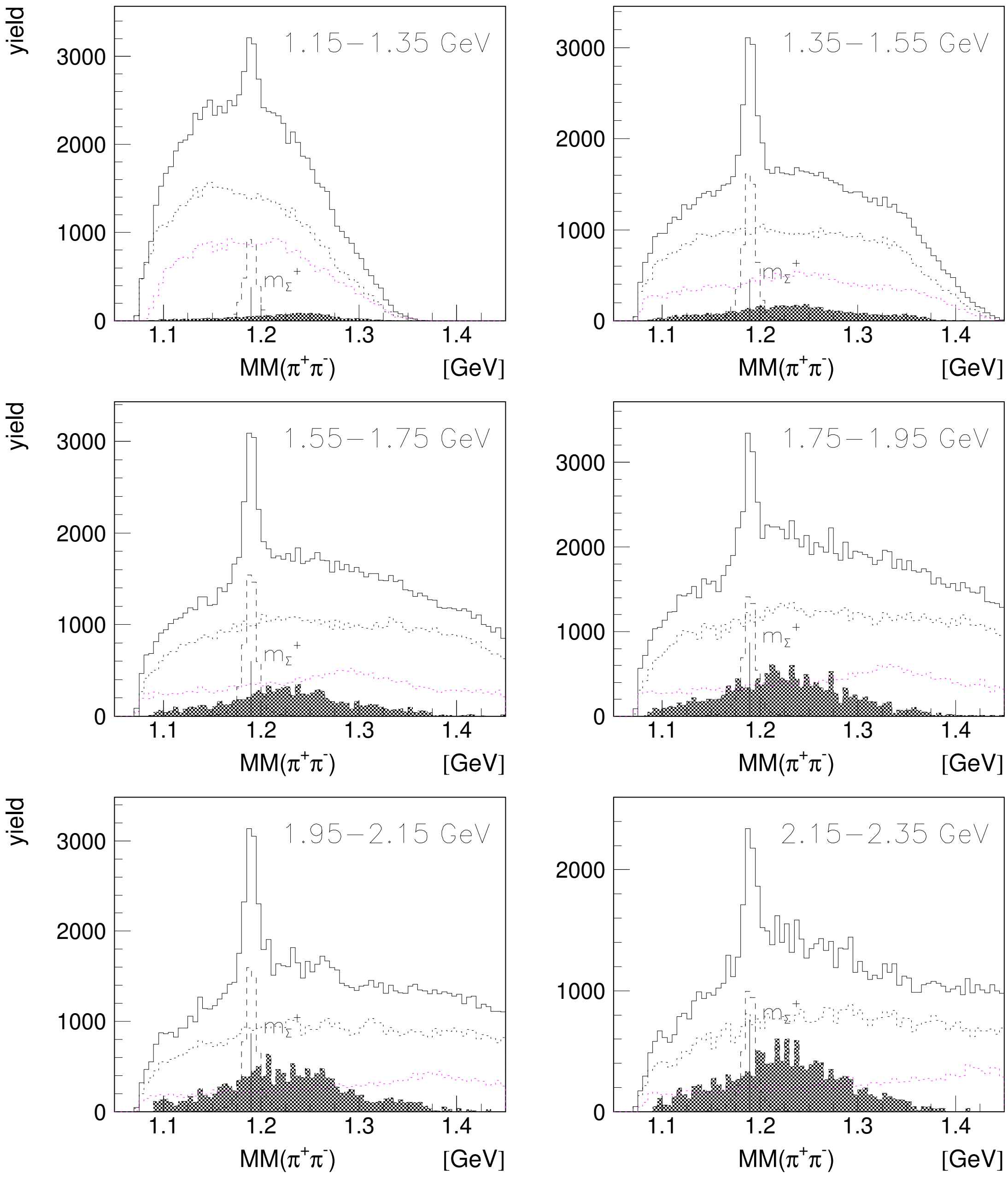

Figure 4.22: MM($\pi^+\pi^- X$) for the combined simulated processes analyzed for the $\Sigma^+ \to p\pi^0$ decay channel for all angles in six photon energy bins. The dashed line is for $\mathrm{K}^0\Sigma^+$, the dotted line is for $\gamma p \to p\omega \to p\pi^+\pi^-\pi^0$, the hashed(grey) line is for $\gamma p \to p\pi^+\pi^-\pi^0$and the filled in region is for $\gamma p \to \Delta^+\rho^0 \to p\pi^+\pi^-\pi^0$. The solid line shows the sum of these processes.

Table 4.3 presents the number of events from each simulated background process that passed the event selection criteria into the final event sample (FES) for identified Σ^+ events. The second column on the table presents the scaling factor for each reaction which was used to combine the processes in Fig. 4.22 based on the number of events generated and the cross sections of the reactions. The number of events for the reaction is multiplied by this scaling factor, and then divided by the number of $\gamma p \rightarrow K^0\Sigma^+$ events for the photon energy to determine the % of misidentified $\gamma p \rightarrow K^0\Sigma^+$ events, as presented in the third column. It is clear from this table that the number of background events that are misidentified as $\gamma p \rightarrow K^0\Sigma^+$ events in our final event sample is very small, with the highest total background contamination being 3.5% in the photon energy bin 1.55-1.95 GeV. Therefore, our sideband background subtraction is very efficient in eliminating background processes from our final event sample for the $\Sigma^+ \rightarrow p\pi^0$ decay channel used to calculate cross sections.

Table 4.3: Final event samples and contamination percentages from background processes for the decay channel $\Sigma^+ \rightarrow p\pi^0$.

1.15-1.55 GeV	FES	Scale	% background contamination
$\gamma p \rightarrow K^0\Sigma^+$	7233 ± 89		
$\gamma p \rightarrow p\pi^+\pi^-\pi^0$	-5 ± 66	1.8	1.5%
$\gamma p \rightarrow p\omega$	8 ± 41	1.8	1.2%
$\gamma p \rightarrow \Delta^+\rho^0$	-1 ± 23	1.0	0.3 %
1.55-1.95 GeV	FES		
$\gamma p \rightarrow K^0\Sigma^+$	10600 ± 107		
$\gamma p \rightarrow p\pi^+\pi^-\pi^0$	3 ± 59	4.3	2.5%
$\gamma p \rightarrow p\omega$	8 ± 27	2.7	0.9%
$\gamma p \rightarrow \Delta^+\rho^0$	-4 ± 12	1.8	0.1%
1.95-2.35 GeV	FES		
$\gamma p \rightarrow K^0\Sigma^+$	11084 ± 109		
$\gamma p \rightarrow p\pi^+\pi^-\pi^0$	-25 ± 45	6.7	1.2%
$\gamma p \rightarrow p\omega$	19 ± 19	3.3	1.1%
$\gamma p \rightarrow \Delta^+\rho^0$	17 ± 10	3.3	0.8%

4.3.3 Acceptance calculation for $\gamma p \rightarrow \mathrm{K}^0\Sigma^+ \rightarrow n\pi^+\pi^+\pi^-$

To obtain acceptance values for the decay channel $\gamma p \rightarrow \mathrm{K}^0\Sigma^+ \rightarrow n\pi^+\pi^+\pi^-$ events were also simulated and analyzed. However, MM($\pi^+\pi^+\pi^- X$) events are now selected around the neutron mass. The acceptance is obtained using the same procedure as for the $\Sigma^+ \rightarrow p\pi^0$ decay channel. Figure 4.23 and Table 4.4 present results of the acceptance as a function of energy vs. $\cos(\theta^{cm}_{K^0_S})$ in the center-of-mass frame for $\gamma p \rightarrow \mathrm{K}^0\Sigma^+ \rightarrow n\pi^+\pi^+\pi^-$.

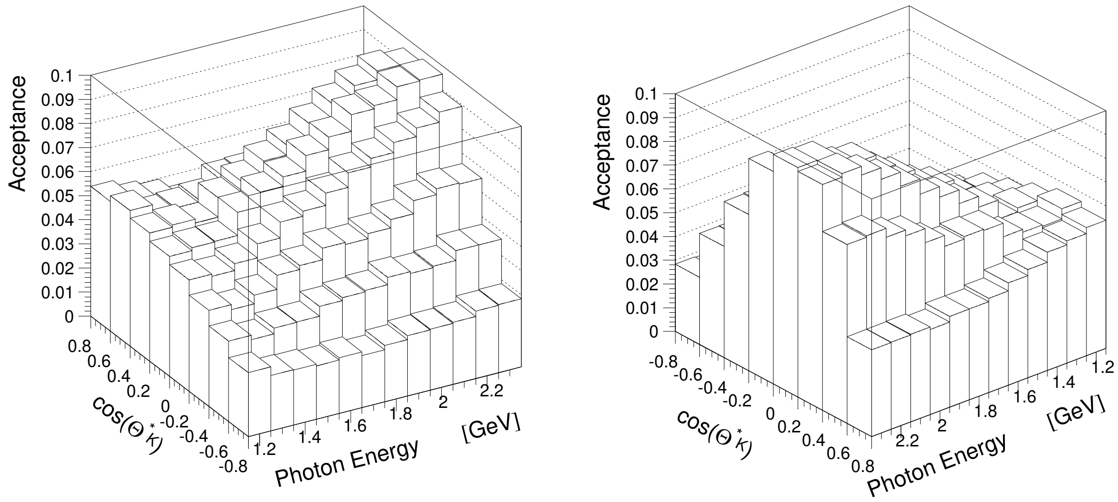

Figure 4.23: Acceptance values for indicated bins in energy and $\cos(\theta^{cm}_{K^0_S})$ for the $\Sigma^+ \rightarrow n\pi^+$ decay channel. Shown are two views of the same data, the second figure rotated by 180° about the vertical axis so that bins hidden in one view are visible in the other.

The top row of Fig. 4.24 shows MM($\pi^+\pi^+\pi^- X$) for the indicated bins. There is a distinct peak at the neutron mass as expected. As with the experimental data, an event selection in made to exclude data outside the range 0.85 to 1.05 GeV. The middle row of Fig. 4.24 shows for the same energy and angles the invariant mass of the detected π^+ and π^- for $\mathrm{K}^0\Sigma^+$ data, where with the expected peak at the mass of the K^0_S. As with the $\Sigma^+ \rightarrow p\pi^0$ decay channel, events are selected in a range of 0.4975 $\pm$ 0.0135, and sideband events are chosen in 0.0270 GeV wide regions to the left and right of the selected event range. The bottom row of Fig. 4.24 shows for the simulated data the missing mass of the detected π^+ and π^- where there is a distinct peak at the mass of the Σ^+. The dotted curve under the main curve represents the sideband background subtraction determined from the M($\pi^+\pi^-$) plot as described above. As for the $\Sigma^+ \rightarrow p\pi^0$ decay channel there is a very small contribution from subtracted

Table 4.4: Acceptance for $\gamma p \to K^0\Sigma^+ \to n\pi^+\pi^+\pi^-$ (in %).

$\cos(\theta^{cm}_{K^0_S})$	E_γ (GeV)					
	1.15-1.25	1.25-1.35	1.35-1.45	1.45-1.55	1.55-1.65	1.65-1.75
0.8 to 0.6	5.39 ±0.13	5.14 ±0.13	4.97 ±0.12	4.55 ±0.12	4.30 ±0.12	3.96 ±0.11
0.6 to 0.4	5.63 ±0.13	5.20 ±0.13	5.26 ±0.13	5.38 ±0.13	5.95 ±0.13	6.00 ±0.14
0.4 to 0.2	5.32 ±0.13	5.42 ±0.13	5.26 ±0.13	6.07 ±0.14	6.53 ±0.14	7.11 ±0.15
0.2 to 0.0	4.98 ±0.13	5.10 ±0.13	5.12 ±0.13	6.09 ±0.14	6.68 ±0.14	7.07 ±0.15
0.0 to -0.2	4.63 ±0.12	4.54 ±0.12	4.82 ±0.12	5.40 ±0.13	6.07 ±0.14	6.28 ±0.14
-0.2 to -0.4	3.99 ±0.11	3.78 ±0.11	4.14 ±0.12	4.72 ±0.12	4.88 ±0.12	5.36 ±0.13
-0.4 to -0.6	3.34 ±0.11	3.15 ±0.10	3.39 ±0.10	3.41 ±0.11	3.81 ±0.11	3.93 ±0.11
-0.6 to -0.8	2.65 ±0.09	2.30 ±0.09	2.28 ±0.09	2.21 ±0.09	2.31 ±0.09	2.15 ±0.08
	1.75-1.85	1.85-1.95	1.95-2.05	2.05-2.15	2.15-2.25	2.25-2.35
0.8 to 0.6	3.82 ±0.11	3.82 ±0.11	3.58 ±0.10	3.68 ±0.11	3.66 ±0.11	3.65 ±0.12
0.6 to 0.4	5.90 ±0.14	6.36 ±0.14	6.96 ±0.14	7.21 ±0.15	7.59 ±0.15	7.53 ±0.17
0.4 to 0.2	7.55 ±0.15	8.19 ±0.16	8.79 ±0.16	9.28 ±0.16	9.65 ±0.17	9.50 ±0.19
0.2 to 0.0	7.72 ±0.15	8.24 ±0.16	8.94 ±0.16	9.07 ±0.16	9.61 ±0.17	9.66 ±0.19
0.0 to -0.2	6.79 ±0.14	7.39 ±0.15	7.75 ±0.15	8.17 ±0.15	8.52 ±0.16	8.94 ±0.18
-0.2 to -0.4	5.28 ±0.13	5.49 ±0.13	5.83 ±0.13	6.38 ±0.14	6.63 ±0.14	6.58 ±0.16
-0.4 to -0.6	3.99 ±0.11	4.30 ±0.11	4.22 ±0.11	4.28 ±0.12	4.69 ±0.12	4.68 ±0.14
-0.6 to -0.8	2.34 ±0.09	2.50 ±0.09	2.53 ±0.09	2.58 ±0.09	2.80 ±0.09	2.83 ±0.11

"background" events in the $\gamma p \to K^0\Sigma^+$ reaction, indicating that few of these events are being lost by making this background subtraction. For the $\Sigma^+ \to n\pi^+$ decay channel, about 7% of the $\gamma p \to K^0\Sigma^+$ events are lost by the sideband subtraction at lower photon energies, which goes down to about a 4% loss at higher photon energies.

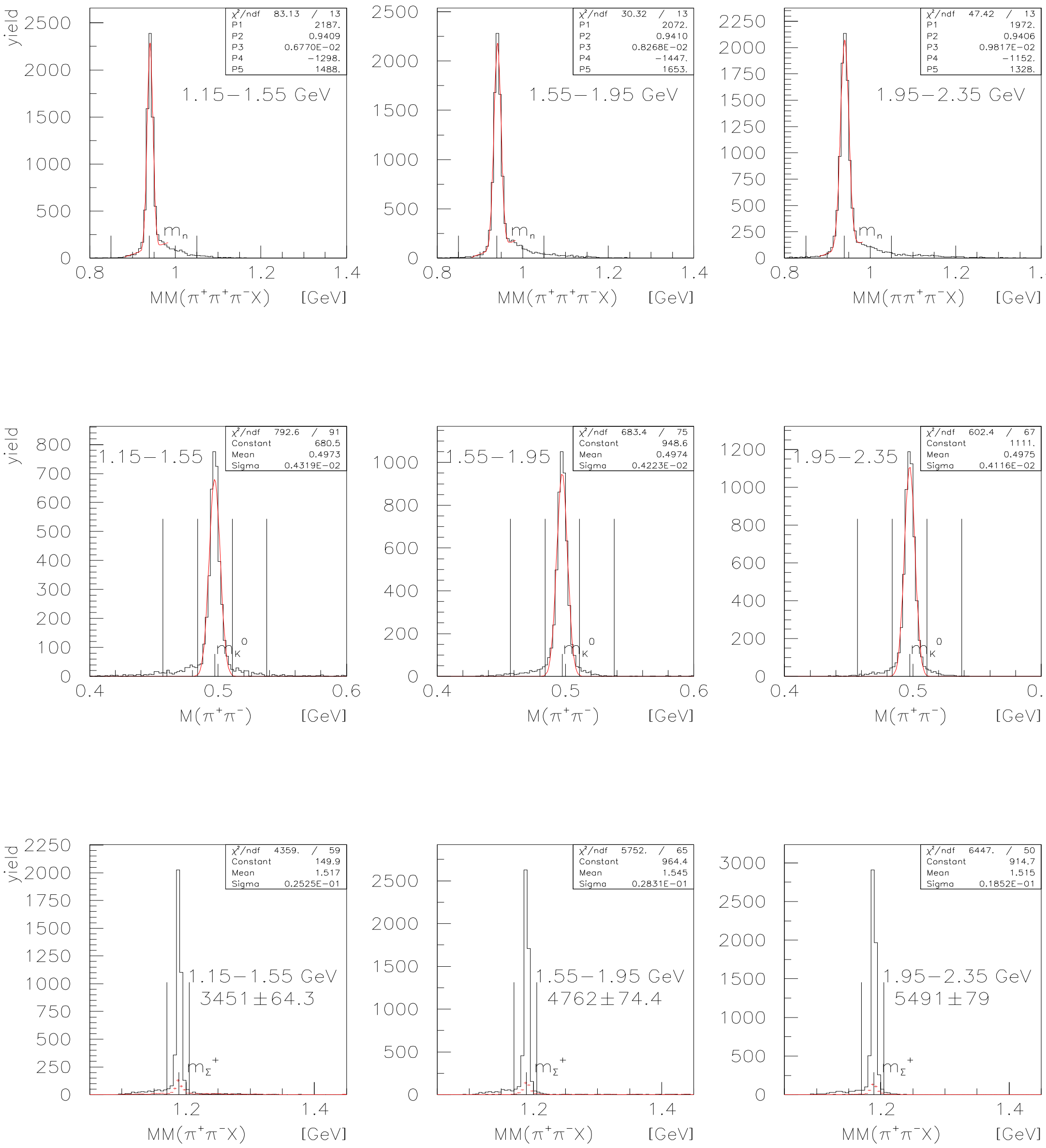

Figure 4.24: The top plots show MM($\pi^+\pi^+\pi^- X$) for three photon energy bins for $0.0 < \cos(\theta^{cm}_{K^0_S}) < 0.2$ for simulated $\gamma p \to$K$^0\Sigma^+ \to n\pi^+\pi^+\pi^-$ events, analyzed for the $\Sigma^+ \to n\pi^+$ channel. The middle and bottom plots show M($\pi^+\pi^-$) and MM($\pi^+\pi^- X$) using the same photon energy and angle bins. Gaussian fits are made to the top and middle rows, with the fit parameters displayed. The vertical lines shown are from the event selection criteria. The results of the sideband subtraction along with the associated statistical uncertainty are shown in the figures in the bottom row.

4.3.4 Simulated background processes for the decay channel $\gamma p \rightarrow \mathbf{K}^0\Sigma^+ \rightarrow n\pi^+\pi^+\pi^-$

The experimental data for the $\Sigma^+ \rightarrow n\pi^+$ decay channel show a large background in the MM($\pi^+\pi^- X$) under the Σ^+ peak(cf. Fig. 4.13). Thus it is important to study potential sources of background to assure that the sideband subtraction is also justified for this data set.

4.3.4.1 $\gamma p \rightarrow n\pi^+\pi^+\pi^-$ phase space distribution

$\gamma p \rightarrow n\pi^+\pi^+\pi^-$ events were generated with a flat distribution in the four particle phase space. The threshold for this reaction is 0.506 GeV so we expect background from this reaction throughout the data set. The top plots in Fig. 4.25 show MM($\pi^+\pi^+\pi^- X$) for this simulated data set background peaking around the mass of the neutron, so many of these events will pass the first cut on MM($\pi^+\pi^+\pi^- X$). The middle plots in Fig. 4.25 show results from M($\pi^+\pi^-$) for the $n\pi^+\pi^+\pi^-$ simulated data with a mostly flat background. The bottom plots in Fig. 4.25 show MM($\pi^+\pi^- X$) for these simulated data; the data points with error bars represent sideband events. As with the $\Sigma^+ \rightarrow p\pi^0$ decay channel, the background data points are consistent with the selected events. The number of events remaining after sideband subtraction and the associated statistical uncertainty are shown in each plot in the bottom row. These data show that the background events are removed by this procedure.

4.3.4.2 $\gamma p \rightarrow \Delta^+\rho^0 \rightarrow$ (n π^+) ($\pi^+\pi^-$) decay channel

Events from the reaction $\gamma p \rightarrow \Delta^+\rho^0 \rightarrow$ (n π^+) ($\pi^+\pi^-$) were also simulated and analyzed. The threshold for this reaction is 1.703 GeV so we might expect background from this reaction in the higher photon energy ranges in the data set, but here again the large width of the Δ and ρ make the 'below-threshold' contributions not only possible but larger than those in the higher photon energy bins. In Fig. 4.26, the MM($\pi^+\pi^+\pi^- X$) plot shows these events have a peak at the mass of the neutron. Figure 4.26 shows that here too, the sideband subtraction excludes most of these events from reaching the final event sample.

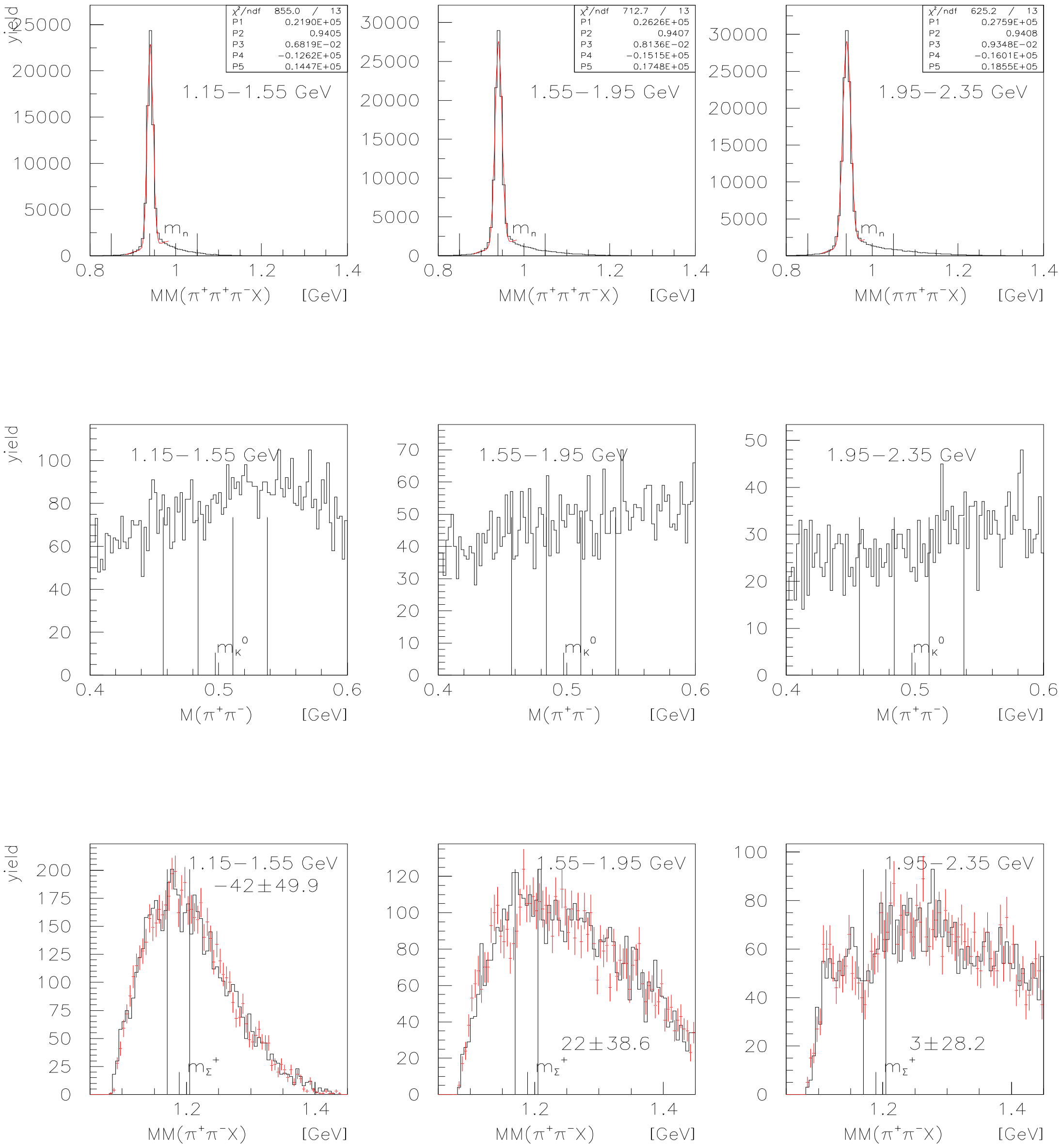

Figure 4.25: The top plots show MM($\pi^+\pi^+\pi^- X$) for three photon energy bins for $0.0 < \cos(\theta^{cm}_{(\pi^+\pi^-)}) < 0.2$ for simulated $\gamma p \rightarrow n\pi^+\pi^+\pi^-$ events. The middle and bottom plots show M($\pi^+\pi^-$) and MM($\pi^+\pi^- X$) using the same photon energy and angle bins. Gaussian fits are made in the top row, with the fit parameters displayed. The vertical lines shown are from the event selection criteria. The results of the sideband subtraction along with the associated statistical uncertainty are shown in the figures in the bottom row.

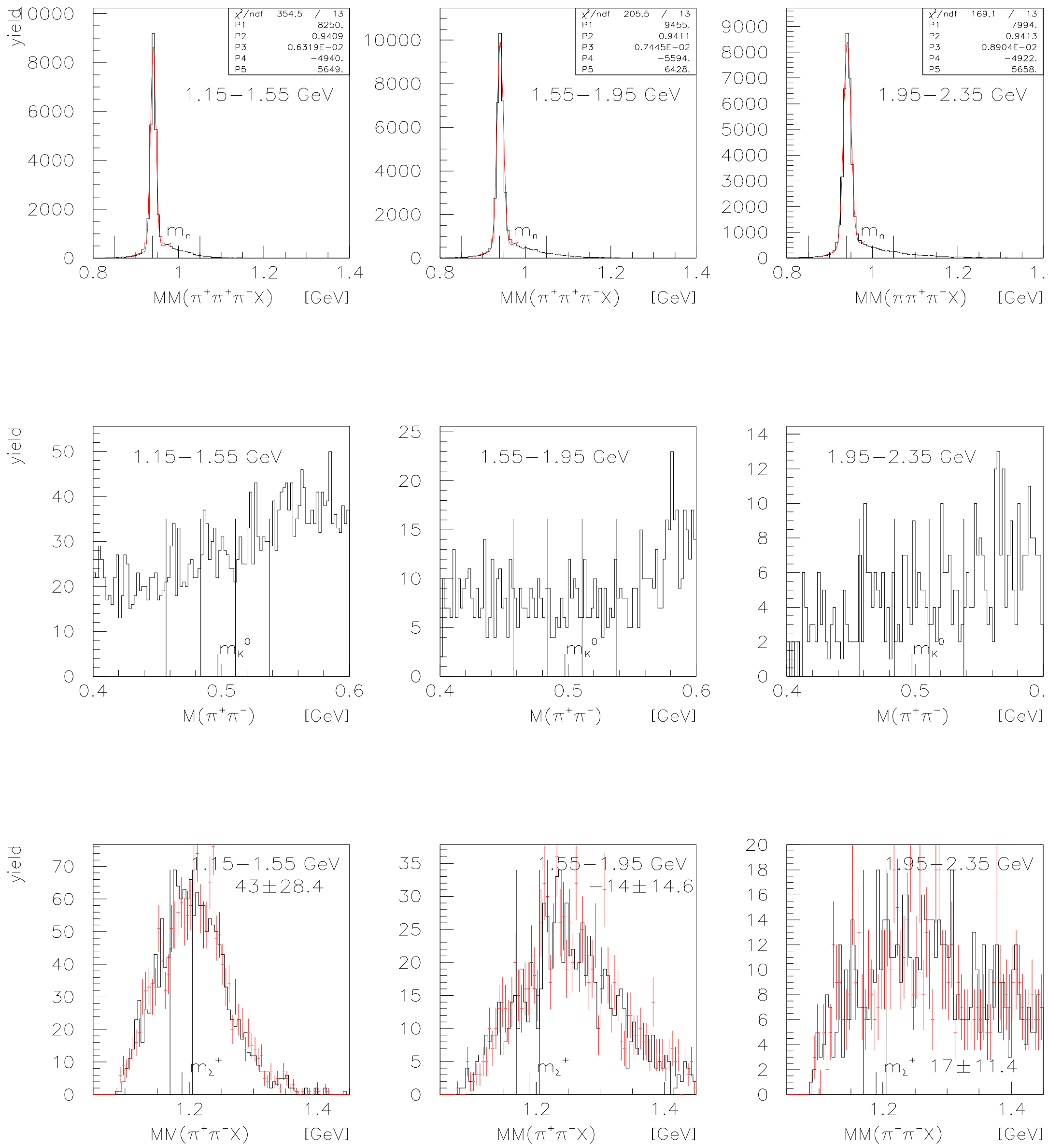

Figure 4.26: The top plots show MM($\pi^+\pi^+\pi^- X$) for three photon energy bins for $0.0 <$ $\cos(\theta^{cm}_{(\pi^+\pi^-)}) < 0.2$ for simulated $\gamma p \rightarrow \Delta^+ \rho^0 \rightarrow n\pi^+\pi^+\pi^-$ events. The middle and bottom plots show M($\pi^+\pi^-$) and MM($\pi^+\pi^- X$) using the same photon energy and angle bins. Gaussian fits are made in the top row, with the fit parameters displayed. The vertical lines shown are from the event selection criteria. The results of the sideband subtraction along with the associated statistical uncertainty are shown in the figures in the bottom row.

4.3.4.3 Comparison of simulated processes with experimental data

To compare these results with experimental data, first a comparison between experimental results and those for each simulated process is made.

In order to perform a more realistic yield extraction as for the $\Sigma^+ \rightarrow p\pi^0$ decay channel, events from the simulated processes in this section, $\gamma p \rightarrow \mathrm{K}^0\Sigma^+$, $n\pi^+\pi^+\pi^-$ and $\Delta^+\ \rho^0$ were combined and analyzed. Data were combined based on the measured cross section for $\gamma p \rightarrow n\pi^+\pi^+\pi^-$. Since the cross section for $\gamma p \rightarrow \Delta^+\ \rho^0$ is not well known, this cross section was adjusted to fit the distribution of experimental data. Figure 4.27 shows results for $\mathrm{MM}(\pi^+\pi^-X)$ with the combination of these reactions in the indicated bins.

This figure can be directly compared with Fig. 4.13 which contains the same plots for experimental data. The combination of the backgrounds appears similar to the experimental data. In both simulated and experimental data there is a high background in the photon energy bin 1.15-1.35 GeV which decreases to zero at about 1.35 GeV in $\mathrm{MM}(\pi^+\pi^-X)$. The background in the simulated and experimental data appear to exhibit similar properties in $\mathrm{MM}(\pi^+\pi^-X)$ in these photon energy bins. From this we conclude that the background processes that were identified and simulated explain well properties of the background in experimental data.

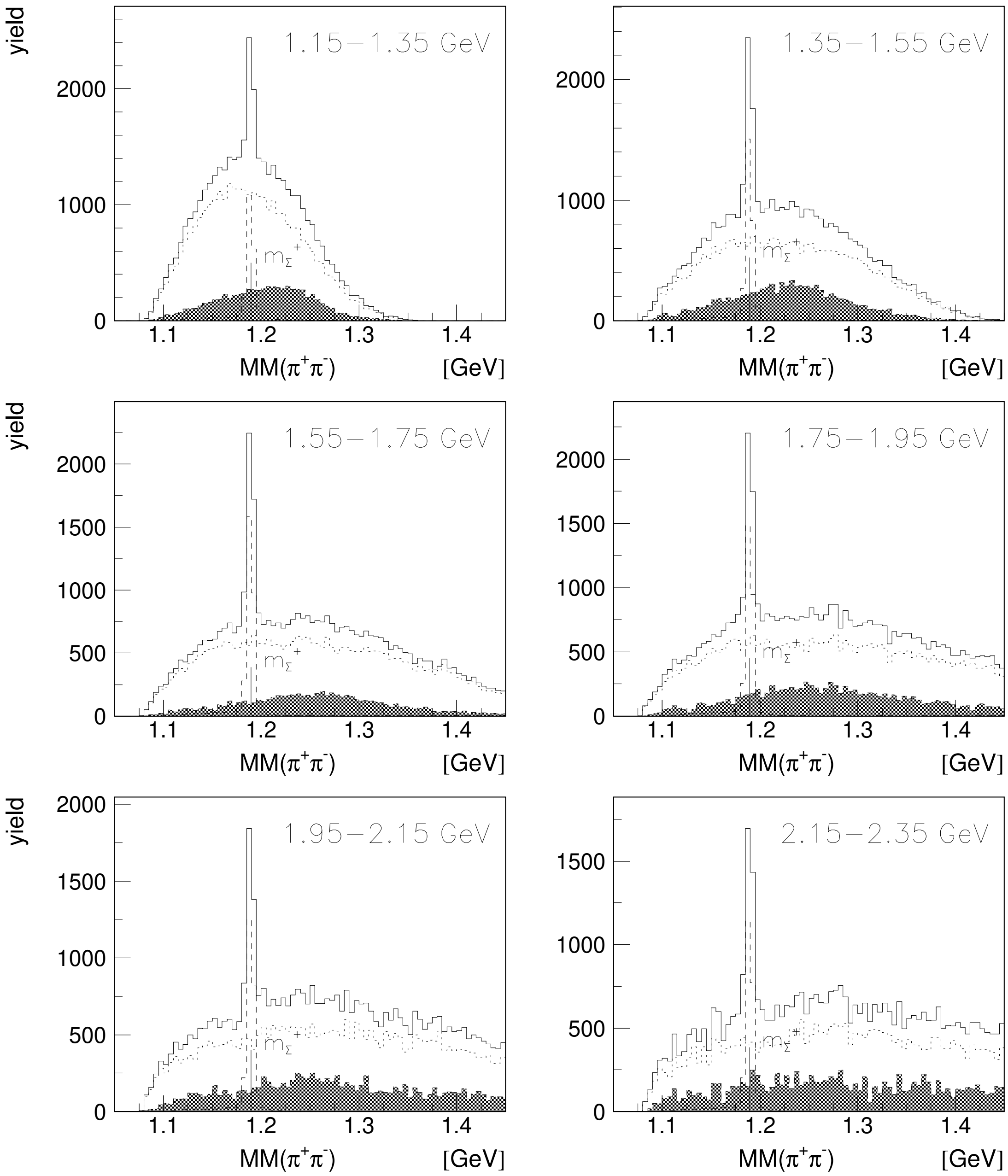

Figure 4.27: MM($\pi^+\pi^-X$) for the combined simulated processes analyzed for the $\Sigma^+ \to p\pi^0$ decay channel for all angles in six photon energy bins. The dashed line is for $K^0\Sigma^+$, the dotted line is for $\gamma p \to p\omega \to n\pi^+\pi^+\pi^-$, the filled in region is for $\gamma p \to \Delta^+ \rho^0 \to p\pi^+\pi^-\pi^0$. The solid line shows the sum of these processes.

Table 4.5 presents the number of events from each simulated background process that passed the event selection criteria into the final event sample(FES) for identified Σ^+ events. The second column on the table presents the scaling factor for each reaction which was used to combine the processes in Fig. 4.27 based on the number of events generated and the cross sections of the reactions. The number of events for the reaction is multiplied by this scaling factor, and then divided by the number of $\gamma p \to \mathrm{K}^0\Sigma^+$ events for the photon energy to determine the % of misidentified $\gamma p \to \mathrm{K}^0\Sigma^+$ events, as presented in the third column. As was the case for the $\Sigma^+ \to p\pi^0$ decay channel, the number of background events that are misidentified as $\gamma p \to \mathrm{K}^0\Sigma^+$ events in our final event sample is very small, with the highest total background contamination being 3.6% in the photon energy bin 1.95-2.35 GeV. Therefore, our sideband background subtraction is very efficient in eliminating background processes from our final event sample for the $\Sigma^+ \to n\pi^+$ decay channel as well as for the $\Sigma^+ \to p\pi^0$ decay channel.

Table 4.5: Final event samples and contamination percentages from background processes for the decay channel $\Sigma^+ \to n\pi^+$.

1.15-1.55 GeV	FES	Scale	% background contamination
$\gamma p \to \mathrm{K}^0\Sigma^+$	3451 ± 64		
$\gamma p \to n\pi^+\pi^+\pi^-$	-42 ± 50	1.8	0.4%
$\gamma p \to \Delta^+ \rho^0$	43 ± 28	1.0	2.1%
1.55-1.95 GeV			
$\gamma p \to \mathrm{K}^0\Sigma^+$	4762 ± 74		
$\gamma p \to n\pi^+\pi^+\pi^-$	22 ± 39	2.6	3.3%
$\gamma p \to \Delta^+ \rho^0$	-14 ± 15	1.8	0.1%
1.95-2.35 GeV			
$\gamma p \to \mathrm{K}^0\Sigma^+$	5491 ± 79		
$\gamma p \to n\pi^+\pi^+\pi^-$	3 ± 28	3.3	1.9%
$\gamma p \to \Delta^+ \rho^0$	17 ± 11	3.3	1.7%

4.4 Error analysis

4.4.1 Error propagation

The uncertainty in the determined cross sections takes into account uncertainties in the number of extracted events, acceptance, target density and photon flux. The statistical uncertainties in the number of events are calculated as the square root of the number of events. To obtain the final data sample, the sideband events are subtracted from the selected events. To propagate the errors for both decay channels the formula for error propagation of added or subtracted uncorrelated quantities is used:

$$\Delta S = \sqrt{\Delta A^2 + \frac{\Delta B^2}{4}} \tag{4.6}$$

where $S = A - \frac{B}{2}$, A is the number of selected events and B is the number of sideband events in a given bin in angle and energy.

The cross section (Eq. 4.1) is obtained by dividing the extracted number of Σ^+ events by the target density(T), the acceptance(ϵ) and the photon flux(Φ). The acceptance for a given energy and angular bin is determined by the number of events accepted by the analysis divided by the number of events generated. The uncertainty in the acceptance is determined from these quantities where the error on selected events is determined using binomial statistics, since the number of events accepted is a subset of the number of events generated, but the calculation is made more complicated by the sideband subtraction. The error in the acceptance is determined by the formula:

$$(\Delta A)^2 = \Delta\left(\frac{a-s}{a+r}\right)^2 = \frac{1}{(a+r)^4}[(r^2+s^2)a + (a^2+s^2)r + \frac{1}{2}(a+r)^2 s] \ , \tag{4.7}$$

where a is the number of events accepted in the selected region, r is the number of events rejected, i.e. outside the selected region, and s is half the number of events in the two sidebands.

The errors for the photon flux values were provided to us as a result of the gflux program.

The differential cross section is calculated from the $\gamma p \to \mathrm{K}^0\Sigma^+ \to p\pi^+\pi^-\pi^0$ and the $\gamma p \to \mathrm{K}^0\Sigma^+ \to n\pi^+\pi^+\pi^-$ partial differential cross sections by adding them together and dividing by the $K^0_S \to \pi^0\pi^0$ and missing K^0_L branching ratio. The formula for the cross section is given by:

$$\frac{d\sigma}{d\Omega} = \frac{N}{(\Phi T \epsilon \Omega B)} \ . \tag{4.8}$$

Thus we can write the error in the differential cross section as:

$$\Delta\sigma = \sigma * \sqrt{\left(\frac{\Delta S}{S}\right)^2 + \left(\frac{\Delta T}{T}\right)^2 + \left(\frac{\Delta \Phi}{\Phi}\right)^2 + \left(\frac{\Delta \epsilon}{\epsilon}\right)^2 + \left(\frac{\Delta B}{B}\right)^2} \ . \tag{4.9}$$

Table 4.6 shows the uncertainties (for the $\Sigma^+ \to p\pi^0$ decay channel in the photon energy bin 1.55 to 1.75 GeV and the angular bin $0.0 < \cos(\theta^{cm}_{K^0_S}) < 0.2$) for the quantities used to calculate the partial differential cross section and the uncertainty in the partial differential cross section. The majority of the error in the differential cross section comes from the statistical error in the number of the selected events from this analysis. This is due to the relatively low number of selected events present, and that experiments which would generate more selected events would clearly reduce this error. As the statistical uncertainty mainly comes from the number of selected events, we studied alternate methods of obtaining these numbers to determine systematic uncertainties in Section 4.4.2.

Table 4.6: Error propagation for one bin of the differential cross section

	Quantity	Uncertainty	Percentage Error
Acceptance	0.1210	0.0014	1.2%
Photon Flux (no. of γs)	$3.02\text{x}10^{11}$	$9.06\text{X}10^{9}$	3.0%
Target Parameter ($\frac{g}{cm^3}$)	$7.58\text{X}10^{-7}$	$3.6\text{X}10^{-9}$	0.5%
Branching Ratio	0.177	0.001	0.7%
Selected Events (no. of events)	302.5	37.4	12.4%
Total Uncertainty ($\frac{\mu b}{sr}$)	0.0491	0.0061	12.4%

It can be seen that the uncertainty in the number of selected events dominates the total uncertainty. Thus it is important to consider effects which might systematically bias the selection.

4.4.2 Systematic uncertainties

In addition to the statistical uncertainties in the results, systematic uncertainties which are present in the analysis must be considered.

4.4.2.1 Sideband background subtraction

To determine systematic uncertainties in the method used to obtain the final event sample, different methods for obtaining this final event sample were peformed and compared with our chosen method. Comparisons of values of these alternate final event samples with our chosen one were made in six photon energy bins of 200 MeV each, and eight points in $\cos(\theta^{cm}_{K^0_S})$. A χ^2 value was calculated for each comparison using the equation

$$\chi^2 = \sum_{i=1}^{8} \left[\frac{(a_1 - a_2)^2}{\sigma_1^2 + \sigma_2^2} \right]_i = \sum_{i=1}^{8} \left[\frac{(a_1 - a)^2}{\sigma_1^2} + \frac{(a_2 - a)^2}{\sigma_2^2} \right]_i \tag{4.10}$$

where a_1 and a_2 are elements of two different data sets, where we expect to obtain the same result (a) independently from each set. A Z value was also calculated for these comparisons, where

$$Z = \sum_{i=1}^{8} \left[\frac{(a_1 - a_2)}{\sqrt{\sigma_1^2 + \sigma_2^2}} \right]_i . \tag{4.11}$$

Table 4.7 presents results of comparisons between the chosen analysis method of extracting Σ^+ events and alternate methods, showing the χ^2 and Z parameters for eight degrees of freedom. The full sets of final event samples being considered are presented in Appendix C. If the variations are normally distributed and independent, χ^2 should be approximately the number of data pairs, and $|Z|$ (the absolute value of Z) should be approximately the square root of the number of data pairs. The systematic uncertainty for a given bin is calculated by dividing $|Z|$ by the number of data points in the bin (in most cases 8 data points) and then multiplying by the statistical error in that bin. For the eight data points considered, values of Z that contribute more than half of the total Z value for the set are rejected. For calculating the statistical error, data points with greater than 100% statistical error were also rejected, as these points do not represent the data as a whole and would improperly skew the results. It is clear that the data sets being compared in the sideband subtraction comparison are not independent, as the data in the middle 7 bins will be present in both the 7 bin and

9 bin data sets. Therefore, the χ^2 values will be smaller than would be for two sets of independent data.

Table 4.7: Determining systematic uncertainties for sideband subtraction method of identifying Σ^+ events. The χ^2 (all presented as χ^2 per eight degrees of freedom) and Z parameters for eight degrees of freedom are presented. The * represents the "standard" method we have chosen to use in this analysis. The signs of the Z parameters come from by subtracting the alternate methods from the method chosen for this analysis.

	9bins v. 7bins(*)			gap v. no gap(*)			fit v. sum (*)			
E_γ (GeV)	χ^2	Z	syst.err	χ^2	Z	syst.err	χ^2	Z	syst.err	stat.err.
$\Sigma^+ \to p\pi^0$										
1.15-1.35	2.45	-3.41	11.5%	1.14	-2.37	8.0%	3.69	3.70	12.5 %	27.0 %
1.35-1.55	0.80	-0.19	0.3%	1.43	-2.15	3.8%	0.71	-1.38	2.5%	14.3 %
1.55-1.75	1.12	-1.88	3.4%	1.54	-2.02	3.7 %	0.58	-0.91	1.6 %	14.6 %
1.75-1.95	0.66	-0.66	1.9%	0.46	-0.64	1.8%	1.66	-2.37	6.7 %	22.5 %
1.95-2.15	0.89	-1.14	4.1%	0.38	-0.05	0.4 %	3.79	1.48	5.3%	28.8 %
2.15-2.35	1.23	-1.31	4.6%	0.73	-0.74	2.6 %	11.24	4.34	4.7 %	27.8 %
$\Sigma^+ \to n\pi^+$										
1.15-1.35	1.31	-0.69	3.2%	1.34	-2.46	11.3 %	2.75	-2.03	9.4%	36.9 %
1.35-1.55	0.75	-1.75	4.3%	0.59	-0.93	2.3 %	0.99	0.32	0.8%	19.6 %
1.55-1.75	0.95	0.13	0.2%	0.28	-0.82	1.5 %	2.37	2.38	2.4%	14.4 %
1.75-1.95	0.24	0.05	0.1%	0.14	-3.71	1.4 %	4.55	-0.62	1.2%	15.8 %
1.95-2.15	1.22	-1.93	4.2%	0.11	-0.17	0.4 %	0.76	0.71	1.6%	17.5 %
2.15-2.35	0.91	0.16	0.4 %	0.78	-0.49	1.4 %	0.56	-0.68	1.9%	22.1 %

Summing over 7 central bins vs. 9 central bins in the Σ^+ plot In the analysis, the sideband subtracted events are summed in a region of seven bins of 0.05 MeV per bin around the mass of the Σ^+(1.189 GeV), from 1.17 to 1.205 GeV. For a comparison, the analysis was also performed summing over a region of nine bins of similar size around the mass of the Σ^+ , from 1.165 to 1.21 GeV. χ^2 and Z results for this comparison are presented in the first two columns of Table 4.7. The data sets being compared in the sideband subtraction comparison are not independent, as the data in the middle 7 bins will be present in both the 7 bin and 9 bin data sets. Therefore, the χ^2 values will be smaller than would be for two sets of independent data.

Contiguous vs. non-contiguous sidebands for subtraction For the sideband subtraction it is assumed that the events in the sidebands will accurately represent the shape of the background. For this analysis sideband regions were chosen to be contiguous with the region of selected events. To ensure that this method is accurate, and to check that the background will not vary greatly further from the selected region, a final event sample is obtained using sideband regions that were separated from the region of selected events by a gap equal to $\frac{1}{4}$ the size of the center selected region, as described in Section 4.4.2.1. χ^2 and Z results for this comparison with the chosen method are listed in the third and fourth columns of Table 4.7.

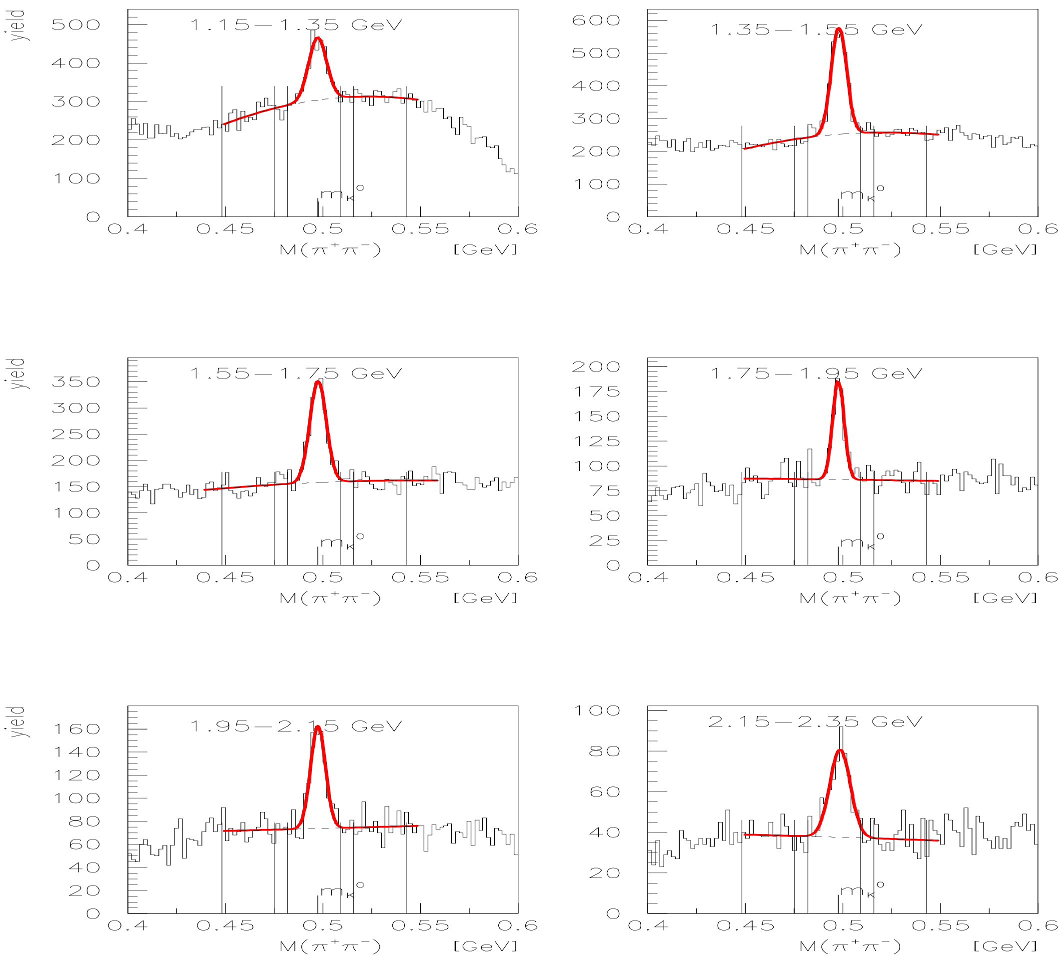

Figure 4.28: M($\pi^+\pi^-$)for the $\Sigma^+ \to p\pi^0$ decay channel. The center region contains selected events while the right and left sidebands are now separated from the selected region by gaps of $\frac{1}{4}$ the size of the selected region.

Sideband subtraction vs. fitted peak Another method of obtaining the final event sample is fitting the peak of selected events to a Gaussian and third-order polynomial. Figures 4.29 and 4.30 show comparisons of the sideband subtraction method, on the left, and fitting to a Gaussian and third-order polynomial, on the right. For events with comparatively high statistics, as in Fig. 4.29, the differences in the final event sample are small between the methods when the statistical errors are considered. For bins with lower statistics, as in Fig. 4.30, it is more difficult to obtain accurate fits, and the differences between the methods are larger, though still within the statistical errors. The errors for the extracted yields in Fig. 4.29 and 4.30 (right-hand sides) were calculated according to the equation

$$\Delta A^2 = \sqrt{2\pi}[(m\Delta\sigma)^2 + (\sigma\Delta m)^2]$$

where $A = \sqrt{2\pi}\sigma m$ is the area under the Gaussian, m its mean and σ its variation. χ^2 and Z results for this comparison are presented in the fifth and sixth columns of Table 4.7.

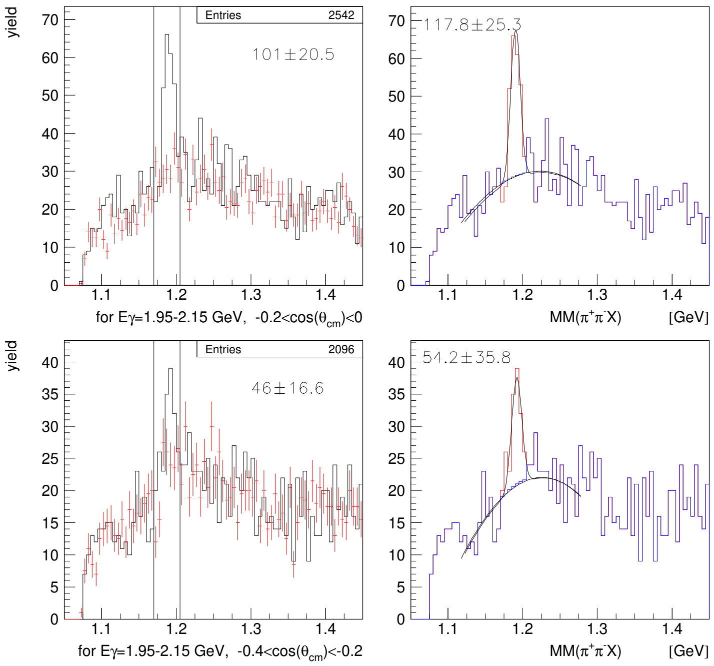

Figure 4.29: MM($\pi^+\pi^- X$)for $\Sigma^+ \to p\pi^0$. The sideband subtracted results are on the left and the corresponding fits are on the right.

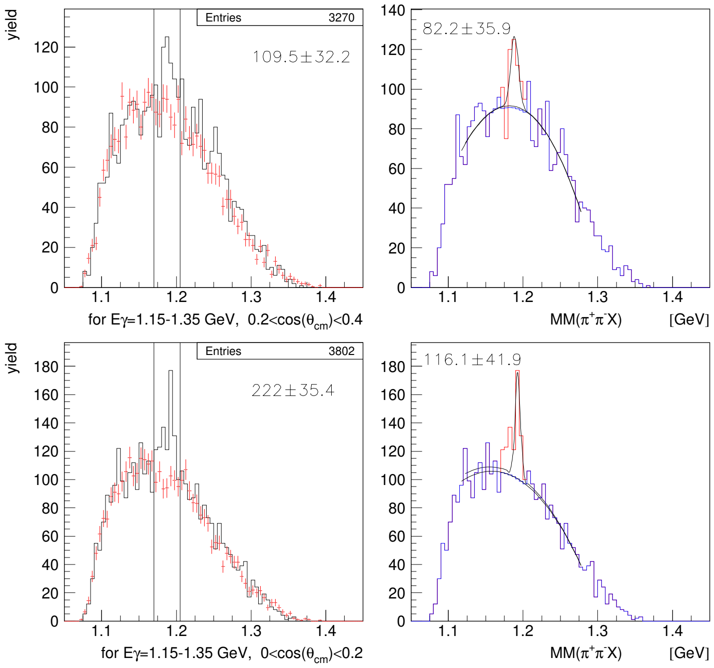

Figure 4.30: MM($\pi^+\pi^- X$)for $\Sigma^+ \to p\pi^0$. The sideband subtracted results are on the left and the corresponding fits are on the right.

4.4.2.2 The $\Sigma^+ \to p\pi^0$ vs. $\Sigma^+ \to n\pi^+$ decay channel

To check the quality of our data and analysis, results obtained from the decay channels $\Sigma^+ \to p\pi^0$ and $\Sigma^+ \to n\pi^+$ were analyzed separately. Results from each decay channel should give the same measured cross section. The cross sections extracted from both decay channels were compared, and Table 4.8 shows results of these comparisons. Based on the calculated Z value, systematic uncertainties were calculated for the 8 angle bins by multiplying the Z value by the fractional statistical error for each bin, then summing these results (taking the best 7 out of 8 points for the systematic error calculation so as to not have one point overly influencing the entire systematic error). This table shows that our systematic uncertainties are considerably smaller than statistical uncertainties. As these data sets have a total χ^2 of 43.8 for 48 degrees of freedom and $\sum Z \approx \sqrt{N}$ (in this case $\sqrt{48}$), there is no evidence for significant systematic uncertainties in this test.

Table 4.8: Comparisons of differential cross sections for the $\Sigma^+ \to p\pi^0$ versus the $\Sigma^+ \to n\pi^+$ decay channel. The signs of the Z parameters come from subtracting the $\Sigma^+ \to n\pi^+$ decay channel result from the $\Sigma^+ \to p\pi^0$ decay channel result.

Photon Energy	χ^2 per 8DF	Z	stat. error	systematic error
1.15-1.35 GeV	8.50	0.848	29.0 %	3.1%
1.35-1.55 GeV	6.00	-2.175	13.7%	3.8%
1.55-1.75 GeV	9.21	-3.229	14.1%	6.5 %
1.75-1.95 GeV	9.48	-1.587	24.7%	4.9%
1.95-2.15 GeV	4.58	-0.808	26.3%	2.7 %
2.15-2.35 GeV	0.48	-1.784	22.3%	5.0 %

4.4.2.3 2.445 vs. 3.115 GeV beam energy data

The final data set includes data from two running periods, each at a different electron beam energy. The acceptance corrected and flux normalized yield for both data sets should be the same. To compare the results from these two run periods, the data obtained from each running period were analyzed separately. As these data sets were only combined for photon energies of 1.55 GeV and above, four photon energy bins of 200 MeV each which contained values for eight regions of $\cos(\theta^{cm}_{K^0_S})$ were analyzed. A χ^2 and Z value for each region was obtained as before. Summing up these χ^2 values over each photon energy bin we obtained the results in Table 4.9. In the photon energy range from 1.55 to 2.35 GeV the two data sets appear to be consistent with each other, as the total χ^2 is 30.67 for 32 degrees of freedom. The Z values indicate that the 3.115 GeV data set cross sections are about 4.5% larger than the 2.445 GeV data set cross sections, well within statistical uncertainties.

Table 4.9: Comparisons of cross sections for the 2.445 versus the 3.115 GeV data set. The signs of the Z parameters come from subtracting the 3.115 GeV data set result from the 2.445 GeV data set result.

Photon Energy	χ^2	Z	stat error	syst err
1.55-1.75 GeV	8.37	-1.10	17.1%	2.4 %
1.75-1.95 GeV	4.20	-4.13	19.1%	9.9 %
1.95-2.15 GeV	13.97	-0.83	28.7%	3.0 %
2.15-2.35 GeV	4.13	-1.10	19.9%	2.7 %

4.4.2.4 Laboratory azimuthal angle of the K^0_S

Acceptance corrected-yields were analyzed in three angular regions of the laboratory azimuth(ϕ) of the K^0_S: -30° to 90° (range 1), 90° to 210° (range 2), and 210° to 330° (range 3). Each region corresponds to two sectors of CLAS. Since the azimuthal orientation of the $\gamma p \rightarrow K^0\Sigma^+$ production plane is equally probable for these three angular regions, the same results should be obtained for each set if the acceptance is correctly simulated. χ^2 results for the comparisons of these data sets are presented in Table 4.10, with the complete tables in Appendix C. The few high χ^2 values on this table mainly result from one or two points out of eight having a high χ^2 value. For example, for 1.15 GeV < E_γ < 1.35 GeV, the total χ^2 of 18.47 for comparing lab angles 2 and 3 mainly results from a χ^2 of 14.51 for 0.0 < $\cos(\theta^{cm}_{K^0_S})$< 0.2 . The total χ^2 of 18.32 for comparing lab angles 1 and 3 mainly results from a χ^2 value of 10.33 for 0.4 < $\cos(\theta^{cm}_{K^0_S})$< 0.6. As these high χ^2 values appear infrequently and in all comparisons of the data sets, it does not appear that the acceptance corrected yield for one range in lab angle is inconsistent with the other two. As most of these comparisons have good χ^2 values, there is no evidence of a significant ϕ-dependent systematic uncertainty.

Table 4.10: χ^2 values for comparing acceptance corrected yields for three different ranges in laboratory $\phi^{lab}_{K^0_S}$.

Photon Energy	χ^2 1 vs 2	χ^2 1 vs 3	χ^2 2 vs 3
1.15-1.35 GeV	18.47	10.29	7.69
1.35-1.55 GeV	6.69	18.32	19.69
1.55-1.75 GeV	3.24	4.06	3.81
1.75-1.95 GeV	4.95	7.22	5.64
1.95-2.15 GeV	6.42	3.00	3.80
2.15-2.35 GeV	5.38	8.35	8.61

Table 4.11: Z values and systematic errors for comparisons of acceptance corrected yields for three different ranges in laboratory $\phi^{lab}_{K^0_S}$. The Z values are calculated by subtracting results from lab angle regions 1 from 2, 1 from 3, and 2 from 3.

Photon Energy	Z 1 vs 2	syst. err	Z 1 vs 3	syst. err	Z 2 vs 3	syst. err
1.15-1.35 GeV	-0.99	6.9%	-3.98	31.4%	-1.31	7.5%
1.35-1.55 GeV	2.64	8.2%	3.07	9.5%	0.41	1.4%
1.55-1.75 GeV	1.20	6.0%	0.26	1.3%	-0.93	4.3%
1.75-1.95 GeV	-0.27	2.3%	0.58	4.8%	0.83	4.5%
1.95-2.15 GeV	-0.57	3.7%	-2.24	14.7%	-1.81	10.6%
2.15-2.35 GeV	0.33	2.1%	0.78	4.9%	0.33	2.2%

4.4.2.5 Other systematic errors

The systematic error for the gflux procedure of photon normalization has been estimated to be about 3%. Systematic uncertainties also enter from the target parameters, which are estimated to be about 0.4% from the measurement of the target density and 0.3% from the measurement of the target length [35].

4.4.2.6 Systematic error results

Table 4.12 shows combined results from this section for systematic errors from various studies. The overall systematic uncertainty is determined by adding these systematic errors in quadrature, in the form

$$\Delta S = \sqrt{(\Delta S_1)^2 + (\Delta S_2)^2 + (\Delta S_3)^2 + ... + (\Delta S_N)^2}\ .$$

The systematic uncertainty from the sideband subtraction comparisons in Section 4.4.2.1 gives the largest contribution to the overall systematic uncertainty in most energy bins.

Table 4.12: Summary of systematic uncertainties. The systematic errors for the event selection come from the sideband subtraction studies in Section 4.4.2.1. The systematic uncertainties from the acceptance use the highest values for systematic error for the three comparisons presented in Section 4.4.2.4 (exluding the systematic error of 31% which is uncharacteristically high). The decay channel systematic errors come from comparing the $\Sigma^+ \to p\pi^0$ and $\Sigma^+ \to n\pi^+$ decay channels, as presented in Section 4.4.2.2. The beam energy systematic errors come from comparing results for the 2.445 and 3.115 GeV beam energy data sets as presented in Section 4.4.2.3. The systematic errors in the target parameters and gflux are presented in Section 4.4.2.5. The overall systematic error is calculated by adding these systematic errors in quadrature.

Photon Energy	event sel.	ϕ acc.	decay channel	E_{beam}	overall syst.err
1.15-1.35 GeV	12.5%	7.5%	3.1%		15.2%
1.35-1.55 GeV	4.3%	9.5%	3.8%		10.9%
1.55-1.75 GeV	3.7%	6.0%	6.5%	2.4%	10.3%
1.75-1.95 GeV	6.7%	4.8%	4.9%	9.9%	14.1%
1.95-2.15 GeV	5.3%	14.7%	2.7%	3.0%	16.4%
2.15-2.35 GeV	4.7%	4.9%	5.0%	2.7%	9.4%
	common syst. errors:		target: 0.5%;		photon flux: 3.0%

Chapter 5

Physics results

5.1 Differential cross section

As stated at the beginning of Section 4, the differential cross section for a given angle and energy bin is obtained via the equation

$$\frac{d\sigma}{d\Omega} = \frac{N}{(\Phi T \epsilon \Omega B)} \tag{5.1}$$

where N is the number of extracted events obtained through this analysis, Φ is the number of photons obtained through gflux (from Section 3.7.1), $\epsilon\Omega$ is the solid angle times the acceptance, T is the target proton density per unit area, and B is the product of branching ratios for the detected final state. For the two analyzed states, $\Sigma^+ \to p\pi^0$ and $\Sigma^+ \to n\pi^+$, we have B($\gamma p \to$K$^0\Sigma^+ \to$ $(\pi^+\pi^-)(p\ \pi^0)$) = (0.5)(0.686 $\pm$ 0.003)(0.516 $\pm$ 0.003) = 0.177 and B($\gamma p \to$K$^0\Sigma^+ \to$ $(\pi^+\pi^-)(n\ \pi^+)$) = (0.5)(0.686 $\pm$ 0.003)(0.483 $\pm$ 0.003) = 0.167, where the three factors are the ratios for K^0 being K^0_S , $K^0_S \to \pi^+\pi^-$, and $\Sigma^+ \to p\pi^0$ or $\Sigma^+ \to n\pi^+$ respectively. Partial differential cross sections are calculated for both analyzed decay channels, $\Sigma^+ \to p\pi^0$ and $\Sigma^+ \to n\pi^+$, and added together.

To obtain the final results, differential cross sections are separately calculated for the 2.445 GeV beam energy data set and the combination of the 3.115 GeV beam energy data sets, one with full tagger enabled and one with half tagger enabled. The 3.115 GeV data set was deemed usable only for photon energies above 1.55 GeV, so the data below 1.55 GeV are taken solely from the 2.445 GeV data set. A weighted average of these results is taken in a given bin in angle and energy to obtain the final results, shown in Fig. 5.1. This figure shows the differential cross sections in 6 different photon energy bins of 200 MeV each, each broken up into 8 angular bins in $\cos(\theta^{cm}_{K^0_S})$ of 0.2 each, between -0.8 and 0.8. Angular bins outside this range are not analyzed, as the data were too few in those bins to obtain sufficient statistics to extract events for the final event sample.

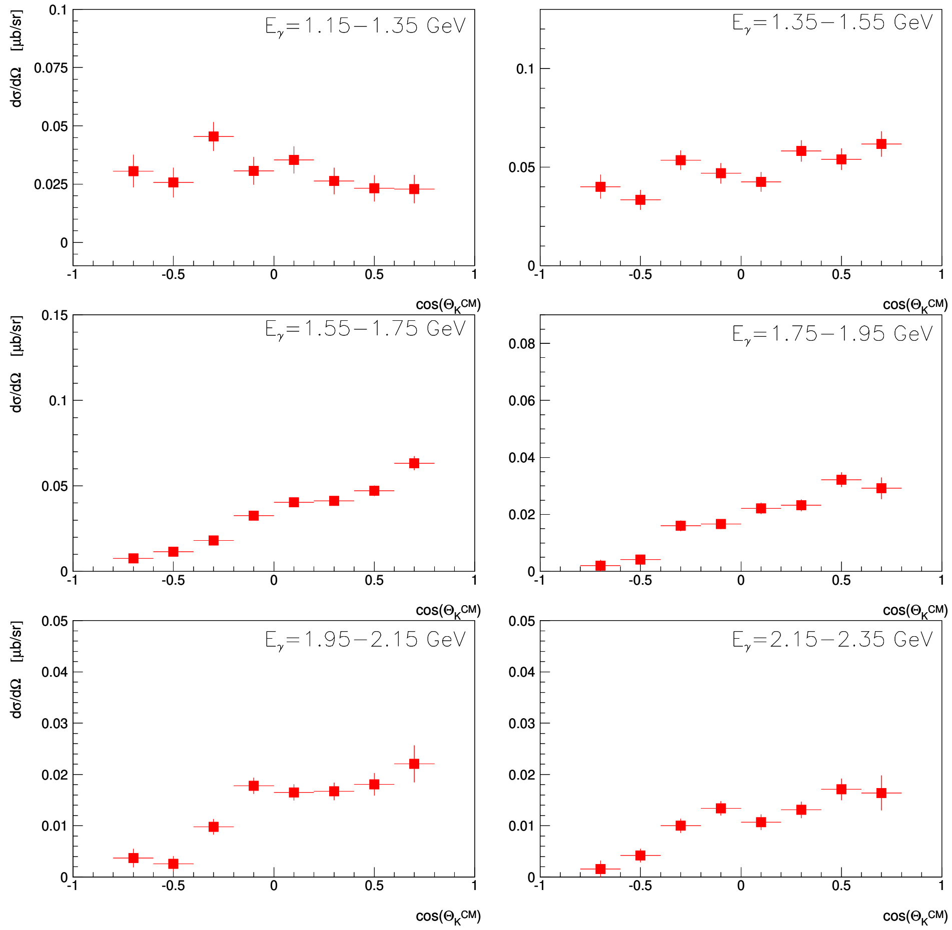

Figure 5.1: Differential cross section for -0.8 < $\cos(\theta^{cm}_{K^0_S})$ < 0.8 for $\gamma p \rightarrow K^0\Sigma^+$ for CLAS data, combining all data sets (both decay channels and beam energies). The vertical error bars are due to counting statistics, the horizontal bars represent the energy interval over which the data are summed.

Figures 5.2 and 5.3 show results obtained for the differential cross section determined separately from the data for the $\Sigma^+ \to p\pi^0$ and $\Sigma^+ \to n\pi^+$ decay channels, from separate analyses of the 2.445 GeV data, the 3.115 GeV data with the full tagger enabled, and the 3.115 GeV data with half of the tagger enabled. The results were scaled using the correct branching ratios.

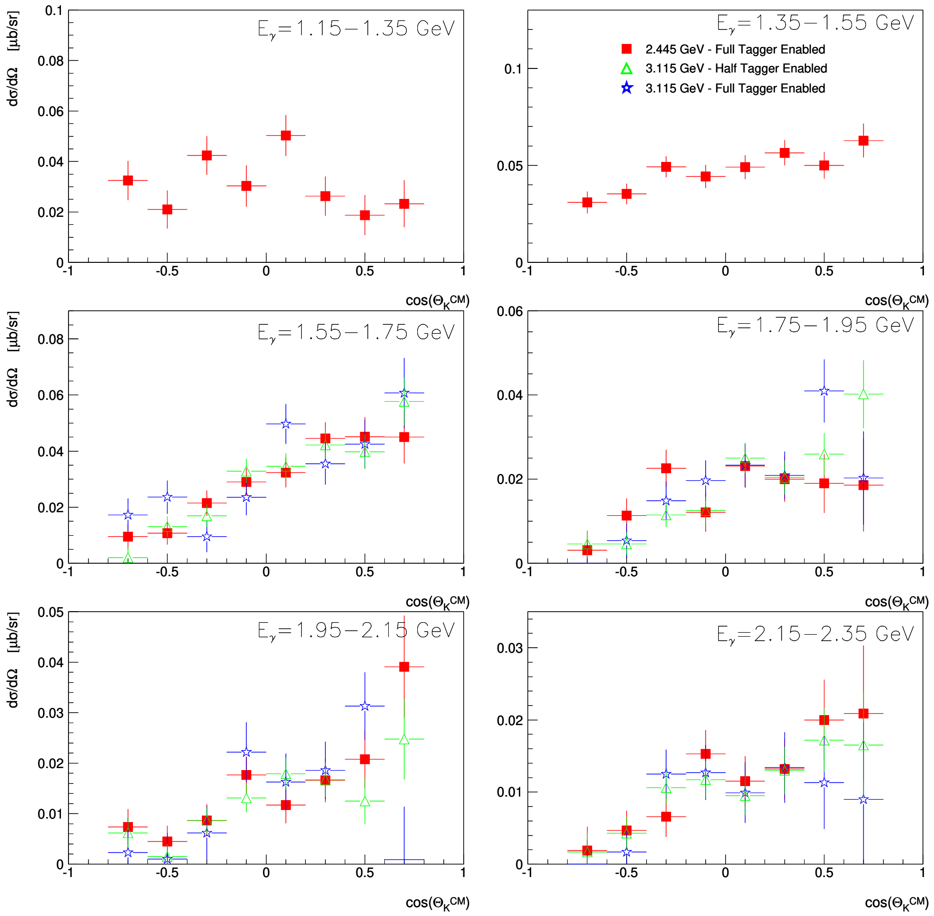

Figure 5.2: Differential cross section for $\gamma p \to \mathrm{K}^0\Sigma^+$ from three subsets of the g1c data using the $\Sigma^+ \to p\pi^0$ decay channel data. The solid squares are the 2.4 GeV data points, the open squares are for 3.1 GeV data with half of the tagger not active, and the open stars are for 3.1 GeV data with the full tagger active. The vertical error bars are due to counting statistics, the horizontal bars represent the energy interval over which the data are summed.

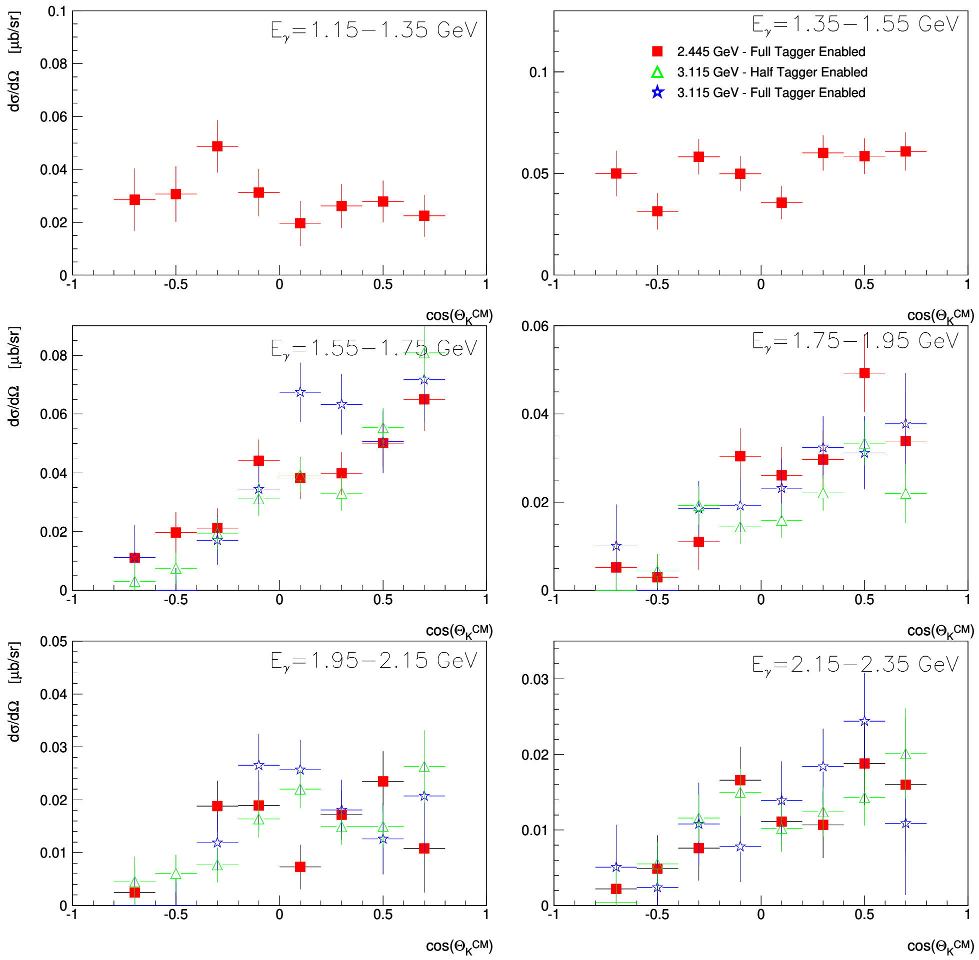

Figure 5.3: Differential cross section from $\gamma p \rightarrow K^0\Sigma^+$ using three subsets of the g1c data from the $\Sigma^+ \rightarrow n\pi^+$ decay channel data. The solid squares are the 2.4 GeV data points, the open squares are for 3.1 GeV data with half of the tagger not active, and the open stars are for 3.1 GeV data with the full tagger active. The vertical error bars are due to counting statistics, the horizontal bars represent the energy interval over which the data are summed.

5.2 Integrated cross section and extrapolated total cross section

To obtain the integrated cross section, the data were rebinned in photon energy bins of 100 MeV and angular range of 0.4 in $\cos(\theta^{cm}_{K^0_S})$. For a given photon energy bin, the differential cross section data points are summed and multiplied by 2π to account for the integral over the azimuthal angle and by 0.4 for the bin size in $\cos(\theta^{cm}_{K^0_S})$, which is written as

$$\sigma = \int_{-0.8}^{0.8}\int_{0}^{2\pi}\frac{d\sigma}{d\Omega}d(cos\theta)d\phi = \sum_{i=1}^{4}(\frac{d\sigma}{d\Omega})_i 2\pi\Delta(\cos(\theta^{cm}_{K^0_S}))_i \ . \tag{5.2}$$

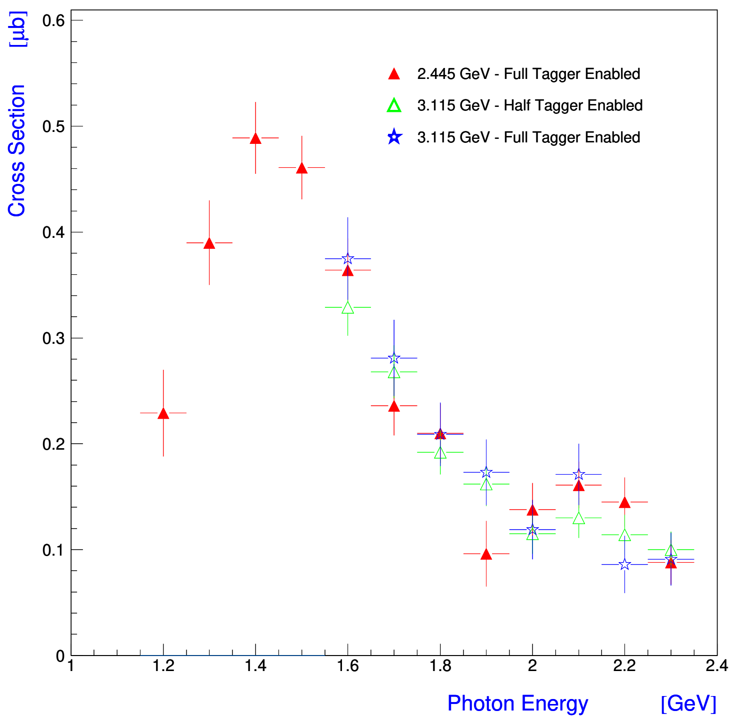

Figure 5.4: Integrated cross section for -0.8 < $\cos(\theta^{cm}_{K^0_S})$ < 0.8 for $\gamma p \rightarrow K^0\Sigma^+$ from three subsets of the data using the $\Sigma^+ \rightarrow p\pi^0$ decay channel. The vertical error bars are due to counting statistics, the horizontal bars represent the angle interval over which the data are summed.

Figures 5.4 and 5.5 show results obtained for the integrated cross section separately from data for the $\Sigma^+ \to p\pi^0$ and $\Sigma^+ \to n\pi^+$ decay channels respectively, from separate analyses of the 2.445 GeV data, the 3.115 GeV data with the full tagger enabled, and the 3.115 GeV data with half of the tagger enabled. The results were scaled using the correct branching ratios. These figures show that the results agree within the error bars.

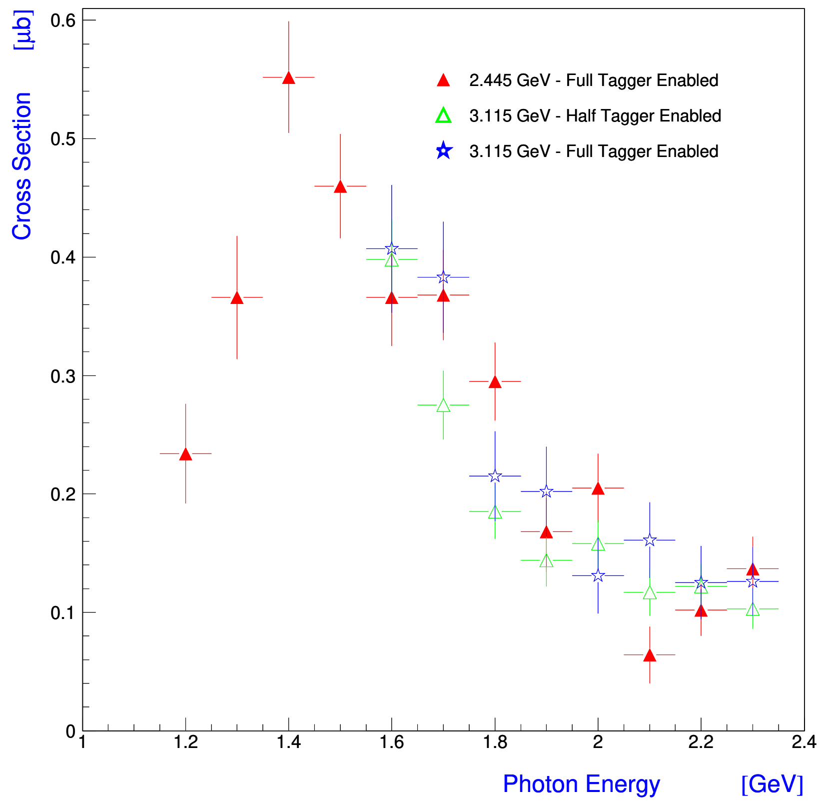

Figure 5.5: Integrated cross section for -0.8 $< \cos(\theta^{cm}_{K^0_S}) <$ 0.8 for $\gamma p \to \mathrm{K}^0\Sigma^+$ from three subsets of the data using the $\Sigma^+ \to n\pi^+$ decay channel. The vertical error bars are due to counting statistics, the horizontal bars represent the angle interval over which the data are summed.

As data were only analyzed in the angle range from -0.8 < $\cos(\theta^{cm}_{K^0_S})$< 0.8, an extrapolation must be performed for the missing angle range to obtain the total cross section. To approximate the differential cross section outside the range of measurement, the measured differential cross section in each of the six photon energy ranges is fit to a straight line. An extrapolation of this line is used to obtain an estimate of the cross section in the unmeasured angular region. These fits and extrapolated points are shown in Fig. 5.6.

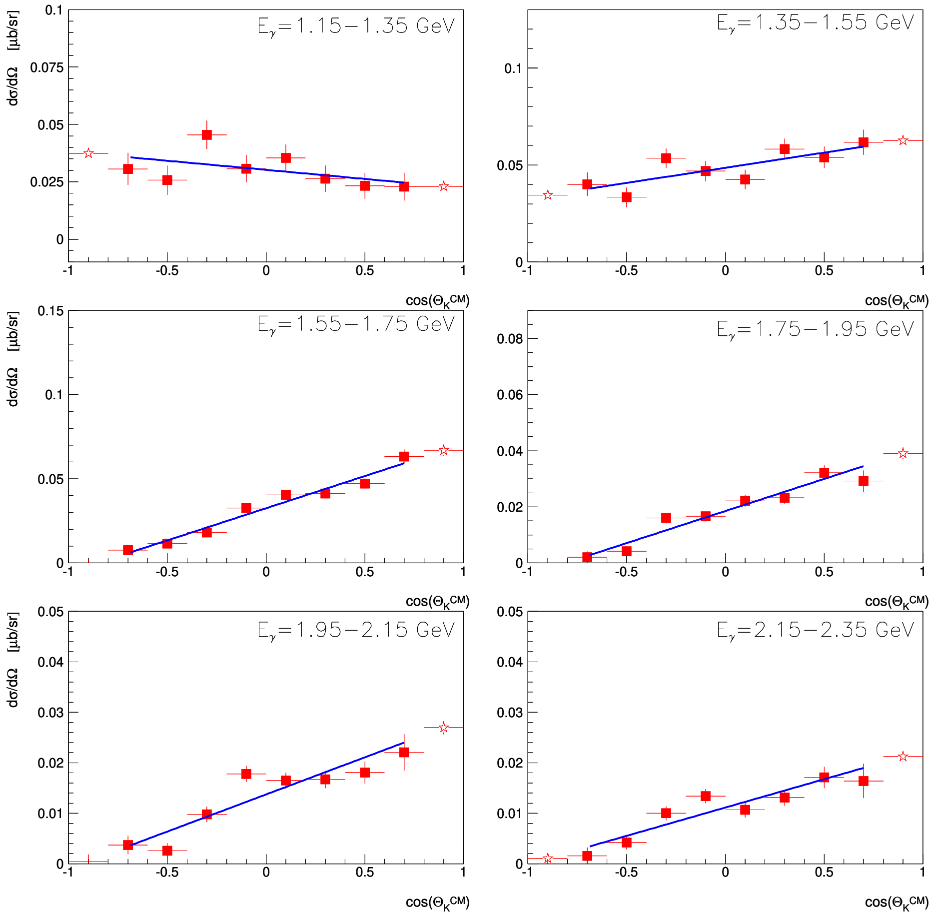

Figure 5.6: Straight line fits to differential cross section data used to extrapolate values in the missing angular regions. The measured differential cross sections are represented by solid squares, while the estimated values at $\cos(\theta^{cm}_{K^0_S})$ = ± 0.9 are represented by stars. Negative values obtained in these extrapolations are taken as zero in obtaining the total cross sections.

This straight line fit was performed for photon energy bins of 200 MeV, as that wide a bin was required to have adequate statistics for the data points. These extrapolated points obtained from the 200 MeV energy bin straight line fits were then interpolated linearly for values in 100 MeV bins of photon energy. In Fig. 5.7 cross sections are plotted for the integrated cross section in the range of -0.8 $< \cos(\theta^{cm}_{K^0_S}) <$ 0.8, and the extrapolated total cross section.

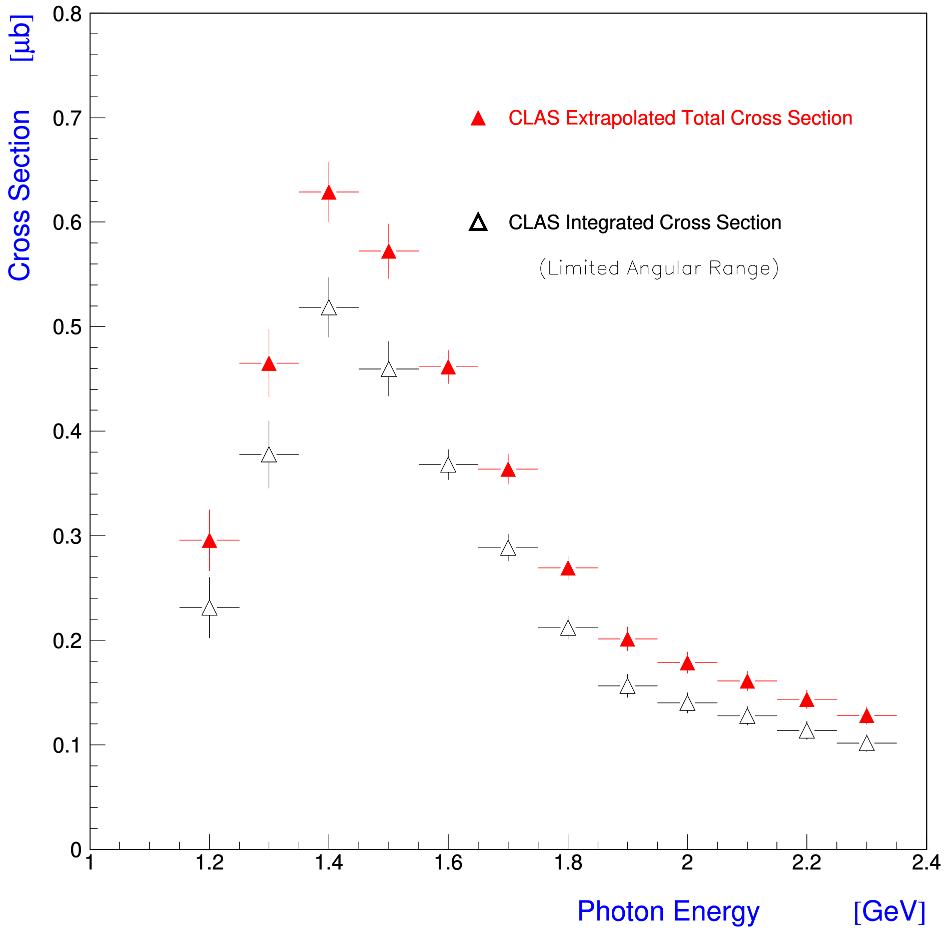

Figure 5.7: Cross section integrated over -0.8 $< \cos(\theta^{cm}_{K^0_S}) <$ 0.8 and the extrapolated total cross section for CLAS data. The vertical error bars are due to counting statistics, the horizontal bars represent the energy interval over which the data are summed.

5.3 Comparisons with previous experiments

5.3.1 ABBHHM and SAPHIR total cross sections

The ABBHHM collaboration published only two total cross section measurements in our photon energy region. SAPHIR measured five total cross section values as a function of photon energy up to an energy of 1.55 GeV. The ABBHHM data points have large error bars due to very low statistics. Figure 5.8 shows a comparison of our extrapolated total cross section with these total cross section results for ABBHHM and SAPHIR. Our results have higher statistics and cover a larger photon energy range, though are statistically lower in magnitude than the SAPHIR results.

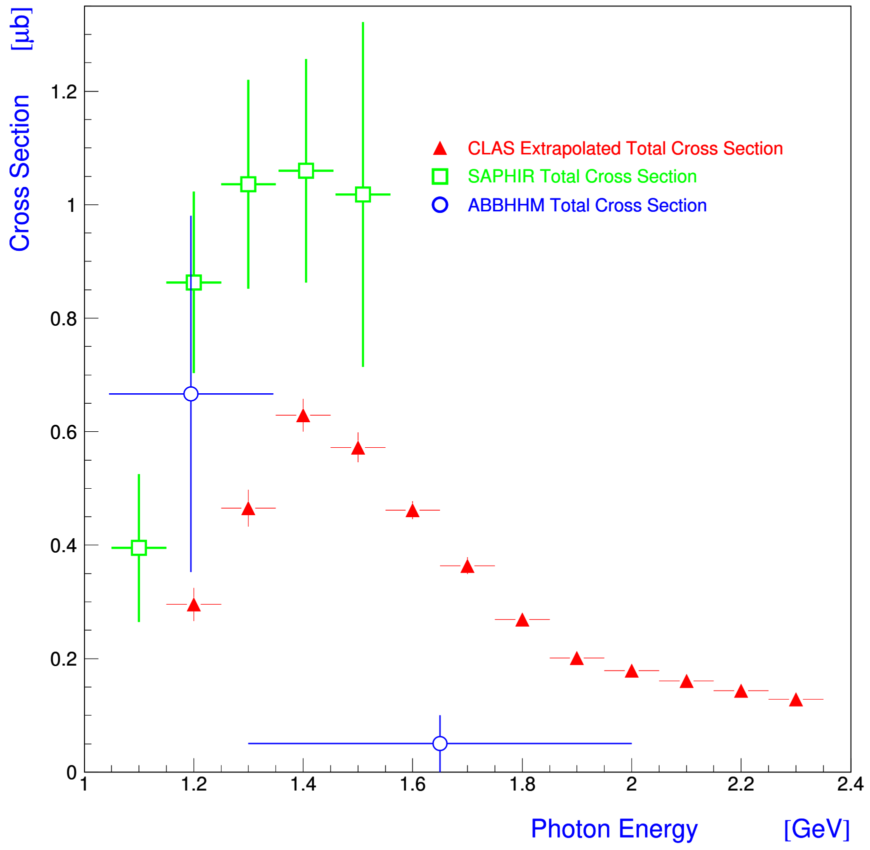

Figure 5.8: CLAS extrapolated total cross section in comparison with ABBHHM [16] and SAPHIR [17] results.

5.3.2 SAPHIR differential cross sections

Figure 5.9 shows a comparison of our differential cross sections with those of SAPHIR. Here the SAPHIR data are combined into two 200 MeV wide energy bins. In the lowest energy bin(top plot), our data are significantly below the SAPHIR data for forward angles. In the higher energy bin(bottom plot) both data sets show somewhat better agreement, but again our values are consistently smaller than the SAPHIR data at forward angles.

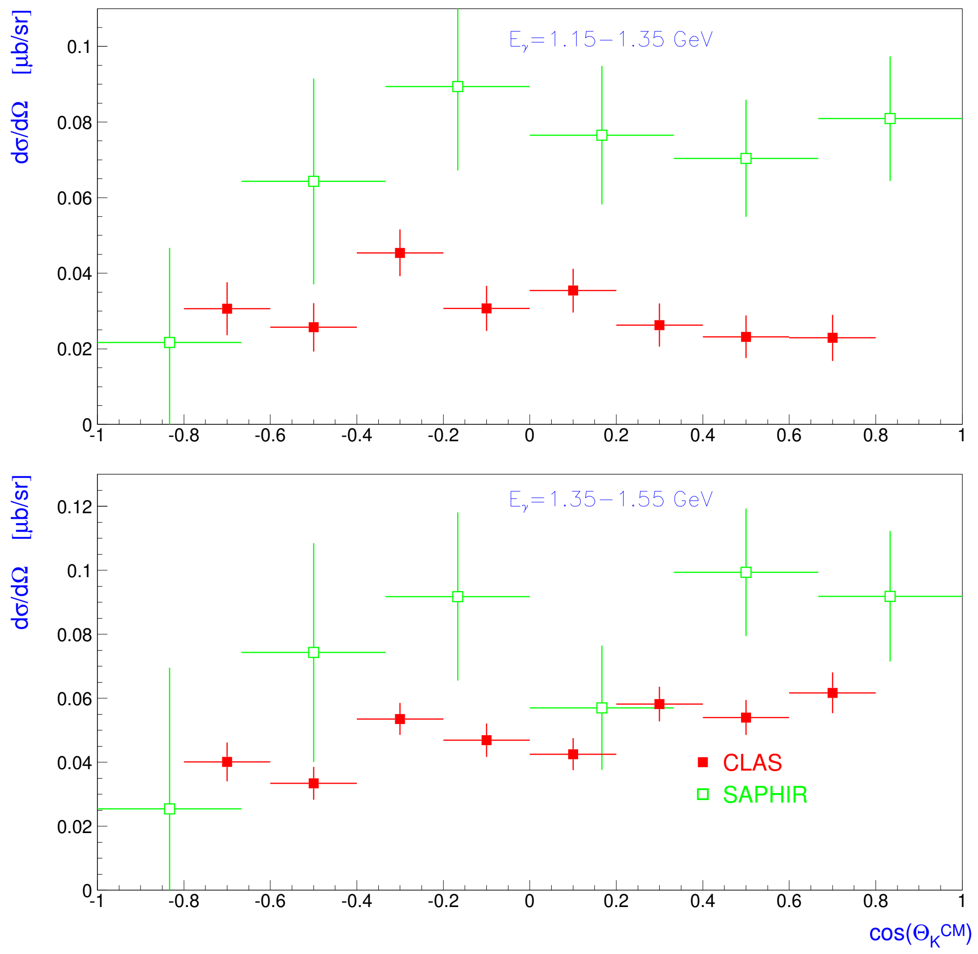

Figure 5.9: Comparison of CLAS differential cross section with SAPHIR data [17]. CLAS data are solid squares and SAPHIR data are open squares.

5.4 Comparisons with theoretical models

5.4.1 Coupled channel model by Penner and Mosel

Our results can be compared with the theoretical predictions previously discussed in section 1.2.2 and shown in Fig. 1.4, 1.5, and 1.6. Figure 5.10 shows CLAS and SAPHIR data plotted with two calculations for total cross section by Penner and Mosel, $C-p\gamma+$ and $C-p\gamma-$. This figure shows that the earlier SAPHIR experimental data below 1.55 GeV photon energy could be used to support these predictions. Our data are clearly lower than these predictions. Our data, however, show a clear decrease in cross section at higher photon energies, which is very different from the rising cross section of the $C-p\gamma-$ prediction. Our data also differ from the $C-p\gamma+$ prediction as they increase and decrease more gradually than the $C-p\gamma+$ predicts.

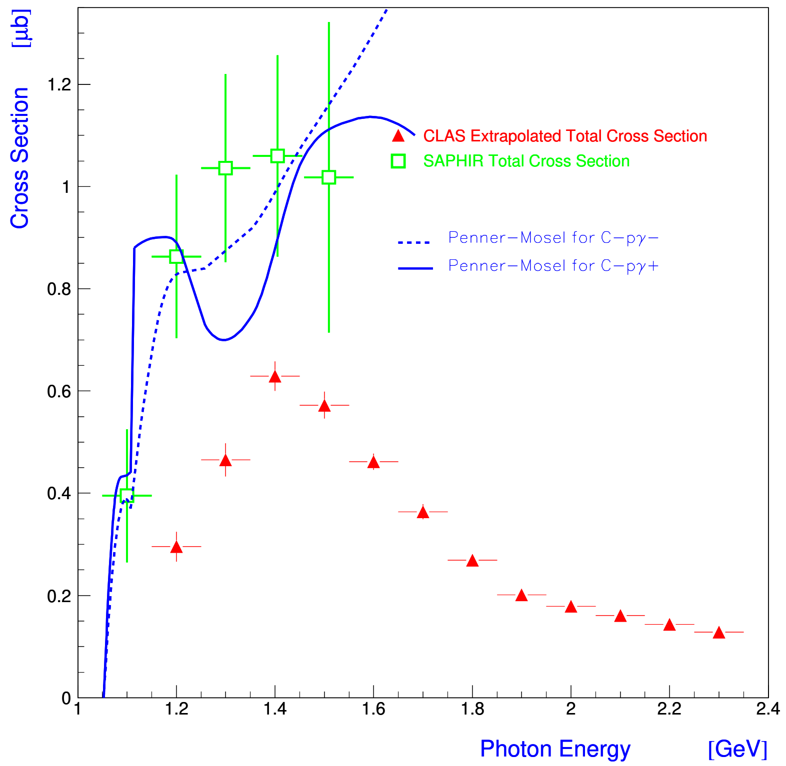

Figure 5.10: CLAS and SAPHIR data compared with theoretical calculations by Penner and Mosel. The solid line is the $C-p\gamma+$ calculation, and the dotted line is the $C-p\gamma-$ calculation.

The discrepancies between Penner and Mosel's predictions for total cross section and CLAS data are also present in the differential cross section, as shown in Fig. 5.11. The SAPHIR data are also shown in this figure. In the top plot, the shape of our data agrees more with the $C-p\gamma-$ than the $C-p\gamma+$. As the photon energy increases, the CLAS data disagree more with the differential cross section predictions, shown in the lower two plots of Fig. 5.10.

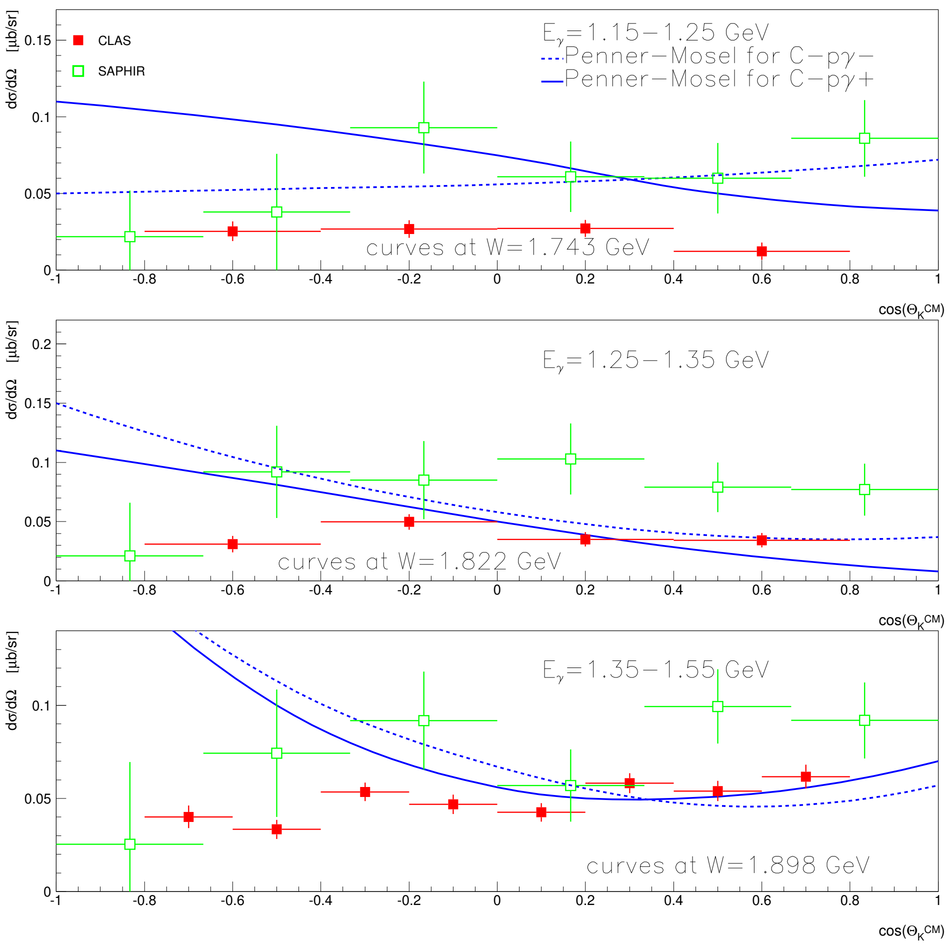

Figure 5.11: Differential cross sections from CLAS and SAPHIR compared with theoretical calculations by Penner and Mosel. The solid line is the $C-p\gamma+$ calculation, and the dotted line is the $C-p\gamma-$ calculation, evaluated at values of W=1.743, 1.822 and 1.898 GeV, which correspond respectively to $E_\gamma = 1.20$, 1.30 and 1.45 GeV.

Our data are also compared with a partial wave decomposition of Penner and Mosel's predictions, similar to Fig. 1.6. This is shown in Fig. 5.12, where it is clear that the $J^P = \frac{1}{2}^-$ contribution does not describe the data as the prediction has a sharp peak at 1.15 MeV and then rapidly declines, while our data peaks around 1.4 MeV. The experimental data appear more like the prediction for the $J^P = \frac{1}{2}^+$ contribution.

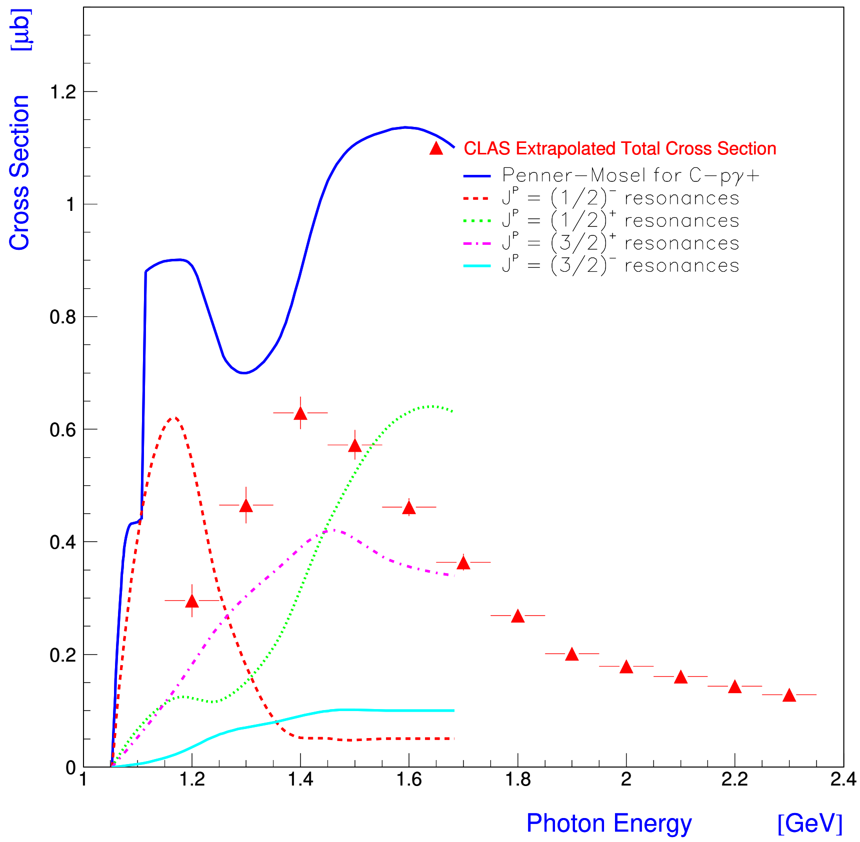

Figure 5.12: CLAS data for total cross sections compared with partial wave decomposition of Penner and Mosel predictions. The solid line is the $C - p\gamma+$ calculation, the dashed line is for resonances with $J^P = \frac{1}{2}^-$, the dotted line for $J^P = \frac{1}{2}^+$(including the $P_{11}(1710)$), the dash-dotted line for $J^P = \frac{3}{2}^+$ (including the $P_{33}(1920)$ and $P_{13}(1900)$) and the grey line for $J^P = \frac{3}{2}^-$.

5.4.2 Isobar model by Mart and Bennhold

The KAON-MAID parameterization code uses the Mart-Bennhold isobar model (Section 1.2.1.3), determining the parameters from a fit to existing experimental data. The web-version of the code [10] calculated theoretical predictions for differential cross sections, which we then summed in full or partial angular ranges for data comparisons.

5.4.2.1 Total cross section

Figure 5.13 shows CLAS data compared to KAON-MAID predictions. The top curve is the predicted total cross section, while the lower curve is the prediction only in the angular range in which our data were analyzed, -0.8 < $\cos(\theta^{cm}_{K^0_S})$ < 0.8. Our data have a similar shape as the KAON-MAID prediction, but are smaller in magnitude. The model is based upon a fit to previously existing experimental data which only went as high as 1.55 GeV in photon energy and reported higher cross sections than in this analysis. The rise predicted for energies above 1.9 GeV is not present in our data.

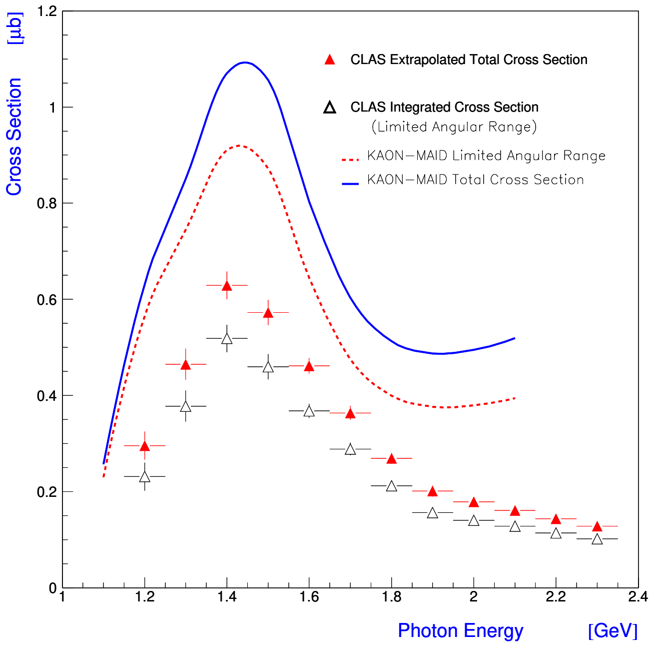

Figure 5.13: Comparison of CLAS cross sections (data points) with KAON-MAID predictions (curves). The open data points and dotted curve are for -0.8 < $\cos(\theta^{cm}_{K^0_S})$ < 0.8. The solid data points and solid curve are for the entire angular range.

5.4.2.2 Differential cross section

To better identify the differences that exist between our results and the KAON-MAID predictions, the differential cross section results are compared as shown in Fig. 5.14. In the lowest photon energy bin, 1.15-1.35 GeV, our experimental results have a more flat angular behavior than the KAON-MAID prediction. In the photon energy bin 1.35-1.55 GeV, our data have a similar angular distribution as the KAON-MAID curve, but with smaller magnitude. Above 1.55 GeV, where experimental data for $\gamma p \to K^0\Sigma^+$ did not exist before, there are more significant differences between the angular distribution of our results and KAON-MAID predictions. It is clear that our data will be able to make a significant contribution to model predictions. KAON-MAID predictions do not exist for energies above 2.15 GeV, thus they do not appear in the figures.

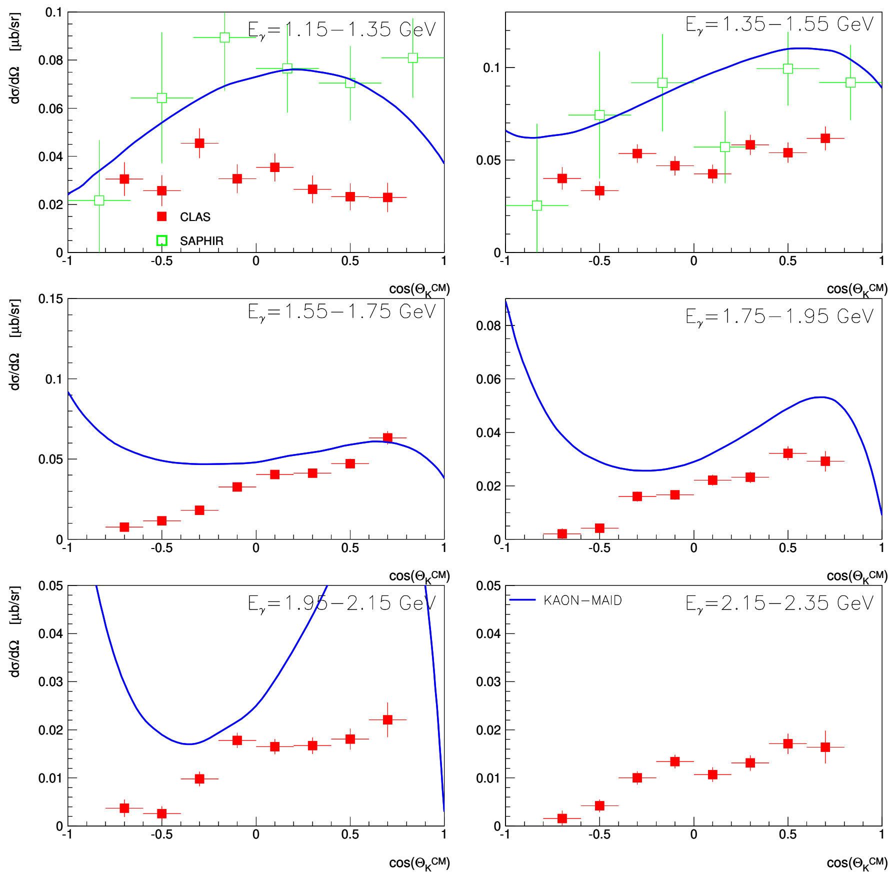

Figure 5.14: Comparison of CLAS differential cross sections with KAON-MAID predictions. There are notable differences at photon energies above 1.55 GeV.

5.4.2.3 Partial wave decomposition

To better understand the results shown in Fig. 5.13 and 5.14, and the noticable differences between the angular distribution of our data and the KAON-MAID predictions in the photon energy ranges from 1.55-2.15 GeV, KAON-MAID predictions are presented for total and differential cross sections decomposed into contributions from different resonances. We have separately identified contributions from the Born terms (the diagrams in the left column of Fig. 1.2), the $P_{13}(1720)$ resonance, the combination of the $S_{31}(1900)$ and $P_{31}(1910)$ resonances, and $K^*(893)$ meson exchange.

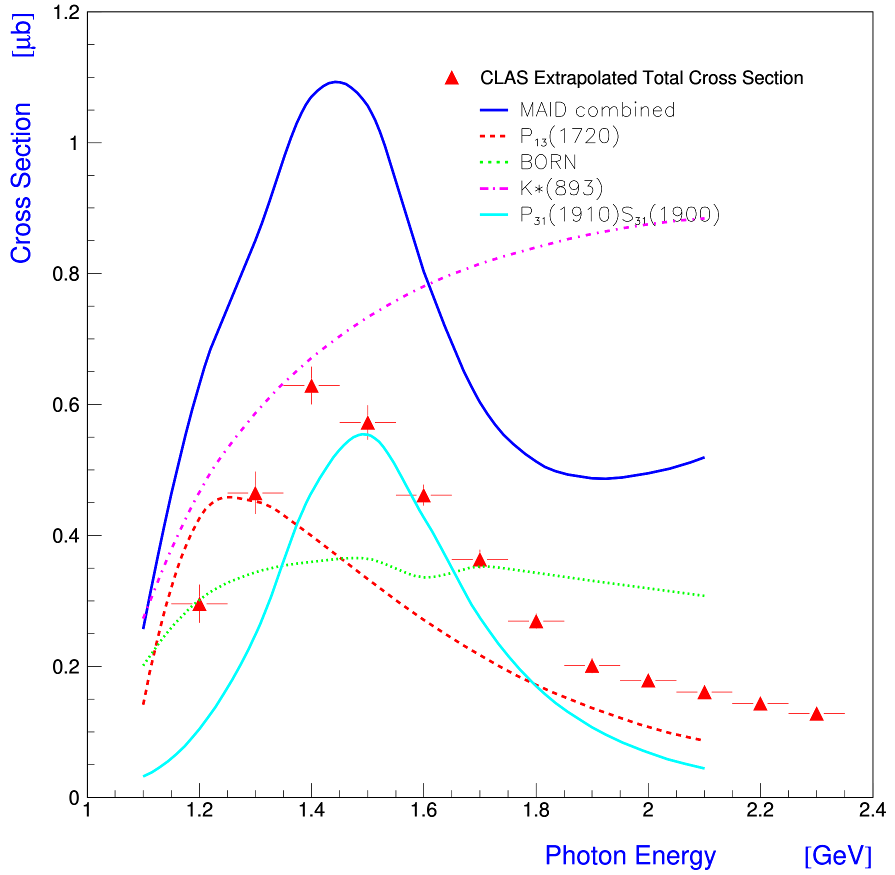

Figure 5.15: Comparison of CLAS total cross section with KAON-MAID prediction decomposed into partial waves. The dotted line is the Born contribution, the dashed line is the combination of the $S_{31}(1900)$ and $P_{31}(1910)$, the dot-dashed line is for the $P_{13}(1720)$ and the dot-dot-dashed line is from the K^* exchange.

Figure 5.15 shows this decomposition plotted with our experimental data for the total cross section. As the amplitudes are added coherently, thus giving rise to interference effects, it is not possible to draw full conclusions based on diagrams such as this. We can however identify which resonances are more prominent in different regions of energy and angle by looking additionally into their angular behavior.

For a more comprehensive analysis of this decomposition, the partial wave decomposition for the differential cross sections is shown in Fig. 5.16. When observing these differential cross sections in reference to the diagrams of Fig. 1.2, the s-channel contributions will be symmetric in angular distribution over the angular range, the t-channel contributions will peak in the forward direction, and the u-channel contributions will peak in the backward direction.

In the first photon energy bin, 1.15-1.35 GeV, our data are lower and have a flatter angular distribution than the KAON-MAID prediction, which is dominated by the $P_{13}(1720)$ resonance and $K^*(893)$ exchange. In the photon energy bin 1.35-1.55 GeV, our angular distribution is more in agreement with KAON-MAID predictions, but with a smaller magnitude. In this photon energy bin the cross section appears to be dominated by the $K^*(893)$ and the $S_{31}(1900)$ and $P_{31}(1910)$ contributions. Most notable is the effect of resonance contributions in the line slope of the resonance as a function of energy, i.e. their Breit-Wigner sloped contributions (Eq. 1.10) to the total cross section. Figure 5.15 shows that the cross section peaking is dominated by $S_{31}(1900)$ and $P_{31}(1910)$, in addition to the tail of the $P_{13}(1720)$ resonance. At energies above 1.55 GeV, where previous experimental data do not exist, the differences are more significant. Most noticably is the presence of the Born terms in the KAON-MAID calculations with strong u-channel effects of peaking in the backward direction (Σ^+-exchange) not evident in our data. In the photon energy bin 1.55-1.75 GeV, our data are forward peaked while the KAON-MAID results are fairly flat. This could suggest a greater contribution from the $S_{31}(1900)$ and $P_{31}(1910)$ terms than previously incorporated, as our experimental cross section appears to increase steadily with $\cos(\theta^{cm}_{K^0_S})$ as the s- and p-wave inteference term ($S_{31}(1900)$-$P_{31}(1910)$) does, but does not drop off as the $K^*(893)$ contribution does. In the photon energy bin 1.75-1.95 GeV, with the exception of the backward peaking in KAON-MAID due to the Born terms, there is good agreement between the angular distribution of our data and the KAON-MAID prediction at forward angles. In the last photon energy bin for which there exist KAON-MAID predictions, 1.95-2.15 GeV, there is again backward peaking in KAON-MAID absent from our data, but also less of the $K^*(893)$ behavior that is present in KAON-MAID, causing strong forward peaking before quickly falling off.

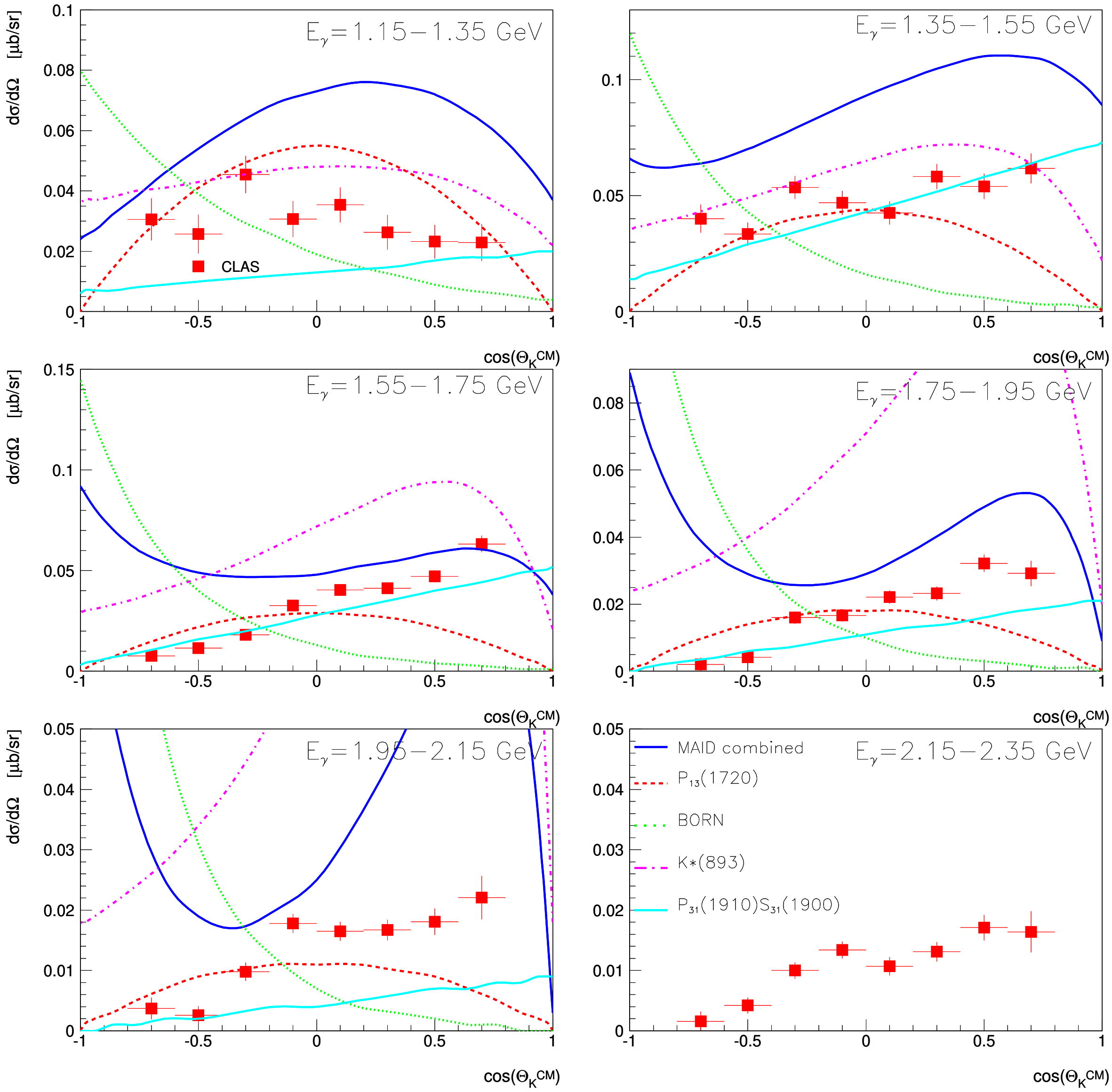

Figure 5.16: Comparison of CLAS differential cross sections with KAON-MAID predictions decomposed into partial waves. The dotted line is the Born contribution, the grey line is the combination of the $S_{31}(1900)$ and $P_{31}(1910)$, the dashed line is the $P_{13}(1720)$, and the dot-dashed line is from the K^* exchange.

This partial wave decomposition can also partially explain the differences between KAON-MAID and our experimental results for cross sections in the total angular range, and in the restricted angular range of -0.8 < $\cos(\theta^{cm}_{K^0_S})$< 0.8 as shown in Fig. 5.13. Figure 5.16 shows that the large discrepancy in the backward peaking of KAON-MAID, due to Born terms, versus our experimental results will contribute significantly to the total KAON-MAID cross section being greater than our experimental data for these energies, as shown in Fig. 5.13 above 1.55 GeV. This also appears to be the case in the figure for the partial wave decomposition for the total cross section, Fig. 5.15, where the Born terms appear to be too prominent in the model for the higher photon energies.

Chapter 6

Conclusions

- This analysis obtained results for differential and total cross sections for the reaction $\gamma p \to \mathrm{K}^0\Sigma^+$ in the photon energy range 1.15-2.35 GeV. This greatly expands upon previously existing data. Detailed results are listed in Appendix A.

- Our total cross sections are similar in shape to, but lower than previous experimental data and theoretical predictions of the KAON-MAID isobar model. Our data have much higher statistics than previous experiments. The ABBHHM and SAPHIR experiments produced 18 and 405 background-subtracted events respectively, our experiment identified a total of 15,650 background-subtracted Σ^+ events: 9,840 for the $\Sigma^+ \to p\pi^0$ decay channel and 5,810 for the $\Sigma^+ \to n\pi^+$ decay channel.

- At photon energies greater than those of previous experimental data, our CLAS data does not agree with KAON-MAID predictions. Comparing our experimental results with the partial wave decomposition of the KAON-MAID predictions, our experimental data suggest decreasing the u-channel Born term contributions to the differential cross section predictions at photon energies greater than 1.55 GeV, which should significantly reduce the KAON-MAID total cross section values in that photon energy range.

- Future experiments with higher statistics than this analysis and with the extraction of polarization observables would provide a basis for further refinement of these theoretical models.

Appendix A

Tables of differential, integrated and extrapolated total cross sections

The values for differential cross section for the combined data set, followed by the partial differential cross sections for the $\Sigma^+ \rightarrow p\pi^0$ and $\Sigma^+ \rightarrow n\pi^+$ decay channels are presented in Table A.1.

Table A.1: Differential cross section

E_γ (GeV)	$\cos(\theta^{cm}_{K^0_S})$	$\frac{d\sigma}{d\Omega}$ $(\frac{\mu b}{sr})$
1.15-1.35	0.8 to 0.6	0.0229 $\pm$ 0.0061
1.15-1.35	0.6 to 0.4	0.0232 $\pm$ 0.0056
1.15-1.35	0.4 to 0.2	0.0263 $\pm$ 0.0057
1.15-1.35	0.2 to 0.0	0.0354 $\pm$ 0.0058
1.15-1.35	0.0 to -0.2	0.0307 $\pm$ 0.0060
1.15-1.35	-0.2 to -0.4	0.0454 $\pm$ 0.0062
1.15-1.35	-0.4 to -0.6	0.0257 $\pm$ 0.0064
1.15-1.35	-0.6 to -0.8	0.0306 $\pm$ 0.0070
1.35-1.55	0.8 to 0.6	0.0617 $\pm$ 0.0064
1.35-1.55	0.6 to 0.4	0.0540 $\pm$ 0.0055
1.35-1.55	0.4 to 0.2	0.0582 $\pm$ 0.0054
1.35-1.55	0.2 to 0.0	0.0425 $\pm$ 0.0050
1.35-1.55	0.0 to -0.2	0.0469 $\pm$ 0.0052
1.35-1.55	-0.2 to -0.4	0.0535 $\pm$ 0.0050
1.35-1.55	-0.4 to -0.6	0.0334 $\pm$ 0.0051
1.35-1.55	-0.6 to -0.8	0.0401 $\pm$ 0.0061
1.55-1.75	0.8 to 0.6	0.0633 $\pm$ 0.0042
1.55-1.75	0.6 to 0.4	0.0472 $\pm$ 0.0031
1.55-1.75	0.4 to 0.2	0.0413 $\pm$ 0.0027
1.55-1.75	0.2 to 0.0	0.0405 $\pm$ 0.0026
1.55-1.75	0.0 to -0.2	0.0326 $\pm$ 0.0024
1.55-1.75	-0.2 to -0.4	0.0182 $\pm$ 0.0023
1.55-1.75	-0.4 to -0.6	0.0115 $\pm$ 0.0022
1.55-1.75	-0.6 to -0.8	0.0076 $\pm$ 0.0027
1.75-1.95	0.8 to 0.6	0.0292 $\pm$ 0.0038
1.75-1.95	0.6 to 0.4	0.0322 $\pm$ 0.0026
1.75-1.95	0.4 to 0.2	0.0232 $\pm$ 0.0021
1.75-1.95	0.2 to 0.0	0.0221 $\pm$ 0.0020
1.75-1.95	0.0 to -0.2	0.0166 $\pm$ 0.0018
1.75-1.95	-0.2 to -0.4	0.0160 $\pm$ 0.0019
1.75-1.95	-0.4 to -0.6	0.0042 $\pm$ 0.0017
1.75-1.95	-0.6 to -0.8	0.0020 $\pm$ 0.0021
1.95-2.15	0.8 to 0.6	0.0221 $\pm$ 0.0036
1.95-2.15	0.6 to 0.4	0.0181 $\pm$ 0.0022
1.95-2.15	0.4 to 0.2	0.0167 $\pm$ 0.0017
1.95-2.15	0.2 to 0.0	0.0165 $\pm$ 0.0016
1.95-2.15	0.0 to -0.2	0.0178 $\pm$ 0.0016
1.95-2.15	-0.2 to -0.4	0.0098 $\pm$ 0.0015
1.95-2.15	-0.4 to -0.6	0.0026 $\pm$ 0.0015
1.95-2.15	-0.6 to -0.8	0.0037 $\pm$ 0.0018
2.15-2.35	0.8 to 0.6	0.0164 $\pm$ 0.0034
2.15-2.35	0.6 to 0.4	0.0171 $\pm$ 0.0021
2.15-2.35	0.4 to 0.2	0.0131 $\pm$ 0.0016
2.15-2.35	0.2 to 0.0	0.0107 $\pm$ 0.0015
2.15-2.35	0.0 to -0.2	0.0134 $\pm$ 0.0014
2.15-2.35	-0.2 to -0.4	0.0100 $\pm$ 0.0014
2.15-2.35	-0.4 to -0.6	0.0042 $\pm$ 0.0013
2.15-2.35	-0.6 to -0.8	0.0016 $\pm$ 0.0016

Table A.2: Partial differential cross section for the decay channel $\gamma p \rightarrow K^0\Sigma^+ \rightarrow (\pi^+\pi^-)(p\ \pi^0)$ for three subsets of the data ($\frac{\mu b}{sr}$)

E_γ (GeV)	$\cos(\theta^{cm}_{K^0_S})$	2.445 GeV data	3.115 GeV half tagger	3.115 GeV full tagger
1.15-1.35	0.8 to 0.6	0.0233 ± 0.0093		
1.15-1.35	0.6 to 0.4	0.0188 ± 0.0079		
1.15-1.35	0.4 to 0.2	0.0263 ± 0.0078		
1.15-1.35	0.2 to 0.0	0.0503 ± 0.0081		
1.15-1.35	0.0 to -0.2	0.0303 ± 0.0082		
1.15-1.35	-0.2 to -0.4	0.0424 ± 0.0077		
1.15-1.35	-0.4 to -0.6	0.0210 ± 0.0075		
1.15-1.35	-0.6 to -0.8	0.0325 ± 0.0078		
1.35-1.55	0.8 to 0.6	0.0628 ± 0.0087		
1.35-1.55	0.6 to 0.4	0.0500 ± 0.0069		
1.35-1.55	0.4 to 0.2	0.0565 ± 0.0065		
1.35-1.55	0.2 to 0.0	0.0491 ± 0.0061		
1.35-1.55	0.0 to -0.2	0.0443 ± 0.0060		
1.35-1.55	-0.2 to -0.4	0.0493 ± 0.0054		
1.35-1.55	-0.4 to -0.6	0.0353 ± 0.0054		
1.35-1.55	-0.6 to -0.8	0.0309 ± 0.0056		
1.55-1.75	0.8 to 0.6	0.0450 ± 0.0094	0.0577 ± 0.0085	0.0607 ± 0.0125
1.55-1.75	0.6 to 0.4	0.0451 ± 0.0070	0.0398 ± 0.0061	0.0425 ± 0.0087
1.55-1.75	0.4 to 0.2	0.0445 ± 0.0058	0.0422 ± 0.0052	0.0355 ± 0.0074
1.55-1.75	0.2 to 0.0	0.0324 ± 0.0053	0.0346 ± 0.0047	0.0497 ± 0.0071
1.55-1.75	0.0 to -0.2	0.0290 ± 0.0049	0.0329 ± 0.0043	0.0235 ± 0.0063
1.55-1.75	-0.2 to -0.4	0.0215 ± 0.0045	0.0170 ± 0.0040	0.0096 ± 0.0056
1.55-1.75	-0.4 to -0.6	0.0108 ± 0.0041	0.0131 ± 0.0037	0.0236 ± 0.0059
1.55-1.75	-0.6 to -0.8	0.0096 ± 0.0044	0.0020 ± 0.0039	0.0173 ± 0.0058
1.75-1.95	0.8 to 0.6	0.0186 ± 0.0110	0.0402 ± 0.0081	0.0203 ± 0.0111
1.75-1.95	0.6 to 0.4	0.0190 ± 0.0070	0.0260 ± 0.0050	0.0410 ± 0.0075
1.75-1.95	0.4 to 0.2	0.0200 ± 0.0054	0.0204 ± 0.0040	0.0209 ± 0.0057
1.75-1.95	0.2 to 0.0	0.0231 ± 0.0051	0.0250 ± 0.0036	0.0233 ± 0.0052
1.75-1.95	0.0 to -0.2	0.0121 ± 0.0046	0.0125 ± 0.0033	0.0197 ± 0.0048
1.75-1.95	-0.2 to -0.4	0.0226 ± 0.0044	0.0115 ± 0.0029	0.0149 ± 0.0045
1.75-1.95	-0.4 to -0.6	0.0114 ± 0.0040	0.0046 ± 0.0027	0.0054 ± 0.0041
1.75-1.95	-0.6 to -0.8	0.0031 ± 0.0046	0.0046 ± 0.0032	0.0000 ± 0.0048
1.95-2.15	0.8 to 0.6	0.0391 ± 0.0101	0.0248 ± 0.0080	0.0009 ± 0.0112
1.95-2.15	0.6 to 0.4	0.0208 ± 0.0057	0.0125 ± 0.0045	0.0313 ± 0.0072
1.95-2.15	0.4 to 0.2	0.0166 ± 0.0043	0.0167 ± 0.0034	0.0186 ± 0.0053
1.95-2.15	0.2 to 0.0	0.0117 ± 0.0036	0.0179 ± 0.0031	0.0163 ± 0.0046
1.95-2.15	0.0 to -0.2	0.0177 ± 0.0036	0.0131 ± 0.0028	0.0222 ± 0.0043
1.95-2.15	-0.2 to -0.4	0.0087 ± 0.0032	0.0087 ± 0.0026	0.0062 ± 0.0037
1.95-2.15	-0.4 to -0.6	0.0045 ± 0.0031	0.0015 ± 0.0025	0.0010 ± 0.0036
1.95-2.15	-0.6 to -0.8	0.0074 ± 0.0035	0.0062 ± 0.0029	0.0023 ± 0.0044
2.15-2.35	0.8 to 0.6	0.0209 ± 0.0094	0.0165 ± 0.0074	0.0090 ± 0.0107
2.15-2.35	0.6 to 0.4	0.0200 ± 0.0056	0.0172 ± 0.0044	0.0113 ± 0.0064
2.15-2.35	0.4 to 0.2	0.0132 ± 0.0042	0.0130 ± 0.0033	0.0134 ± 0.0049
2.15-2.35	0.2 to 0.0	0.0115 ± 0.0035	0.0095 ± 0.0027	0.0099 ± 0.0042
2.15-2.35	0.0 to -0.2	0.0153 ± 0.0033	0.0117 ± 0.0026	0.0127 ± 0.0038
2.15-2.35	-0.2 to -0.4	0.0066 ± 0.0028	0.0106 ± 0.0023	0.0125 ± 0.0034
2.15-2.35	-0.4 to -0.6	0.0047 ± 0.0027	0.0043 ± 0.0023	0.0017 ± 0.0030
2.15-2.35	-0.6 to -0.8	0.0019 ± 0.0033	0.0017 ± 0.0026	0.0000 ± 0.0034

Table A.3: Partial differential cross section for the decay channel $\gamma p \to K^0\Sigma^+ \to (\pi^+\pi^-)(n\ \pi^+)$ for three subsets of the data ($\frac{\mu b}{sr}$)

E_γ (GeV)	$\cos(\theta^{cm}_{K^0_S})$	2.445 GeV data	3.115 GeV half tagger	3.115 GeV full tagger
1.15-1.35	0.8 to 0.6	0.0225 ± 0.0079		
1.15-1.35	0.6 to 0.4	0.0279 ± 0.0079		
1.15-1.35	0.4 to 0.2	0.0262 ± 0.0083		
1.15-1.35	0.2 to 0.0	0.0196 ± 0.0085		
1.15-1.35	0.0 to -0.2	0.0312 ± 0.0089		
1.15-1.35	-0.2 to -0.4	0.0487 ± 0.0099		
1.15-1.35	-0.4 to -0.6	0.0307 ± 0.0105		
1.15-1.35	-0.6 to -0.8	0.0286 ± 0.0118		
1.35-1.55	0.8 to 0.6	0.0608 ± 0.0094		
1.35-1.55	0.6 to 0.4	0.0585 ± 0.0088		
1.35-1.55	0.4 to 0.2	0.0601 ± 0.0087		
1.35-1.55	0.2 to 0.0	0.0356 ± 0.0082		
1.35-1.55	0.0 to -0.2	0.0499 ± 0.0086		
1.35-1.55	-0.2 to -0.4	0.0582 ± 0.0086		
1.35-1.55	-0.4 to -0.6	0.0314 ± 0.0089		
1.35-1.55	-0.6 to -0.8	0.0500 ± 0.0112		
1.55-1.75	0.8 to 0.6	0.0650 ± 0.0107	0.0808 ± 0.0090	0.0717 ± 0.0144
1.55-1.75	0.6 to 0.4	0.0501 ± 0.0081	0.0554 ± 0.0067	0.0506 ± 0.0106
1.55-1.75	0.4 to 0.2	0.0399 ± 0.0073	0.0331 ± 0.0060	0.0633 ± 0.0103
1.55-1.75	0.2 to 0.0	0.0382 ± 0.0072	0.0393 ± 0.0058	0.0674 ± 0.0101
1.55-1.75	0.0 to -0.2	0.0441 ± 0.0072	0.0311 ± 0.0056	0.0345 ± 0.0088
1.55-1.75	-0.2 to -0.4	0.0212 ± 0.0067	0.0195 ± 0.0056	0.0171 ± 0.0084
1.55-1.75	-0.4 to -0.6	0.0197 ± 0.0070	0.0075 ± 0.0053	0.0000 ± 0.0076
1.55-1.75	-0.6 to -0.8	0.0111 ± 0.0083	0.0031 ± 0.0067	0.0112 ± 0.0110
1.75-1.95	0.8 to 0.6	0.0339 ± 0.0112	0.0220 ± 0.0067	0.0378 ± 0.0114
1.75-1.95	0.6 to 0.4	0.0493 ± 0.0089	0.0334 ± 0.0050	0.0312 ± 0.0083
1.75-1.95	0.4 to 0.2	0.0297 ± 0.0066	0.0221 ± 0.0040	0.0324 ± 0.0071
1.75-1.95	0.2 to 0.0	0.0261 ± 0.0064	0.0159 ± 0.0039	0.0232 ± 0.0068
1.75-1.95	0.0 to -0.2	0.0304 ± 0.0064	0.0144 ± 0.0038	0.0192 ± 0.0062
1.75-1.95	-0.2 to -0.4	0.0110 ± 0.0063	0.0193 ± 0.0044	0.0185 ± 0.0063
1.75-1.95	-0.4 to -0.6	0.0030 ± 0.0052	0.0044 ± 0.0038	0.0000 ± 0.0057
1.75-1.95	-0.6 to -0.8	0.0052 ± 0.0077	0.0000 ± 0.0041	0.0101 ± 0.0094
1.95-2.15	0.8 to 0.6	0.0108 ± 0.0083	0.0263 ± 0.0068	0.0207 ± 0.0105
1.95-2.15	0.6 to 0.4	0.0235 ± 0.0057	0.0150 ± 0.0040	0.0126 ± 0.0067
1.95-2.15	0.4 to 0.2	0.0172 ± 0.0046	0.0149 ± 0.0034	0.0181 ± 0.0057
1.95-2.15	0.2 to 0.0	0.0073 ± 0.0042	0.0220 ± 0.0036	0.0257 ± 0.0056
1.95-2.15	0.0 to -0.2	0.0189 ± 0.0047	0.0164 ± 0.0035	0.0265 ± 0.0059
1.95-2.15	-0.2 to -0.4	0.0188 ± 0.0048	0.0077 ± 0.0033	0.0119 ± 0.0053
1.95-2.15	-0.4 to -0.6	0.0000 ± 0.0043	0.0061 ± 0.0035	0.0000 ± 0.0052
1.95-2.15	-0.6 to -0.8	0.0025 ± 0.0053	0.0045 ± 0.0048	0.0000 ± 0.0069
2.15-2.35	0.8 to 0.6	0.0160 ± 0.0089	0.0201 ± 0.0060	0.0109 ± 0.0095
2.15-2.35	0.6 to 0.4	0.0188 ± 0.0055	0.0143 ± 0.0037	0.0244 ± 0.0064
2.15-2.35	0.4 to 0.2	0.0107 ± 0.0044	0.0124 ± 0.0033	0.0184 ± 0.0050
2.15-2.35	0.2 to 0.0	0.0111 ± 0.0039	0.0102 ± 0.0031	0.0139 ± 0.0052
2.15-2.35	0.0 to -0.2	0.0166 ± 0.0044	0.0150 ± 0.0031	0.0078 ± 0.0047
2.15-2.35	-0.2 to -0.4	0.0076 ± 0.0043	0.0116 ± 0.0031	0.0108 ± 0.0055
2.15-2.35	-0.4 to -0.6	0.0049 ± 0.0044	0.0055 ± 0.0029	0.0024 ± 0.0054
2.15-2.35	-0.6 to -0.8	0.0022 ± 0.0043	0.0004 ± 0.0043	0.0051 ± 0.0056

Integrated and Extrapolated Total Cross Section

The integrated and extrapolated total cross sections are tabulated in Table A.4. The integrated cross section is calculated by adding the differential cross sections from 4 angular bins in each from -0.8 < $\cos(\theta^{cm}_{K^0_S})$< 0.8 and 100 MeV photon energy bins, then multiplying by 2π to account for the integral over ϕ angles and by 0.4 which is the size of the angular bin in $\cos(\theta^{cm}_{K^0_S})$. The extrapolated total cross section is obtained by fitting a straight line to the differential cross section data and then adding the points on that line, which are centered on 0.9 and -0.9 for $\cos(\theta^{cm}_{K^0_S})$ to the integrated cross section, thus accounting for the unanalyzed angular ranges. As data below 1.55 GeV photon energy from the 3.115 GeV beam energy data set were not considered, those parts of the table are left blank.

Table A.4: Integrated and extrapolated total cross section

E_γ (GeV)	Integrated Cross Section (μb)	Extrapolated Cross Section (μb)
1.15-1.25	0.231 ± 0.029	0.296 ± 0.037
1.25-1.35	0.378 ± 0.032	0.465 ± 0.039
1.35-1.45	0.518 ± 0.029	0.629 ± 0.035
1.45-1.55	0.460 ± 0.026	0.572 ± 0.032
1.55-1.65	0.368 ± 0.015	0.461 ± 0.019
1.65-1.75	0.289 ± 0.013	0.364 ± 0.016
1.75-1.85	0.212 ± 0.011	0.269 ± 0.014
1.85-1.95	0.156 ± 0.011	0.201 ± 0.014
1.95-2.05	0.140 ± 0.010	0.179 ± 0.013
2.05-2.15	0.128 ± 0.009	0.161 ± 0.011
2.15-2.25	0.114 ± 0.009	0.144 ± 0.011
2.25-2.35	0.102 ± 0.008	0.128 ± 0.010

Table A.5: Integrated partial cross sections for $\Sigma^+ \to p\pi^0$ and $\Sigma^+ \to n\pi^+$

E_γ (GeV)	$\gamma p \to K^0\Sigma^+ \to p\pi^+\pi^-\pi^0 (\mu b)$	$\gamma p \to K^0\Sigma^+ \to n\pi^+\pi^+\pi^- (\mu b)$
1.15-1.25	0.229 ± 0.041	0.234 ± 0.042
1.25-1.35	0.390 ± 0.040	0.366 ± 0.052
1.35-1.45	0.489 ± 0.034	0.552 ± 0.047
1.45-1.55	0.461 ± 0.030	0.460 ± 0.044
1.55-1.65	0.351 ± 0.018	0.389 ± 0.024
1.65-1.75	0.259 ± 0.016	0.320 ± 0.021
1.75-1.85	0.201 ± 0.015	0.221 ± 0.017
1.85-1.95	0.149 ± 0.015	0.163 ± 0.017
1.95-2.05	0.120 ± 0.013	0.162 ± 0.015
2.05-2.15	0.149 ± 0.013	0.112 ± 0.012
2.15-2.25	0.117 ± 0.013	0.115 ± 0.013
2.25-2.35	0.094 ± 0.012	0.114 ± 0.012

Table A.6: Integrated partial cross sections for the $\gamma p \to K^0\Sigma^+ \to p\pi^+\pi^-\pi^0$ channel for all three data subsets

E_γ (GeV)	2.445 Gev(μb)	3.115 half tagger(μb)	3.115 full tagger(μb)
1.15-1.25	0.229 ± 0.041		
1.25-1.35	0.390 ± 0.040		
1.35-1.45	0.489 ± 0.034		
1.45-1.55	0.461 ± 0.030		
1.55-1.65	0.364 ± 0.030	0.329 ± 0.027	0.375 ± 0.039
1.65-1.75	0.236 ± 0.028	0.268 ± 0.025	0.281 ± 0.036
1.75-1.85	0.210 ± 0.028	0.192 ± 0.021	0.209 ± 0.030
1.85-1.95	0.096 ± 0.031	0.162 ± 0.021	0.173 ± 0.031
1.95-2.05	0.138 ± 0.025	0.115 ± 0.019	0.119 ± 0.028
2.05-2.15	0.161 ± 0.022	0.130 ± 0.019	0.171 ± 0.029
2.15-2.25	0.145 ± 0.023	0.114 ± 0.019	0.086 ± 0.027
2.25-2.35	0.088 ± 0.021	0.100 ± 0.017	0.091 ± 0.025

Table A.7: Integrated partial cross sections for the $\gamma p \rightarrow K^0\Sigma^+ \rightarrow n\pi^+\pi^+\pi^-$ channel for all three data subsets

E_γ (GeV)	2.445 Gev(μb)	3.115 half tagger(μb)	3.115 full tagger(μb)
1.15-1.25	0.234 ± 0.042		
1.25-1.35	0.366 ± 0.052		
1.35-1.45	0.552 ± 0.047		
1.45-1.55	0.460 ± 0.044		
1.55-1.65	0.366 ± 0.041	0.398 ± 0.034	0.407 ± 0.054
1.65-1.75	0.368 ± 0.038	0.275 ± 0.029	0.383 ± 0.047
1.75-1.85	0.295 ± 0.033	0.185 ± 0.023	0.215 ± 0.038
1.85-1.95	0.168 ± 0.034	0.144 ± 0.022	0.202 ± 0.038
1.95-2.05	0.205 ± 0.029	0.158 ± 0.020	0.131 ± 0.032
2.05-2.15	0.064 ± 0.024	0.117 ± 0.020	0.161 ± 0.032
2.15-2.25	0.102 ± 0.022	0.122 ± 0.019	0.125 ± 0.031
2.25-2.35	0.137 ± 0.027	0.103 ± 0.017	0.126 ± 0.029

Appendix B

Calculating the distance cut

A point on the proton track was determined by reading the PART bank tracking fit parameters. The tracking fit provides charge, momentum and the intersection of the track with the beam line. This point is often referred to as the "vertex". The proton track is determined via fitting to the drift chamber using the time to distance relation (time-based tracking). To get the vertex of the kaon, data from the VERT bank are used which reconstruct the vertex of all combinations of two detected particles, such as the detected π^+ and π^-. To calculate the distance, the formulas for a line are first considered:

$$x = x_0 + a(z - z_0) \tag{B.1}$$
$$y = y_0 + b(z - z_0), \tag{B.2}$$

which lead to $\frac{dx}{dz} = a$ and $\frac{dy}{dz} = b$, where x_0, y_0, and z_0 are the coordinates of a point on the line. Since the rate of change in x with respect to z is represented both by $\frac{dx}{dz}$ and $\frac{p_x}{p_z}$,

$$a = \frac{p_x}{p_z} \tag{B.3}$$
$$b = \frac{p_y}{p_z} \; . \tag{B.4}$$

The equation used to calculate the distance between a point x_1, y_1, and z_1 is

$$d^2 = (x_1 - x)^2 + (y_1 - y)^2 + (z_1 - z)^2. \tag{B.5}$$

Substituting in (1) and (2) and grouping terms by z:

$$d^2 = ((x_1 - x_0 + az_0) - az)^2 + ((y_1 - y_0 + bz_0) - bz)^2 + (z_1 - z)^2. \tag{B.6}$$

Taking the squares and grouping in terms of z:

$$d^2 = D + Ez + Fz^2, \tag{B.7}$$

where

$$D = (x_1 - x0 + az_0)^2 + (y_1 - y_0 + bz_0)^2 + z_1^2) \tag{B.8}$$
$$E = -2(a(x_1 - x_0 + az_0) + b(y_1 - y_0 + bz_0) + z_1) \tag{B.9}$$
$$F = a^2 + b^2 + 1. \tag{B.10}$$

The minimum of the distance is determined from equation B.6 by taking the derivative with respect to z and setting that equal to zero:

$$0 = 2d\frac{d}{dz}(d) = 2d(E + 2Fz). \tag{B.11}$$

Since $d = 0$ is the trivial case

$$E + 2Fz = 0 \tag{B.12}$$

and

$$z = -\frac{E}{2F}. \tag{B.13}$$

So then subsituting this into (1) and (2)

$$x = x_0 + G \tag{B.14}$$
$$y = y_0 + H \tag{B.15}$$

where

$$G = a(-\frac{E}{2F} - z_0) \tag{B.16}$$

and $$H = b(-\frac{E}{2F} - z_0) \tag{B.17}$$

The distance between the point of the reconstructed kaon vertex and the line of the proton track is

$$d^2 = (x_1 - (x_0 + G))^2 + (y_1 - (y_0 + H))^2 + (z_1 + \frac{E}{2F})^2. \tag{B.18}$$

Appendix C

Detailed systematic uncertainty comparisons

Figure C.1 presents data used to calculate systematic errors for the analysis of the $\Sigma^+ \to p\pi^0$ versus the $\Sigma^+ \to n\pi^+$ decay channels. These results are summarized in Table 4.8 in Section 4.4.2.2.

KEY:

PXS = partial integrated cross section obtained from data from the $\Sigma^+ \to p\pi^0$ decay channel

NXS = partial integrated cross section obtained from data from the $\Sigma^+ \to n\pi^+$ decay channel

stat err = the average fractional error for each 8 point set = $\frac{1}{8}\sum_{i=1}^{8}\frac{\Delta S}{S}$

chi sq = the χ^2 value comparing the two sets of results. 8 values of χ^2 for the 8 angular bins are presented, followed by the sum of those values

Z = the Z parameter comparing the two sets of results. 8 values of Z for the 8 angular bins are presented, followed by the sum of those values

syst error = the fractional systematic error determined by multiplying the average Z value by the fractional error

photon energy (GeV)	cos theta	P XS	error P XS	N XS	error N XS	ChiSQ	Z	stat. error	syst. error
1.15-1.35	0.6 to 0.8	0.0233	0.0093	0.0225	0.0079	0	0.07		
	0.4 to 0.6	0.0188	0.0079	0.0279	0.0079	0.67	-0.82		
	0.2 to 0.4	0.0263	0.0078	0.0262	0.0083	0	0.01		
	0.0 to 0.2	0.0503	0.0081	0.0196	0.0085	6.93	2.63		
	-0.2 to 0.0	0.0303	0.0082	0.0312	0.0089	0.01	-0.07		
	-0.4 to -0.2	0.0424	0.0077	0.0487	0.0099	0.25	-0.5		
	-0.6 to -0.4	0.0210	0.0075	0.0307	0.0105	0.56	-0.75		
	-0.8 to -0.6	0.0325	0.0078	0.0286	0.0118	0.07	0.27		
						8.5	0.85	0.29	0.03
1.35-1.55	0.6 to 0.8	0.0628	0.0087	0.0608	0.0094	0.02	0.15		
	0.4 to 0.6	0.0500	0.0069	0.0585	0.0088	0.58	-0.76		
	0.2 to 0.4	0.0565	0.0065	0.0601	0.0087	0.11	-0.33		
	0.0 to 0.2	0.0491	0.0061	0.0356	0.0082	1.75	1.32		
	-0.2 to 0.0	0.0443	0.0060	0.0499	0.0086	0.3	-0.54		
	-0.4 to -0.2	0.0493	0.0054	0.0582	0.0086	0.76	-0.87		
	-0.6 to -0.4	0.0353	0.0054	0.0314	0.0089	0.15	0.38		
	-0.8 to -0.6	0.0309	0.0056	0.0500	0.0112	2.33	-1.53		
						6	-0.65	0.14	0.01
1.55-1.75	0.6 to 0.8	0.0538	0.0056	0.0737	0.0062	5.54	-2.35		
	0.4 to 0.6	0.0422	0.0041	0.0528	0.0047	2.9	-1.7		
	0.2 to 0.4	0.0416	0.0034	0.0412	0.0043	0	0.07		
	0.0 to 0.2	0.0370	0.0031	0.0444	0.0041	2	-1.42		
	-0.2 to 0.0	0.0295	0.0029	0.0357	0.0040	1.59	-1.26		
	-0.4 to -0.2	0.0169	0.0026	0.0196	0.0038	0.33	-0.57		
	-0.6 to -0.4	0.0144	0.0025	0.0075	0.0037	2.37	1.54		
	-0.8 to -0.6	0.0079	0.0026	0.0073	0.0047	0.01	0.12		
						14.75	-3.23	0.14	0.07
1.75-1.95	0.6 to 0.8	0.0298	0.0056	0.0281	0.0051	0.05	0.22		
	0.4 to 0.6	0.0278	0.0036	0.0359	0.0039	2.37	-1.54		
	0.2 to 0.4	0.0204	0.0028	0.0261	0.0031	1.87	-1.37		
	0.0 to 0.2	0.0241	0.0026	0.0199	0.0030	1.16	1.08		
	-0.2 to 0.0	0.0142	0.0023	0.0188	0.0029	1.58	-1.26		
	-0.4 to -0.2	0.0150	0.0021	0.0171	0.0031	0.29	-0.54		
	-0.6 to -0.4	0.0065	0.0020	0.0018	0.0027	1.99	1.41		
	-0.8 to -0.6	0.0029	0.0023	0.0011	0.0036	0.17	0.41		
						9.48	-1.59	0.25	0.05
1.95-2.15	0.6 to 0.8	0.0234	0.0055	0.0203	0.0047	0.19	0.44		
	0.4 to 0.6	0.0193	0.0032	0.0167	0.0029	0.37	0.61		
	0.2 to 0.4	0.0171	0.0024	0.0162	0.0025	0.06	0.25		
	0.0 to 0.2	0.0154	0.0021	0.0178	0.0025	0.51	-0.71		
	-0.2 to 0.0	0.0165	0.0020	0.0192	0.0025	0.71	-0.84		
	-0.4 to -0.2	0.0082	0.0018	0.0114	0.0024	1.14	-1.07		
	-0.6 to -0.4	0.0023	0.0017	0.0043	0.0029	0.36	-0.6		
	-0.8 to -0.6	0.0057	0.0020	0.0016	0.0032	1.25	1.12		
						4.58	-0.81	0.26	0.03
2.15-2.35	0.6 to 0.8	0.0161	0.0051	0.0171	0.0044	0.02	-0.14		
	0.4 to 0.6	0.0167	0.0030	0.0176	0.0028	0.06	-0.24		
	0.2 to 0.4	0.0132	0.0023	0.0132	0.0023	0	-0.01		
	0.0 to 0.2	0.0102	0.0019	0.0112	0.0022	0.11	-0.34		
	-0.2 to 0.0	0.0130	0.0018	0.0139	0.0022	0.1	-0.31		
	-0.4 to -0.2	0.0097	0.0016	0.0103	0.0023	0.04	-0.2		
	-0.6 to -0.4	0.0038	0.0015	0.0047	0.0022	0.1	-0.31		
	-0.8 to -0.6	0.0012	0.0017	0.0019	0.0027	0.06	-0.24		
						0.48	-1.78	0.22	0.05

Figure C.1: Comparisons between cross sections obtained from the $\Sigma^+ \to p\pi^0$ and $\Sigma^+ \to n\pi^+$ decay channels.

photon energy (GeV)	cos theta	3.1 txs	error 3.1 TXS	2.4 TXS	error 2.4 TXS	Chi SQ	Z	stat. error	syst. error
1.55-1.75	0.6 to 0.8	0.0680	0.0052	0.0546	0.0071	2.32	1.52		
	0.4 to 0.6	0.0471	0.0038	0.0474	0.0053	0	-0.05		
	0.2 to 0.4	0.0408	0.0033	0.0422	0.0046	0.06	-0.25		
	0.0 to 0.2	0.0433	0.0032	0.0352	0.0044	2.24	1.5		
	-0.2 to 0.0	0.0309	0.0029	0.0363	0.0043	1.07	-1.04		
	-0.4 to -0.2	0.0166	0.0028	0.0213	0.0040	0.94	-0.97		
	-0.6 to -0.4	0.0098	0.0027	0.0151	0.0040	1.23	-1.11		
	-0.8 to -0.6	0.0062	0.0032	0.0103	0.0046	0.51	-0.71		
						8.37	-1.1	0.17	0.02
1.75-1.95	0.6 to 0.8	0.0302	0.0044	0.0259	0.0079	0.23	0.47		
	0.4 to 0.6	0.0318	0.0030	0.0336	0.0056	0.08	-0.29		
	0.2 to 0.4	0.0227	0.0024	0.0247	0.0042	0.16	-0.4		
	0.0 to 0.2	0.0213	0.0023	0.0245	0.0040	0.48	-0.69		
	-0.2 to 0.0	0.0153	0.0021	0.0209	0.0039	1.63	-1.28		
	-0.4 to -0.2	0.0157	0.0022	0.0170	0.0038	0.09	-0.29		
	-0.6 to -0.4	0.0031	0.0019	0.0074	0.0033	1.25	-1.12		
	-0.8 to -0.6	0.0014	0.0024	0.0041	0.0044	0.29	-0.53		
						4.2	-4.13	0.19	0.1
1.95-2.15	0.6 to 0.8	0.0207	0.0043	0.0254	0.0066	0.35	-0.59		
	0.4 to 0.6	0.0165	0.0026	0.0221	0.0040	1.33	-1.15		
	0.2 to 0.4	0.0166	0.0021	0.0169	0.0031	0.01	-0.08		
	0.0 to 0.2	0.0201	0.0020	0.0095	0.0028	9.56	3.09		
	-0.2 to 0.0	0.0176	0.0019	0.0183	0.0029	0.03	-0.18		
	-0.4 to -0.2	0.0084	0.0018	0.0136	0.0029	2.41	-1.55		
	-0.6 to -0.4	0.0028	0.0018	0.0023	0.0026	0.02	0.14		
	-0.8 to -0.6	0.0030	0.0023	0.0050	0.0031	0.26	-0.51		
						13.97	-0.83	0.29	0.03
2.15-2.35	0.6 to 0.8	0.0157	0.0040	0.0185	0.0065	0.14	-0.38		
	0.4 to 0.6	0.0162	0.0024	0.0194	0.0039	0.49	-0.7		
	0.2 to 0.4	0.0136	0.0019	0.0120	0.0030	0.21	0.46		
	0.0 to 0.2	0.0104	0.0017	0.0113	0.0026	0.08	-0.29		
	-0.2 to 0.0	0.0124	0.0017	0.0159	0.0027	1.16	-1.08		
	-0.4 to -0.2	0.0113	0.0017	0.0071	0.0025	1.92	1.38		
	-0.6 to -0.4	0.0040	0.0016	0.0048	0.0025	0.07	-0.27		
	-0.8 to -0.6	0.0013	0.0020	0.0021	0.0027	0.05	-0.23		
						4.13	-1.1	0.2	0.03

Figure C.2: Comparisons between cross sections obtained from the 2.445 and 3.115 GeV beam energy data sets.

Figures C.3 and C.4 present data used to calculate systematic errors for the sideband subtraction method used in the analysis. These results are summarized in Table 4.7 in Section 4.4.2.1.

KEY:

Selected Events = number of identified Σ^+ events

frac err = the average fractional error for each 8 point set = $\frac{1}{8}\sum_{i=1}^{8}\frac{\Delta S}{S}$

Regular = sideband subtraction method as used in the analysis, summing over 7 bins with contiguous sideband and selected event regions

9 bins = sideband subtraction method summing over 9 bins centered at the Σ^+ mass

gap = sideband subtraction method with a gap $\frac{1}{4}$ the size of the selected region between the selected and sideband regions

fit = a Gaussian fit to the peak around the Σ^+ mass

chi sq = the χ^2 value comparing the alternate method with the standard method. 8 values of χ^2 for the 8 angular bins are presented, followed by the sum of those values

Z = the Z parameter comparing the alternate method with the standard method. 8 values of Z for the 8 angular bins are presented, followed by the sum of those values

syst error = the fractional systematic error determined by multiplying the average Z value by the fractional error

K0PiP Photon Energy (GeV)	Cos Theta	Regular Selected Events	Error	frac err	9 bins Selected Events	Error	chi sq	z	syst error
1.15-1.35	0.7	87.5	26.94		115	30.32	0.46	-0.68	
	0.5	93.5	29.42		103	32.97	0.05	-0.22	
	0.3	108.5	32.12		153	36.5	0.84	-0.92	
	0.1	146	35.12		150	39.33	0.01	-0.08	
	-0.1	154.5	36.05		153	39.86	0	0.03	
	-0.3	158	34.01		187.5	37.92	0.34	-0.58	
	-0.5	110.5	31.25		151.5	35.44	0.75	-0.87	
	-0.7	103.5	28.16		108	31.3	0.01	-0.11	
				0.270			2.45	-3.41	0.115
1.35-1.55	0.7	226	27.49		217.5	30.56	0.04	0.21	
	0.5	198	30.55		195	33.94	0	0.07	
	0.3	260.5	35.54		273.5	39.07	0.06	-0.25	
	0.1	352	37.88		382	42.01	0.28	-0.53	
	-0.1	257.5	36.75		225	40.32	0.35	0.6	
	-0.3	285	33.07		291	36.52	0.01	-0.12	
	-0.5	173	28.73		181.5	31.69	0.04	-0.2	
	-0.7	115	23		113.5	25.81	0	0.04	
				0.143			0.8	-0.19	0.003
1.55-1.75	0.7	419	38.64		453	42.66	0.35	-0.59	
	0.5	404.5	44.04		421	48.8	0.06	-0.25	
	0.3	530	47.38		569	52.43	0.3	-0.55	
	0.1	547	49.02		561	54.06	0.04	-0.19	
	-0.1	479	47.07		470	52.12	0.02	0.13	
	-0.3	212	40.85		244	45.77	0.27	-0.52	
	-0.5	139	33.91		146	37.78	0.02	-0.14	
	-0.7	107.5	26.84		98	30.11	0.06	0.24	
				0.146			1.12	-1.88	0.034
1.75-1.95	0.7	146	30.68		134.5	33.83	0.06	0.25	
	0.5	266	36.3		255.5	40.25	0.04	0.19	
	0.3	256	37.68		267	41.59	0.04	-0.2	
	0.1	311	38.83		328	42.98	0.09	-0.29	
	-0.1	241	37		271.5	41.25	0.3	-0.55	
	-0.3	194.5	32.31		181.5	35.74	0.07	0.27	
	-0.5	40	25.59		46.5	28.74	0.03	-0.17	
	-0.7	14.5	21.4		20	24.26	0.03	-0.17	
				0.225			0.66	-0.66	0.019
1.95-2.15	0.7	59	27.8		80	31.18	0.25	-0.5	
	0.5	205	33.51		207.5	36.96	0	-0.05	
	0.3	239	33.08		232.5	36.83	0.02	0.13	
	0.1	244.5	33.95		265	37.66	0.16	-0.4	
	-0.1	263	33.77		290.5	37.31	0.3	-0.55	
	-0.3	129.5	28.4		124.5	31.71	0.01	0.12	
	-0.5	45	23.84		52.5	26.76	0.04	-0.21	
	-0.7	38.5	19.72		29	22.12	0.1	0.32	
				0.288			0.89	-1.14	0.041
2.15-2.35	0.7	92	20.4		81.5	22.64	0.12	0.34	
	0.5	78.5	24.55		100.5	27.48	0.36	-0.6	
	0.3	116.5	24.1		102.5	26.6	0.15	0.39	
	0.1	122.5	23.72		135	26.32	0.12	-0.35	
	-0.1	169	23.45		185.5	26.13	0.22	-0.47	
	-0.3	110.5	21.01		120.5	23.33	0.1	-0.32	
	-0.5	24	16.43		33.5	18.65	0.15	-0.38	
	-0.7	10	13.78		8.5	15.6	0.01	0.07	
				0.278		0.18	1.23	-1.31	0.046

Figure C.3: Comparisons between standard event selection and alternate methods for the $\Sigma^+ \to p\pi^0$ decay channel. (2 pages)

K0PiP Photon Energy (GeV)	Cos Theta	Gap Selected Events	Error	chi2	z	syst err	Fit Selected Events	Error	chi2	z	syst err
1.15-1.35	0.7	94	26.88	0.03	-0.17		46.4	46.4	0.59	0.77	
	0.5	109.5	29.28	0.15	-0.39		82.9	31.4	0.06	0.25	
	0.3	100	32.19	0.03	0.19		43.3	43.3	1.46	1.21	
	0.1	160.5	35.02	0.09	-0.29		132.1	39.9	0.07	0.26	
	-0.1	164.5	35.98	0.04	-0.2		180.4	41.9	0.22	-0.47	
	-0.3	181.5	33.84	0.24	-0.49		127.1	45.1	0.3	0.55	
	-0.5	139.5	31.02	0.43	-0.66		55.1	46.7	0.97	0.99	
	-0.7	118	28.03	0.13	-0.36		99.2	5.3	0.02	0.15	
				1.14	-2.37	0.08			3.69	3.7	0.125
1.35-1.55	0.7	212.5	27.61	0.12	0.35		230.3	42.7	0.01	-0.08	
	0.5	211.5	30.43	0.1	-0.31		208.8	47.4	0.04	-0.19	
	0.3	301	35.26	0.65	-0.81		278.4	54.7	0.08	-0.27	
	0.1	374	37.74	0.17	-0.41		402.4	58.8	0.52	-0.72	
	-0.1	287	36.54	0.32	-0.57		271.9	50.7	0.05	-0.23	
	-0.3	289.5	33.03	0.01	-0.1		277.6	53.6	0.01	0.12	
	-0.5	182.5	28.65	0.05	-0.23		172	41.5	0	0.02	
	-0.7	117	22.98	0	-0.06		115.5	30.6	0	-0.01	
				1.43	-2.15	0.04			0.71	-1.38	0.025
1.55-1.75	0.7	415	38.67	0.01	0.07		441.5	66.4	0.09	-0.29	
	0.5	449.5	43.79	0.53	-0.72		437.4	68.4	0.16	-0.4	
	0.3	525.5	47.4	0	0.07		568.8	97.7	0.13	-0.36	
	0.1	565	48.92	0.07	-0.26		559.7	77.9	0.02	-0.14	
	-0.1	482.5	47.06	0	-0.05		500.2	67.7	0.07	-0.26	
	-0.3	260	40.55	0.7	-0.83		204.8	50.3	0.01	0.11	
	-0.5	161	33.75	0.21	-0.46		130.7	42.5	0.02	0.15	
	-0.7	101	26.9	0.03	0.17		89.5	58.4	0.08	0.28	
				1.54	-2.02	0.04			0.58	-0.91	0.016
1.75-1.95	0.7	145.5	30.68	0	0.01		168.6	45.3	0.17	-0.41	
	0.5	268	36.28	0	-0.04		300.4	50.8	0.3	-0.55	
	0.3	283	37.5	0.26	-0.51		307.9	53.6	0.63	-0.79	
	0.1	321.5	38.77	0.04	-0.19		318.8	65.7	0.01	-0.1	
	-0.1	238	37.02	0	0.06		214.5	42.9	0.22	0.47	
	-0.3	186	32.38	0.03	0.19		209.4	45.9	0.07	-0.27	
	-0.5	51.5	25.48	0.1	-0.32		54.3	41.6	0.09	-0.29	
	-0.7	9.5	21.45	0.03	0.17		26.9	20.7	0.17	-0.42	
				0.46	-0.64	0.02			1.66	-2.37	0.067
1.95-2.15	0.7	54.5	27.84	0.01	0.11		90.7	26.5	0.68	-0.83	
	0.5	200	33.55	0.01	0.11		178.4	43.6	0.23	0.48	
	0.3	223	33.2	0.12	0.34		174.7	41.7	1.46	1.21	
	0.1	238	34	0.02	0.14		198.6	50.1	0.58	0.76	
	-0.1	272.5	33.7	0.04	-0.2		213.7	62.5	0.48	0.69	
	-0.3	131	28.39	0	-0.04		157.1	50.9	0.22	-0.47	
	-0.5	59	23.7	0.17	-0.42		44.9	41.7	0	0	
	-0.7	37	19.74	0	0.05		51.8	30.9	0.13	-0.36	
				0.38	0.1	0			3.79	1.48	0.053
2.15-2.35	0.7	93.5	20.38	0	-0.05		14	14	9.94	3.15	
	0.5	99	24.34	0.35	-0.59		107.3	40.3	0.37	-0.61	
	0.3	128.5	23.97	0.12	-0.35		95.7	33.3	0.26	0.51	
	0.1	125.5	23.69	0.01	-0.09		89.9	47.9	0.37	0.61	
	-0.1	170	23.44	0	-0.03		148.3	43.7	0.17	0.42	
	-0.3	117.5	20.92	0.06	-0.24		116.5	29.9	0.03	-0.16	
	-0.5	17.5	16.53	0.08	0.28		18.8	20.1	0.04	0.2	
	-0.7	3.5	13.9	0.11	0.33		6	10.8	0.05	0.23	
			0.26	0.73	-0.74	0.03		0.33	11.24	1.19	0.047
									11.24		

K0PiN	Cos Theta	Regular Selected Events	Error		9 bins Selected Events	Error			
Energy									
1.15-1.35	0.7	56.5	20.46		52.5	23.03	0.02	0.13	
	0.5	58.5	20.98		51.5	23.36	0.05	0.22	
	0.3	59	21.37		81	24.34	0.46	-0.68	
	0.1	45	21.25		34	23.58	0.12	0.35	
	-0.1	79	20.26		73	22.51	0.04	0.2	
	-0.3	85.5	18.83		86	20.65	0	-0.02	
	-0.5	45	16.7		64.5	18.72	0.6	-0.78	
	-0.7	26	14.35		28.5	16.09	0.01	-0.12	
				0.369			1.31	-0.69	0.032
1.35-1.55	0.7	123.5	23.36		135	25.81	0.11	-0.33	
	0.5	144.5	24.52		140	27.04	0.02	0.12	
	0.3	182	26.11		197	28.73	0.15	-0.39	
	0.1	115.5	24.39		135.5	27.19	0.3	-0.55	
	-0.1	140.5	23.21		146	25.61	0.03	-0.16	
	-0.3	102.5	20.04		105.5	22.04	0.01	-0.1	
	-0.5	71	16.22		70.5	17.64	0	0.02	
	-0.7	51	13.53		58.5	14.92	0.14	-0.37	
				0.196			0.75	-1.75	0.043
1.55-1.75	0.7	408	31.94		379.5	34.48	0.37	0.61	
	0.5	359	33.99		362.5	37.19	0	-0.07	
	0.3	348.5	35.75		377.5	38.91	0.3	-0.55	
	0.1	352.5	34.59		362.5	38.03	0.04	-0.19	
	-0.1	239.5	30		242	32.92	0	-0.06	
	-0.3	125.5	24.38		108.5	26.66	0.22	0.47	
	-0.5	58.5	18.31		58	20.15	0	0.02	
	-0.7	16	13.56		18	15.15	0.01	-0.1	
				0.144			0.95	0.13	0.002
1.75-1.95	0.7	97.5	21.55		87.5	23.9	0.1	0.31	
	0.5	220.5	25.94		221.5	28.52	0	-0.03	
	0.3	194.5	26.7		198.5	29.24	0.01	-0.1	
	0.1	172	26.32		174.5	28.77	0	-0.06	
	-0.1	143.5	22.32		153	24.65	0.08	-0.29	
	-0.3	114.5	18.97		108.5	20.78	0.05	0.21	
	-0.5	0	12.32		0	13.65	0	0	
	-0.7	0	9.37		0	10.68	0	0	
				0.158			0.24	0.05	0.0009
1.95-2.15	0.7	66	17.92		68	19.91	0.01	-0.07	
	0.5	141.5	22.61		137	24.66	0.02	0.13	
	0.3	180	24.22		201	26.86	0.34	-0.58	
	0.1	165.5	23.33		179	25.52	0.15	-0.39	
	-0.1	156.5	21.56		158	23.18	0	-0.05	
	-0.3	76.5	15.9		86	17.42	0.16	-0.4	
	-0.5	0	10.89		12	12.67	0.52	-0.72	
	-0.7	9	8.92		7	9.77	0.02	0.15	
				0.175			1.22	-1.93	0.042
2.15-2.35	0.7	46.5	12.93		59.5	14.29	0.45	-0.67	
	0.5	84	16.52		82.5	17.77	0	0.06	
	0.3	87.5	17.31		90.5	18.89	0.01	-0.12	
	0.1	82.5	16.68		82.5	18.27	0	0	
	-0.1	84.5	15.39		82	16.6	0.01	0.11	
	-0.3	44.5	11.95		42	12.67	0.02	0.14	
	-0.5	7.5	7.98		0	8.75	0.4	0.63	
	-0.7	1	5.96		0.5	6.34	0		
				0.221			0.91	0.16	0.004

Figure C.4: Comparisons between standard event selection and alternate methods for the $\Sigma^+ \to n\pi^+$ decay channel.(2 pages)

K0PiN Energy	Cos Theta	Gap Selected Events	Error				Fit Selected Events	Error			
1.15-1.35	0.7	78.5	20.19	0.59	-0.77		46.4	15.6	0.15	0.39	
	0.5	63	20.93	0.02	-0.15		45.4	27.9	0.14	0.38	
	0.3	54.5	21.42	0.02	0.15		61.9	22.8	0.01	-0.09	
	0.1	55	21.13	0.11	-0.33		88.5	23.6	1.88	-1.37	
	-0.1	79.5	20.25	0	-0.02		96	17.2	0.41	-0.64	
	-0.3	97.5	18.67	0.2	-0.45		96.9	38.3	0.07	-0.27	
	-0.5	56.5	16.53	0.24	-0.49		49.5	19.9	0.03	-0.17	
	-0.7	34	14.21	0.16	-0.4		30.9	13.2	0.06	-0.25	
				1.34	-2.46	0.11			2.75	-2.03	0.094
1.35-1.55	0.7	139.5	23.19	0.24	-0.49		131.9	26.9	0.06	-0.24	
	0.5	161	24.35	0.23	-0.48		142.1	21.3	0.01	0.07	
	0.3	190	26.03	0.05	-0.22		157.4	27.8	0.42	0.65	
	0.1	112.5	24.42	0.01	0.09		132.8	25.9	0.24	-0.49	
	-0.1	139.5	23.22	0	0.03		136.1	27.6	0.01	0.12	
	-0.3	98	20.1	0.03	0.16		90.5	22	0.16	0.4	
	-0.5	68	16.26	0.02	0.13		68.5	19.7	0.01	0.1	
	-0.7	54	13.47	0.02	-0.16		73.5	72.9	0.09	-0.3	
				0.59	-0.93	0.02			0.99	0.32	0.008
1.55-1.75	0.7	409.5	31.93	0	-0.03		371.7	47.8	0.4	0.63	
	0.5	372.5	33.89	0.08	-0.28		339	48.9	0.11	0.34	
	0.3	337.5	35.82	0.05	0.22		343.4	50.9	0.01	0.08	
	0.1	358	34.55	0.01	-0.11		282.1	48.2	1.41	1.19	
	-0.1	244	29.97	0.01	-0.11		211.8	35.3	0.36	0.6	
	-0.3	125.5	24.38	0	0		135.4	114.7	0.01	-0.08	
	-0.5	66	18.21	0.08	-0.29		67.5	85.9	0.01	-0.1	
	-0.7	20	13.49	0.04	-0.21		21.3	14.3	0.07	-0.27	
				0.28	-0.82	0.01			2.37	1.19	0.024
1.75-1.95	0.7	100	21.52	0.01	-0.08		83.3	35.1	0.12	0.34	
	0.5	225	25.89	0.02	-0.12		207.4	40.3	0.07	0.27	
	0.3	195.5	26.69	0	-0.03		161.7	26.5	0.76	0.87	
	0.1	183	26.21	0.09	-0.3		183.7	20.7	0.12	-0.35	
	-0.1	142.5	22.33	0	0.03		140.6	25.6	0.01	0.09	
	-0.3	115.5	18.95	0	-0.04		101.9	17.7	0.24	0.49	
	-0.5	3	12.12	0.03	-0.17		15.5	20.3	0.43	-0.65	
	-0.7	0	9.29	0	0		52.8	30.1	2.81	-1.67	
				0.14	-0.71	0.01			4.55	-0.62	0.012
1.95-2.15	0.7	69.5	17.87	0.02	-0.14		58.9	14.2	0.1	0.31	
	0.5	142.5	22.6	0	-0.03		145.1	33.4	0.01	-0.09	
	0.3	179.5	24.22	0	0.01		156.5	52.2	0.17	0.41	
	0.1	160	23.39	0.03	0.17		165.4	23.3	0	0	
	-0.1	164	21.47	0.06	-0.25		150.4	22.9	0.04	0.19	
	-0.3	76	15.91	0	0.02		64.4	23.3	0.18	0.43	
	-0.5	0	10.9	0	0		0.3	0.3	0	-0.03	
	-0.7	8.5	8.93	0	0.04		17.6	14	0.27	-0.52	
				0.11	-0.17	0			0.76	0.71	0.016
2.15-2.35	0.7	42	13.02	0.06	0.25		48.2	18.2	0.01	-0.08	
	0.5	102.5	16.24	0.64	-0.8		86.3	22.3	0.01	-0.08	
	0.3	93	17.23	0.05	-0.23		77.6	35.4	0.06	0.25	
	0.1	80.5	16.71	0.01	0.08		77.1	27	0.03	0.17	
	-0.1	82	15.43	0.01	0.11		83.7	23.7	0	0.03	
	-0.3	43	11.98	0.01	0.09		60.2	40.5	0.14	-0.37	
	-0.5	7.5	7.98	0	0		7.9	7.9	0	-0.04	
	-0.7	1	5.96	0	0		6.1	6.9	0.31	-0.56	
				0.78	-0.49	0.01			0.56	-0.68	0.019

Figure C.5 presents data used to compare different ranges in laboratory angle of the K_S^0 and to calculate systematic errors in the acceptance. These results are summarized in Table 4.11 in Section 4.4.2.4.

KEY:

S7 = the number of identified Σ^+ events from experimental data for the given angular range determined from a sideband subtraction

DS7 = the statistical error in the number of identified Σ^+ events

ACYield = the acceptance corrected yield, calculated by multiplying the acceptance by the number of identified Σ^+ events

DACY = the error in the acceptance corrected yield

stat err = the average fractional error for each 8 point set = $\frac{1}{8}\sum_{i=1}^{8}\frac{\Delta S}{S}$

Gsim K0S = the number of identified Σ^+ events from simulated $\gamma p \rightarrow \mathrm{K}^0\Sigma^+$ events

gen events = the number of $\gamma p \rightarrow \mathrm{K}^0\Sigma^+$ events generated

acc = the acceptance, calculated by dividing Gsim K0s by gen events

chi sq 1 v 2= the χ^2 value comparing two sets of results, here from angular ranges 1 and 2. 8 values of χ^2 for the 8 angular bins are presented, followed by the sum of those values

Z 1 2 = the Z parameter comparing two sets of results, here from angular ranges 1 and 2. 8 values of Z for the 8 angular bins are presented, followed by the sum of those values

syst error = the fractional systematic error determined by multiplying the average Z value by the fractional error

lab angle 1 = -30° to 90°

lab angle 2 = 90° to 210°

lab angle 3 = 210° to 330°

Photon Energy (GeV)	cos theta	lab angle 1	S7	Ds7	ACYield	DACY	stat err	gsim k0s	error k0s	gen events	del gen events	Acc	D acc
1.15-1.35	0.7		20.5	15.45	339.75	256.26	0.75	1432	38.53	23733	154.06	0.060	0.002
	0.5		20.5	16.67	261.78	212.92	0.81	1838	43.55	23471	153.2	0.078	0.002
	0.3		16.5	18.47	195.63	219.07	1.12	1986	45.38	23547	153.45	0.084	0.002
	0.1		46.5	19.69	535.2	226.99	0.42	2064	46.33	23756	154.13	0.087	0.002
	-0.1		8	20.17	89.19	224.92	2.52	2124.5	47	23685	153.9	0.090	0.002
	-0.3		66	19.17	740.92	215.9	0.29	2085.5	46.51	23412	153.01	0.089	0.002
	-0.5		30	17.19	363.86	208.68	0.57	1914	44.67	23214	152.36	0.082	0.002
	-0.7		34	15.67	454.37	209.71	0.46	1745	42.66	23320	152.71	0.075	0.002
							0.55						
1.35-1.55	0.7		83.5	16.26	1404.14	276.12	0.2	1413	38.12	23761	154.15	0.059	0.002
	0.5		111.5	18.53	1285.31	215.65	0.17	2059	45.92	23735	154.06	0.087	0.002
	0.3		54.5	19.32	510.01	181.12	0.36	2515.5	50.87	23540	153.43	0.107	0.002
	0.1		88.5	21.41	762.89	185.19	0.24	2733	53.17	23559	153.49	0.116	0.002
	-0.1		107	20.69	916.73	178.23	0.19	2769.5	53.5	23728	154.04	0.117	0.002
	-0.3		95.5	18.34	835.33	161.32	0.19	2695	52.73	23573	153.54	0.114	0.002
	-0.5		38.5	15.84	394.95	162.68	0.41	2256	48.37	23143	152.13	0.097	0.002
	-0.7		57.5	12.78	776.13	173.58	0.22	1727	42.27	23311	152.68	0.074	0.002
							0.25						
1.55-1.75	0.7		47	13.55	774.7	224.31	0.29	1428.5	38.45	23546	153.45	0.061	0.002
	0.5		61	15.62	624.2	160.44	0.26	2289	48.48	23423	153.05	0.098	0.002
	0.3		80	17.07	644.03	138.04	0.21	2938.5	55.05	23656	153.81	0.124	0.002
	0.1		40.5	16.86	296.26	123.46	0.42	3254.5	57.85	23807	154.3	0.137	0.003
	-0.1		49	16.55	348.75	117.99	0.34	3335.5	58.59	23740	154.08	0.141	0.003
	-0.3		32	13.98	236.86	103.6	0.44	3157	57.25	23368	152.87	0.135	0.003
	-0.5		14	11.18	119.05	95.1	0.8	2763.5	53.31	23500	153.3	0.118	0.002
	-0.7		22	9.92	248.5	112.25	0.45	2062.5	46.16	23297	152.63	0.089	0.002
							0.4						
1.75-1.95	0.7		22.5	10.28	380.79	174.36	0.46	1404	37.89	23761	154.15	0.059	0.002
	0.5		21	11.75	202.16	113.17	0.56	2465.5	50.26	23735	154.06	0.104	0.002
	0.3		10.5	11.78	77.91	87.42	1.12	3197	57.37	23722	154.02	0.135	0.003
	0.1		18	13.02	120.43	87.13	0.72	3536	60.24	23658	153.81	0.149	0.003
	-0.1		22	11.92	142.75	77.36	0.54	3628.5	61.13	23544	153.44	0.154	0.003
	-0.3		22.5	10.21	154.59	70.21	0.45	3448.5	59.59	23693	153.93	0.146	0.003
	-0.5		10	8.28	80.14	66.35	0.83	2898.5	54.61	23228	152.41	0.125	0.002
	-0.7		5	6.63	57.39	76.15	1.33	2026.5	45.69	23262	152.52	0.087	0.002
							0.67						
1.95-2.15	0.7		12	9.72	229.53	186.07	0.81	1243	35.72	23776	154.19	0.052	0.002
	0.5		22	11.4	201.99	104.77	0.52	2518	50.98	23119	152.05	0.109	0.002
	0.3		26.5	11.3	185.51	79.2	0.43	3383.5	59.07	23686	153.9	0.143	0.003
	0.1		22.5	10.85	135.75	65.51	0.48	3893.5	63.14	23491	153.27	0.166	0.003
	-0.1		27	11.68	149.55	64.76	0.43	4268	66.11	23640	153.75	0.181	0.003
	-0.3		20	9.59	127.02	60.96	0.48	3710.5	61.68	23565	153.51	0.157	0.003
	-0.5		5.5	8.5	41.06	63.46	1.55	3139.5	56.76	23439	153.1	0.134	0.003
	-0.7		2	6.16	20.51	63.22	3.08	2293	48.49	23517	153.35	0.098	0.002
							0.53						
2.15-2.35	0.7		13	7.11	250.53	137.17	0.55	1115	33.79	21488	146.59	0.052	0.002
	0.5		31.5	9.29	293.85	86.88	0.3	2256.5	48.06	21050	145.09	0.107	0.002
	0.3		17	8.51	117.7	59	0.5	3086.5	56.17	21370	146.18	0.144	0.003
	0.1		9	7.65	55.44	47.12	0.85	3451	59.51	21257	145.8	0.162	0.003
	-0.1		25	8.19	140.78	46.16	0.33	3792	62.23	21354	146.13	0.178	0.003
	-0.3		3.5	6.58	20.02	37.61	1.88	3686.5	61.31	21082	145.2	0.175	0.003
	-0.5		7	5.96	49.17	41.86	0.85	2997	55.41	21050	145.09	0.142	0.003
	-0.7		0	4.58	0	0	0	2135.5	46.72	21105	145.28	0.101	0.002
							0.5						

Figure C.5: Comparisons between acceptance corrected yields in three regions of laboratory azimuthal angle of the K_S^0, for the $\Sigma^+ \to p\pi^0$ decay channel. (3 pages)

Photon Energy (GeV)	cos lab theta angle 2	S7	Ds7	ACYield	DACY	stat err	Chi 2 1 v 2	Z 1 v 2	stat err	syst err	gsim k0s	error k0s	gen events	error gen events	Acc	error acc	Chi 2 1 v 2	z 1 v 2
1.15-1.35	0.7	31.5	16.23	471.98	243.42	0.52	0.14	-0.37			1598.5	40.7	23951	154.76	0.067	0.002	6.99	2.64
	0.5	28	17.65	345.05	217.66	0.63	0.07	-0.27			1900	44.36	23414	153.02	0.081	0.002	1.06	1.03
	0.3	33.5	18.61	365.23	203.04	0.56	0.32	-0.57			2195	47.6	23931	154.7	0.092	0.002	6.54	2.56
	0.1	9	7.65	61.16	51.99	0.85	4.14	2.04			3451	59.51	23451	153.14	0.147	0.003	316.37	17.79
	-0.1	57	21.21	589.93	219.94	0.37	2.53	-1.59			2288.5	48.81	23685	153.9	0.097	0.002	5.38	2.32
	-0.3	81.5	20.19	837.71	208.38	0.25	0.1	-0.32			2311.5	49	23759	154.14	0.097	0.002	7.55	2.75
	-0.5	41.5	18.62	476.71	214.19	0.45	0.14	-0.38			2088	46.69	23985	154.87	0.087	0.002	2.62	1.62
	-0.7	22.5	15.95	309.46	219.45	0.71	0.23	0.48			1705	42.28	23450	153.13	0.073	0.002	0.64	-0.8
						0.54	7.69	-0.99	0.55	0.07							347.14	3.74
1.35-1.55	0.7	68.5	16.44	1024.21	247.25	0.24	1.05	1.03			1603	40.5	23968	154.82	0.067	0.002	9.53	3.09
	0.5	70	17.99	785.04	202.52	0.26	2.86	1.69			2106.5	46.68	23624	153.7	0.089	0.002	0.7	0.84
	0.3	131	21.54	1198.84	198.7	0.17	6.56	-2.56			2631.5	52.12	24082	155.18	0.109	0.002	0.56	0.75
	0.1	97	21.38	777.66	172.09	0.22	0	-0.06			2921.5	54.99	23422	153.04	0.125	0.002	6.43	2.54
	-0.1	73.5	21.12	588.65	169.58	0.29	1.78	1.33			2962	55.26	23722	154.02	0.125	0.002	5.65	2.38
	-0.3	89.5	19.53	730.41	160.02	0.22	0.21	0.46			2887.5	54.67	23565	153.51	0.123	0.002	5.82	2.41
	-0.5	78	16.52	730.1	155.43	0.21	2.22	-1.49			2535.5	51.12	23733	154.06	0.107	0.002	8.84	2.97
	-0.7	20.5	12.8	252.16	157.52	0.62	5	2.24			1922	44.64	23642	153.76	0.081	0.002	7.06	2.66
						0.28	19.69	2.64	0.25	0.08							44.59	2.2
1.55-1.75	0.7	48	13.86	711	206.09	0.29	0.04	0.21			1603.5	40.56	23752	154.12	0.068	0.002	7.89	2.81
	0.5	50	15.84	490.23	155.69	0.32	0.36	0.6			2414.5	49.84	23673	153.86	0.102	0.002	1.91	1.38
	0.3	67	16.87	506.84	127.97	0.25	0.53	0.73			3150.5	56.87	23833	154.38	0.132	0.003	5.09	2.26
	0.1	76.5	17.26	521.5	118.02	0.23	1.74	-1.32			3449.5	59.64	23515	153.35	0.147	0.003	7.11	2.67
	-0.1	58.5	16.82	375.08	108.02	0.29	0.03	-0.16			3714.5	61.71	23816	154.32	0.156	0.003	16.32	4.04
	-0.3	36	14.59	248.74	100.95	0.41	0.01	-0.08			3401	59.29	23499	153.29	0.145	0.003	6.61	2.57
	-0.5	12	11.62	93.15	90.21	0.97	0.04	0.2			3058.5	56.17	23742	154.08	0.129	0.003	10.48	3.24
	-0.7	9	9.08	95.55	96.45	1.01	1.07	1.03			2228	47.91	23653	153.8	0.094	0.002	3.67	1.92
						0.47	3.81	1.2	0.4	0.06							59.07	2.61
1.75-1.95	0.7	18.5	10.45	334.32	189.13	0.57	0.03	0.18			1317	36.84	23800	154.27	0.055	0.002	2.7	-1.64
	0.5	6	11.62	53.74	104.07	1.94	0.93	0.97			2617.5	51.8	23444	153.11	0.112	0.002	5.84	2.42
	0.3	40	12.53	277.02	86.93	0.31	2.61	-1.62			3469.5	59.74	24028	155.01	0.144	0.003	6.78	2.6
	0.1	40.5	12.7	243.25	76.39	0.31	1.12	-1.06			3899	63.15	23418	153.03	0.166	0.003	18.27	4.27
	-0.1	13	11.85	75.63	68.97	0.91	0.42	0.65			4080.5	64.65	23739	154.07	0.172	0.003	19.25	4.39
	-0.3	19.5	10.71	119.77	65.83	0.55	0.13	0.36			3826	62.6	23500	153.3	0.163	0.003	19.29	4.39
	-0.5	15	8.12	106.74	57.85	0.54	0.09	-0.3			3346	58.35	23811	154.31	0.141	0.003	19.01	4.36
	-0.7	0	6.86	0	70.53	68556.5	0.31	0.55			2305	48.62	23712	153.99	0.097	0.002	11.59	3.4
						0.73	5.64	-0.27	0.67	0.02							102.72	3.02
1.95-2.15	0.7	14	9.27	246.23	163.25	0.66	0	-0.07			1358.5	37.31	23893	154.57	0.057	0.002	4.24	2.06
	0.5	27.5	11.74	236.86	101.21	0.43	0.06	-0.24			2733.5	52.96	23544	153.44	0.116	0.002	4.69	2.17
	0.3	6	10.61	39.48	69.79	1.77	1.91	1.38			3632	60.95	23897	154.59	0.152	0.003	5.74	2.4
	0.1	24	11.62	133.78	64.81	0.48	0	0.02			4205	65.57	23440	153.1	0.179	0.003	10.59	3.25
	-0.1	46.5	12.46	251.5	67.52	0.27	1.19	-1.09			4362.5	66.82	23595	153.61	0.185	0.003	1.01	1.01
	-0.3	23.5	10.26	134.62	58.82	0.44	0.01	-0.09			4101	64.77	23493	153.27	0.175	0.003	17.41	4.17
	-0.5	3	7.84	19.68	51.45	2.61	0.07	0.26			3626.5	60.93	23791	154.24	0.152	0.003	24.13	4.91
	-0.7	9	6.25	85.69	59.49	0.69	0.56	-0.75			2486	50.55	23669	153.85	0.105	0.002	5.85	2.42
						0.92	3.8	-0.57	0.53	0.04							73.67	2.8
2.15-2.35	0.7	10	7.21	175.54	126.69	0.72	0.16	0.4			1221	35.33	21434	146.4	0.057	0.002	4.71	2.17
	0.5	16	8.97	129.99	72.94	0.56	2.09	1.44			2627.5	51.85	21347	146.11	0.123	0.003	20.41	4.52
	0.3	9.5	7.53	63.76	50.57	0.79	0.48	0.69			3213	57.34	21563	146.84	0.149	0.003	1.31	1.14
	0.1	22.5	8.53	129.53	49.16	0.38	1.18	-1.09			3646.5	61.05	20992	144.89	0.174	0.003	6.81	2.61
	-0.1	16.5	8.26	87.12	43.65	0.5	0.71	0.84			4059	64.44	21432	146.4	0.189	0.003	6.75	2.6
	-0.3	16	7.42	85.79	39.79	0.46	1.44	-1.2			3928.5	63.43	21063	145.13	0.187	0.003	6.58	2.56
	-0.5	2	5.66	12.25	34.64	2.83	0.46	0.68			3478.5	59.58	21301	145.95	0.163	0.003	25.81	5.08
	-0.7	9	6.25	77.57	53.85	0.69	2.07	-1.44			2486	50.55	21427	146.38	0.116	0.002	19.01	4.36
						0.87	8.61	0.33	0.5	0.02							91.38	3.13

Photon Energy (GeV)	cos theta	lab angle 3	S7	Ds7	ACYield	DACY	stat err yield	Chi 2 2 v 3	z 2 v 3	frac err yield	syst err 2 v 3	Chi 2 1 v 3	z 1 v 3	stat err	syst err 1 v 3	chi 2 1 v 2	z 1 v 2	gsim k0s	error k0s	Gen Events	Del Gen ev	Acc	D acc	Chi 2 2 v 3	z 2 v 3	syst err 2 v 3
1.15-1.35	0.7		36	16.34	593.29	269.79	0.45	0.11	-0.33			0.46	-0.68			0.14	-0.37	1428.5	38.51	23542	153.43	0.061	0.002	6.22	-2.49	
	0.5		38.5	17.28	481.11	216.31	0.45	0.2	-0.44			0.52	-0.72			0.07	-0.27	1883.5	44.26	23537	153.42	0.080	0.002	0.16	-0.41	
	0.3		57.5	19.05	654.51	217.34	0.33	0.95	-0.97			2.21	-1.49			0.32	-0.57	2054.5	46.15	23386	152.92	0.088	0.002	1.76	-1.32	
	0.1		86.5	20.5	907.92	216.15	0.24	14.51	-3.81			1.41	-1.19			4.14	2.04	2231	48.21	23417	153.03	0.095	0.002	224.57	-14.99	
	-0.1		74.5	21.15	787.9	224.36	0.28	0.4	-0.63			4.84	-2.2			2.53	-1.59	2252.5	48.39	23822	154.34	0.095	0.002	0.47	-0.68	
	-0.3		46	19.47	483.37	204.85	0.42	1.47	1.21			0.75	0.87			0.1	-0.32	2260	48.45	23748	154.1	0.095	0.002	0.49	-0.7	
	-0.5		27.5	17.53	309.67	197.51	0.64	0.33	0.57			0.04	0.19			0.14	-0.38	2087	46.56	23501	153.3	0.089	0.002	0.37	0.61	
	-0.7		40.5	15.85	524.03	205.51	0.39	0.51	-0.71			0.06	-0.24			0.23	0.48	1823	43.48	23588	153.58	0.077	0.002	2.94	1.71	
							0.4	18.47	-1.31	0.4	0.08	10.29	-3.98	0.55	0.31	7.69	-0.99							236.97	-0.41	0.01
1.35-1.55	0.7		55.5	16.23	851.53	249.97	0.29	0.24	0.49			2.2	1.48			1.05	1.03	1541.5	39.75	23651	153.79	0.065	0.002	0.48	-0.69	
	0.5		33.5	17.4	363.61	189.04	0.52	2.31	1.52			10.33	3.21			2.86	1.69	2164	47.18	23488	153.26	0.092	0.002	1.02	1.01	
	0.3		100	20.66	930.57	193.31	0.21	0.94	0.97			2.52	-1.59			6.56	-2.56	2520.5	50.97	23455	153.15	0.107	0.002	0.32	-0.56	
	0.1		105.5	21.9	863.72	180.15	0.21	0.12	-0.35			0.15	-0.39			0	-0.06	2889	54.59	23652	153.79	0.122	0.002	0.55	-0.74	
	-0.1		78.5	21.35	651.01	177.52	0.27	0.06	-0.25			1.12	1.06			1.78	1.33	2886.5	54.67	23938	154.72	0.121	0.002	1.54	-1.24	
	-0.3		105	18.89	878.25	159.02	0.18	0.43	-0.66			0.04	-0.19			0.21	0.46	2847	54.28	23813	154.31	0.120	0.002	0.75	-0.87	
	-0.5		72.5	16.96	670.26	157.46	0.23	0.07	0.27			1.48	-1.22			2.22	-1.49	2541.5	51.2	23496	153.28	0.108	0.002	0.17	0.41	
	-0.7		51	13.53	610.84	162.67	0.27	2.51	-1.58			0.48	0.69			5	2.24	1983	45.15	23751	154.11	0.083	0.002	0.62	0.79	
							0.27	6.69	0.41	0.27	0.01	18.32	3.07	0.25	0.1	19.69	2.64							5.45	-1.15	0.02
1.55-1.75	0.7		30	14.02	471.86	220.84	0.47	0.63	0.79			0.93	0.96			0.04	0.21	1515.5	39.36	23837	154.39	0.064	0.002	2.58	-1.6	
	0.5		70	16.55	683.75	162.36	0.24	0.74	-0.86			0.07	-0.26			0.36	0.6	2416	49.76	23599	153.62	0.102	0.002	0.02	0.12	
	0.3		56.5	16.67	429.26	126.89	0.3	0.19	0.43			1.31	1.15			0.53	0.73	3088.5	56.34	23465	153.18	0.132	0.003	0.03	-0.16	
	0.1		62.5	17.54	424.28	119.34	0.28	0.34	0.58			0.56	-0.75			1.74	-1.32	3485.5	59.96	23661	153.82	0.147	0.003	0.03	0.16	
	-0.1		55.5	16.45	358.58	106.51	0.3	0.01	0.11			0	-0.06			0.03	-0.16	3614	60.8	23350	152.81	0.155	0.003	0.09	-0.3	
	-0.3		52	15.13	354.22	103.29	0.29	0.53	-0.73			0.64	-0.8			0.01	-0.08	3475.5	59.82	23675	153.87	0.147	0.003	0.29	0.54	
	-0.5		24.5	12.42	187.74	95.24	0.51	0.52	-0.72			0.26	-0.51			0.04	0.2	3078	56.12	23586	153.58	0.131	0.003	0.22	0.47	
	-0.7		15.5	8.99	168.62	97.83	0.58	0.28	-0.53			0.29	0.54			1.07	1.03	2147	46.98	23357	152.83	0.092	0.002	0.58	-0.76	
							0.37	3.24	-0.93	0.37	0.04	4.06	0.26	0.4	0.01	3.81	1.2							3.83	-1.69	0.03
1.75-1.95	0.7		0	9.64	0	161.6	96436.5	1.81	1.34			2.57	1.6			0.03	0.18	1398	37.87	23427	153.06	0.060	0.002	3.56	1.89	
	0.5		17.5	11.76	163.24	109.74	0.67	0.52	-0.72			0.06	0.25			0.93	0.97	2520	50.82	23507	153.32	0.107	0.002	1.87	-1.37	
	0.3		30.5	11.41	214.73	80.45	0.37	0.28	0.53			1.33	-1.15			2.61	-1.62	3339.5	58.62	23511	153.33	0.142	0.003	0.39	-0.63	
	0.1		28	12.65	165.62	74.88	0.45	0.53	0.73			0.15	-0.39			1.12	-1.06	3969	63.8	23477	153.22	0.169	0.003	0.39	0.62	
	-0.1		0	11.42	0	66.54	114237	0.62	0.79			1.96	1.4			0.42	0.65	4044	64.34	23556	153.48	0.172	0.003	0	-0.05	
	-0.3		33.5	11.15	200.85	66.92	0.33	0.75	-0.86			0.23	-0.48			0.13	0.36	3914.5	63.38	23470	153.2	0.167	0.003	0.95	0.97	
	-0.5		24	8.4	160.56	56.25	0.35	0.44	-0.67			0.85	-0.92			0.09	-0.3	3519	59.94	23542	153.43	0.149	0.003	5.62	2.37	
	-0.7		3	7.04	29.21	68.51	2.35	0	-0.3			0.08	0.28			0.31	0.55	2440	50.13	23759	154.14	0.103	0.002	3.17	1.78	
							0.44	4.95	0.83	0.44	0.05	7.22	0.58	0.67	0.05	5.64	-0.27							15.95	4.97	0.09
1.95-2.15	0.7		28	10.72	494.64	189.97	0.38	0.98	-0.99			0.99	-1			0	-0.07	1328	36.95	23460	153.17	0.057	0.002	0.01	-0.11	
	0.5		27.5	11.28	239.83	98.5	0.41	0	-0.02			0.07	-0.26			0.06	-0.24	2704	52.59	23582	153.56	0.115	0.002	0.19	-0.43	
	0.3		28.5	11.84	189.19	78.69	0.42	2.03	-1.42			0	-0.03			1.91	1.38	3512	59.93	23313	152.69	0.151	0.003	0.12	-0.35	
	0.1		24.5	11.28	138.46	63.8	0.46	0	-0.05			0	-0.03			0	0.02	4150	65.14	23454	153.15	0.177	0.003	0.33	-0.57	
	-0.1		36.5	11.54	190.67	60.38	0.32	0.45	0.67			0.22	-0.46			1.19	-1.09	4564.5	68.49	23844	154.42	0.191	0.003	2.22	1.49	
	-0.3		11	9.35	60.84	51.75	0.85	0.89	0.94			0.68	0.83			0.01	-0.09	4279.5	66.19	23670	153.85	0.181	0.003	2.15	1.47	
	-0.5		19	8.37	121.43	53.52	0.44	1.88	-1.37			0.94	-0.97			0.07	0.26	3674	61.34	23481	153.24	0.156	0.003	1.06	1.03	
	-0.7		5.5	7.05	48.36	62.03	1.28	0.19	0.43			0.1	-0.31			0.56	-0.75	2715	52.61	23873	154.51	0.114	0.002	7.25	2.69	
							0.47	6.42	-1.81	0.47	0.11	3	-2.24	0.53	0.15	3.8	-0.57							13.33	5.79	0.1
2.15-2.35	0.7		20	7.68	349.8	134.75	0.39	0.89	-0.94			0.27	-0.52			0.16	0.4	1218	35.33	21303	145.96	0.057	0.002	0.01	0.09	
	0.5		1	8.37	8.43	70.57	8.37	1.43	1.2			6.5	2.55			2.09	1.44	2498	50.58	21069	145.15	0.119	0.003	1.57	-1.25	
	0.3		15.5	9.15	102.54	60.57	0.59	0.24	-0.49			0.03	0.18			0.48	0.69	3185.5	57.12	21074	145.17	0.151	0.003	0.28	0.53	
	0.1		15	8.03	83.78	44.88	0.54	0.47	0.69			0.19	-0.44			1.18	-1.09	3787	62.19	21152	145.44	0.179	0.003	1.42	1.19	
	-0.1		32	8.94	167.37	46.87	0.28	1.57	-1.25			0.16	-0.4			0.71	0.84	4085.5	64.57	21368	146.18	0.191	0.003	0.15	0.39	
	-0.3		8.5	7.47	43.76	38.45	0.88	0.58	0.76			0.19	-0.44			1.44	-1.2	4081	64.64	21011	144.95	0.194	0.003	2.71	1.65	
	-0.5		2.5	5.63	15.17	34.19	2.25	0	-0.06			0.4	0.63			0.46	0.68	3458	59.46	20984	144.86	0.165	0.003	0.12	0.35	
	-0.7		5.5	7.05	43.76	56.13	1.28	0.19	0.43			0.61	-0.78			2.07	-1.44	2715	52.61	21601	146.97	0.126	0.003	7.27	2.7	
							0.53	5.38	0.33	0.53	0.02	8.35	0.78	0.5	0.05	8.61	0.33							13.52	4.44	0.08
																0	0									

Bibliography

[1] J. Ashman *et al.* (EMC Collaboration), Phys. Lett. **B206,** (1988);

M. Arneodo *et al.*, (EMC Collaboration), Z. Phys. **C36,** (1987).

[2] D. Silverman, Phys. Rev. **D54**, 5563 (1996).

[3] B. Bovh, K. Rith, C. Scholz and F. Zetsche, Particles and Nuclei: An Introduction to the Physical Concepts, 1995, 3rd edition, Springer.

[4] Particle Data Group, Phys. Rev. **D54,** (1996).

[5] R.A. Adelseck and B. Saghai, Phys. Rev. **C42,** 108 (1990).

[6] R.A. Williams, C. Ji and S. Cotanch, Phys. Rev. **C46,** 1617 (1992).

[7] T. Mart and C. Bennhold, Phys. Rev. **C61**, 012201(R) (1999).

[8] C. Bennhold, Phys. Rev. **C39,** 1944 (1989).

[9] T. Mart and C. Bennhold, Phys. Rev. **C61**, 012201 (2000).

[10] KAON-MAID interactive code:

www.kph.uni-mainz.de/MAID/kaon/kaonmaid.html.

[11] Photoproduction of Elementary Particles, Vol. 8 of *Landolt-Boernstein Numerical Data and Functional Relationships in Science and Technology*, edited by H. Genzel, P. Joos, and W. Pfeil (Springer, New York, 1973), p. 295-298, 336;

P. Brauel *et al.*, Z. Phys. **C3,** 101 (1979) and references therein.

[12] G. Penner and U. Mosel, Phys. Rev. **C66,** 055212 (2002).

[13] B. Friman and M. Soyeur, Nucl. Phys. **A600,** 477 (1996).

[14] Y. Oh *et al.*, Phys. Rev. **C63,** 025201 (2001).

[15] H. Babacan *et al.*, Eur. Phys. J. **A12,** 355 (2002).

[16] R. Erbe *et al.* (ABBHHM Collaboration), Phys. Rev. **188,** 2060 (1969)

[17] S. Goers *et al.* (SAPHIR collaboration), Phys. Lett. **B464**, 331 (1999).

[18] M.Q. Tran *et al.* (SAPHIR Collaboration), Phys. Lett. **B445**, 20 (1998).

[19] B.D. McDaniel, A. Silverman, R.R. Wilson, and G. Cortellessa, Phys. Rev. **115**, 1039 (1959); H.M. Brody, A.M. Wetherell, and R.L. Walker, Phys. Rev. **119**, 1710 (1960); R.L. Anderson, F. Turkot, and W.M. Woodward, Phys. Rev. **123**, 1003 (1961); R.L. Anderson, *et al.*, Phys. Rev. Lett. **9**, 131 (1962); T. Fujii *et al.*, Phys.Rev. **D2**, 439 (1970); H. Goeing, W. Schorsch, J. Tietge, and W. Weilnboeck, Nucl. Phys. **B26**, 121 (1971); P. Feller, D. Menze, U. Opara, W. Schulz, and W.J. Schwille, Nucl. Phys. **B39**, 413 (1972).

[20] T. Feuster and U. Mosel, Phys. Rev. **C58**, 457 (1998).

[21] T. Feuster and U. Mosel, Phys. Rev. **C59**, 460 (1999).

[22] S. Janssen, J. Ryckebusch, D. Debruyne and T. Van Cauteren, Phys. Rev. **C65,** (2002) 015201.

[23] B. Mecking *et al.*, The CEBAF Large Acceptance Spectrometer, Nucl. Instr. Meth. **A503/3,** 513 (2003).

[24] M. D. Mestayer *et al.*, The CLAS Drift Chamber System, Nucl. Instr. Meth. **A449,** 81 (2000).

[25] M. Amarian *et al.*, The CLAS Forward Electromagnetic Calorimeter, Nucl. Instr. Meth. **A460,** 239 (2001).

[26] E.S. Smith *et al.*, The time-of-flight system for CLAS, Nucl. Instr. Meth. **A432,** 265 (1999).

[27] S. Taylor *et al.*, The CLAS Start Counter, Nucl. Instr. Meth. **A462,** 484 (2001).

[28] R. Bradford and R.A. Schumacher. Liquid H_2 Density in the G1C CLAS Cryotarget. CLAS-NOTE 2002-003, Jefferson Lab, Newport News, VA 23606 (2002).

[29] D.I. Sober *et al.*, The bremsstrahlung tagged photon beam in Hall B at JLab, Nucl. Instr. Meth. **A440,** 263 (2000).

[30] S.K. Matthews *et al.*, Composite thin vacuum window for the CLAS photon tagger at Jefferson Lab, Nucl. Instr. Meth. **A421,** 23 (1999).

[31] V. Blobel, The BOS System: Dynamic Memory Management, DESY, internal report (1994).

[32] L. Todor, G1C Data Calibration and Cooking - Procedures, Characteristics, Information, CLAS analysis note 02-017, Jefferson Lab, Newport News, VA 23606 (2002).

[33] R.A. Schumacher. Photon Attenuation in the CLAS Beam Line. CLAS-NOTE 2001-010, Jefferson Lab, Newport News, VA 23606 (2001).

[34] GEANT - Detector Description and Simulation Tool, CERN program library (1995).

[35] J.W.C. McNabb. Photoproduction of Λ and Σ^0 Hyperons off Protons in the Nucleon Resonance Region using CLAS at Jefferson Lab., Ph.D thesis, Carnegie Mellon University (2002).